EFFECTIVE BROADBAND MEASUREMENTS OF THE PERMITTIVITY OF GEOLOGICAL MATERIALS

SHAHROUKH SOTODEH

A Thesis submitted to the Faculty of Graduate Studies in Partial Fulfillment of the Requirements for the Degree of

MASTER OF SCIENCE

Graduate Program in Earth and Space Science
York University
Toronto, Ontario

April 2014

ABSTRACT

It is a commonly held belief that broadband permittivity measurement techniques have great uncertainties in dielectric loss for low-loss materials, which is unfavorable for applications in planetary and asteroid radar mapping. While true, much of the literature has neglected to address in detail how accurate and effective broadband permittivity measurements truly are. The optimal accuracy is often cited as ± 5% for low to medium loss materials [1]. This thesis reports on the development of a procedure to perform the most accurate and repeatable measurements of the permittivity of granular materials using a coaxial airline. A detailed uncertainty analysis comprising all sources of uncertainty is presented. Measurements of materials with well-known dielectric properties are performed in order to validate the reliability of the laboratory setup, refined sample handling, and measurement procedure. Although the results suggest this as a reliable technique for dielectric constant measurements, they reaffirm the conclusion of poor accuracy in dielectric loss measurements.

DEDICATION

This thesis is dedicated to my parents, Davood and Farahnaz Sotodeh, for their endless love and support throughout my life. Their words of encouragement and unyielding push for me to succeed have undoubtedly helped shape the man I am today. Thank you for keeping me grounded by reminding me of how fortunate I am to have the opportunities you never had back home. For this I am forever grateful. My sisters Jinoos and Pegah, as well as my puppy Cooper, also hold a special place in my heart.

I also dedicate this thesis to my many friends and colleagues who have supported me throughout the process. You know who you are. Thank you for standing by my side through all the good times and bad, and for patiently waiting to celebrate with me once I crossed the finish line.

ACKNOWLEDGMENTS

It is with immense gratitude that I acknowledge the help of my supervisors Professor Michael Daly, Associate Professor in the Department of Earth & Space Science & Engineering at the Lassonde School of Engineering, and Professor Rebecca Ghent, Associate Professor in the Department of Earth Sciences at University of Toronto, as well as their steadfast support over the course of the project. I also wish to thank Jeffrey J. Gillis-Davis, researcher from the University of Hawai`i at Manoa, for providing the space-weathered olivine samples studied in this paper.

I am equally indebted to York University's Machine Shop staff Frank Canzona, Jeff Laurence, Paul Woitalla, and Wilfred Stein for their endless patience while sorting every nook and cranny of the experimental setup used in this thesis.

TABLE OF CONTENTS

LIST OF TABLES

LIST OF FIGURES

CHAPTER 1 Introduction

1.1 Historical Summary

When performing radar mapping of planetary surfaces, plane waves are attenuated once they meet the regolith. In general, electromagnetic waves entering a medium travel slower than in free space. Once a wave meets a medium after travelling through free space it will do a number of things, the extent of which depends on the inherent properties of the material. There is the incident wave, which is directed towards the material, but there will also be reflected and transmitted waves, which may differ in amplitude and phase depending on properties of the sample. This is related to the underlying principle that a wave propagating into a lossy medium experiences field intensity decay. This decay is exponentially related to the direction of propagation of the wave, as well as the propagation constant of the medium. The propagation constant of the material depends primarily on its complex permittivity [2]. Permittivity is an inherent property of an insulating, or dielectric, material; it is a property of matter. This suggests that the type of material can be determined simply by measuring its permittivity, as a specific pairing of real and imaginary values is unique. This has serious implications, as one of the main objectives of most orbital and lander-based missions to other bodies in our solar system is to characterize the composition of both the surface and subsurface [3].

High-resolution subsurface mapping has a number of important applications. These include, but are not limited to, archaeological site investigations, mine development, mapping bedrock depth, changes of rock type, and mineral and groundwater exploration. Most significant for space exploration is the success radar techniques have had in mapping ice thickness, water depth in lakes, soil stratigraphy (study of rock layering), and water table depth [4].

Campbell and Ulrichs (1969) surveyed the electric properties of materials for the purpose of lunar radar investigations. Both the dielectric constant and loss tangent for various rocks and powders were determined. This was done with the intent to determine the relationship between a finely ground powder and the corresponding rock from which it originated. Of particular interest were andesite, basalt, granite, peridotite, pumice, tuff, and volcanic ash. All of the samples are from Earth and are believed to encompass the main constituents of the lunar surface and subsurface [5].

The permittivity of the rocks and powders were measured at two frequencies: 450 MHz and 35 GHz. This was accomplished using the resonant cavity and rectangular waveguide techniques respectively. For the resonant cavity, the samples were placed in a region of high electric field within the cavity. The waveguide technique was able to measure the magnitude and phase of the reflected high frequency signal. All materials under test (MUT) were baked in a high temperature oven at 200 degrees Celsius for 2 days to ensure that most of the contained water had been evaporated. The bulk density of each MUT was found by manually measuring the mass of the sample as well as the volume of the sample holder it filled. This doesn't take air-gaps from pores within the rocks into consideration, causing an estimated error of ± 1% [5]. Furthermore, difficulty in cutting the samples with close tolerances necessary to satisfy tightly fitting the holder cross-section was an issue.

The moon's uppermost layer is composed of fragmented and finely ground rock. This is a trend seen on most planetary surfaces within our solar system. The electrical properties of rocks and powders are dependent on their density, given that they have been dried and are free of water vapour. Based on this property, Campbell and Ulrichs (1969) deduced that this is applicable to radar studies and that radar and radiothermal data can provide accurate information about the regolith density and density gradient of the moon or any other planetary body as long as we have a rough idea of its

composition. Regolith density and density gradient estimate errors don't increase greatly if there are small gaps in knowledge of the regolith composition [5].

By combining their permittivity and density profile results with existing radar reflectivity data from Surveyor, they were able estimate the surface density of the lunar regolith and were able to make some reasonable assumptions regarding the subsurface based on these results. The density of the thin surface layer was found to be $0.6 \pm 0.2\ g/cm^3$ and increased to $1.0\ g/cm^3$ within a few centimetres based on radar investigation. The radar data suggested higher densities down to a few metres below the surface. They believe that radar mounted on a surface probe can be used to obtain a distribution profile of rock lumps within the regolith and detect permafrost layers [5].

A series of assumptions were made for the lunar analogue materials. Firstly, the frequencies at which measurements were done are at two extremes: 450 MHz and 35 GHz. This was done as the authors believed that the intermediate frequency-dependent permittivity values can be determined by extrapolating the two extremes. In addition, it was assumed that all materials measured were non-magnetic (relative permeability $\mu_r' = 1$). This is a problem for rocky and powdered samples possessing magnetite content over 5%. This caused a great deal of overestimation for absorption lengths of the powders. The measurements had an accuracy of ± 3% in real part of the relative permittivity ϵ_r', and ± 10% in loss tangent $\tan\delta$, disregarding the uncertainty caused by the assumptions [5]. Campbell and Ulrichs (1969) believe that their estimates regarding subsurface composition and density distribution from radar observations could have been greatly improved had these assumptions not been made.

Heggy et al. (2001) also saw that the mineralogical composition of planetary surfaces is related to their observed electrical properties. The electric properties of Martian analogues were investigated in order to determine the layer boundaries within Mars. The subsurface was divided into the near and deep subsurface, ranging from 0-400

meters and 400-2500 meters respectively. The near subsurface is mainly volcanic materials with the topmost layer (~10 meters) being of Martian dust. In contrast, the deep subsurface comprises porous volcanic rock, permafrost, ice, and liquid water. The presence of subsurface water is assumed based on high-resolution images from the Mars Orbital Camera (MOC) indicating the presence of gullies. Additionally, the surface morphology of crater ejecta is smoothed, providing evidence of subsurface ground ice [6]. Both subsurface sections comprise a few distinct layers.

The hypothesized Martian subsurface, as determined by Clifford (1993), is, in ascending order of depth, composed of dust, basalt altered rock, lava, sedimentary deposits, basaltic regolith with ice, and basaltic regolith with water. Samples were made in powder and pellet form with compositions similar to these geological layers. Djiboutian basalt proved to be an excellent near subsurface chemical analogue based on results from Viking and Pathfinder chemical analysis [6].

The penetration depth of radar signals for Martian analogue materials was studied and seen to be inversely proportional to frequency; the relationship being linear between 1-6 MHz. For this reason the permittivity of the analogue materials was measured between 1-500 MHz. The parallel-plate capacitance method was used for permittivity measurements as well as a magnetic cell for permeability in the case of iron-rich powders. All rock samples were washed with pure water to avoid any dust contamination. Samples were baked in a high-temperature oven at 350 degrees Kelvin for 2 days to remove moisture. X-ray analysis was done to guarantee a match between Djiboutian and other Martian analogues to Viking, Pathfinder, and Clifford's (1993) results. Rocks were ground in a controlled environment to achieve 50 μm granulation. The pellets were also pressed in a controlled manner to achieve various degrees of porosity to simulate the Martian porosity profile within the subsurface [6].

The permittivity measurements disagreed with the previously used values obtained by Ori and Ogliani (1996) and Picardi et al. (1999). The values that were obtained in the past for the dust, basalt, and lava + regolith layers between 0-200 meters of depth differed in both dielectric constant and loss tangent. The new measurements from Heggy et al. (2001) are considered to be more accurate as compaction and porosity were taken into consideration [6]. Increased loss tangents from the new results suggest higher attenuation factors, thus affecting the effective penetration depth of radar sounding. From this drastic change in loss we can conclude that measurement uncertainties have a big impact on the ability to accurately model the regolith layers.

It was shown that the radar penetration depth increases in an almost linear fashion with increasing porosity, ranging from 400 – 1000 meters for 25 – 55% porosity respectively in the case of Djiboutian basalt measured at 2 MHz. This is crucial as it demonstrates the electrical effects ignored by Ori and Ogliani (1996) and Picardi et al. (1999) in analyzing previous measurements. Conversely, for a realistic scenario with layers of volcanic rock, it would be difficult to achieve a penetration depth of even 1 km [6], as the first few layers within the near subsurface are iron-rich, and consequently conductive, they are lossy and as a result affect penetration depth.

For water to be detected in the subsurface of Mars, or any planetary body for that matter, there needs to be a distinct boundary between the rock/regolith and water layer. In other words, a sharp transition in dielectric constant is needed to distinguish between the frozen soil and wet regions for radar investigations to be successful. Heggy et al. (2001) see this as being unlikely in a real situation as porous rocks and frozen soils (ground-ice) may contain trace amounts of unfrozen water at very low temperatures. This presence of water in the ground-ice will cause a moisture gradient throughout the layers leading up to the water. In essence, a smooth increase in real and imaginary permittivity will be present and will prevent the water layer from being discovered with

ease due to the lack of a sharp transition point. This is a challenge and illustrates the need to study the electric properties of complex soil scenarios [6].

Another challenge presented for the detection of water is the geological context of the upper layers. This is true even in the case of possible reservoirs at shallow depths. If the covering layer of material is comprised of carbonates, which are weakly absorbent, then deep subsurface water can be discovered. However, highly absorbent covering layers with high losses will inhibit the propagation of radar waves. As was seen by Heggy et al. (2001), water cannot be easily detected based on the model of the Martian layers assumed using a 2 MHz radar signal. It is suggested that select sites with sharp soil/ice transitional boundaries be chosen for radar sounding to achieve satisfactory penetration depth and thus potentially detect any evidence of water [6]. The importance of broad frequency, temperature, porosity, and compositional investigations are emphasized for in depth permittivity studies. In addition, accurate results will help determine landing sites for future sounding missions.

1.2 Research Context

Radar is a valuable tool for the investigation of planetary surfaces and asteroids, and allows refinement in orbit calculations and improvements of ephemerides. It also permits constraints on the physical and chemical properties of the regolith. Although variations in radar albedo are a good indicator of changes in near-surface regolith structure, density, and metal content, additional work is required to constrain the radar characteristics of geological materials. To aid in addressing these issues, a measurement and analysis protocol for broadband permittivity measurements for the purpose of accurate planetary and asteroid radar mapping has been developed.

Compositional variations in mineral constituents have effects on the electrical properties of regolith. These variations may likely impact very low loss materials such as lunar anorthosites, as does the presence of adsorbed water. By developing a body of

knowledge about the permittivity of good analogs, we can place regolith samples in the appropriate context and thus broaden our understanding of variations in the radar properties of other objects.

1.3 Research Objectives

The ultimate goal is to develop a procedure to perform the most accurate and repeatable permittivity measurements of semi-solids (powders) that are geological in nature, given the limitations of the technique. Ultimately the coaxial transmission line technique was selected for this research. The method allows the wave to be guided along a finite cross-section from one point to another [7]. In the case of the coaxial airline, it is broadband in nature. This method allows frequency measurements ranging all the way up to the tens of GHz [8] and can measure down to DC (0 Hz), however the practicality of the results depend entirely on the sample length and capabilities of the test equipment [9] [10].

One of the main problems that many authors of broadband permittivity research papers have neglected to address in detail is the assessment of how accurate broadband permittivity measurements truly are. The optimal accuracy is often cited as ± 5% for low to medium loss materials [1]; however there is rarely mention of the specific loss range this applies to. Loss tangent is also said to vary by ± 0.01 [8] in an ideal scenario where the common sources of error are accounted for. In spite of this one needs to understand the severity of these sources of uncertainty and how common they are. It is thus imperative to direct our attention to adopting a measurement procedure and error model, as well as to consider measures that can be taken to improve the accuracy of permittivity measurements. This also demands a refined approach for sample handling to be used in the laboratory.

The dielectric response of materials will be determined over a wide range of frequencies spanning 0.1 – 8 GHz. To do so, a 2-port Network Analyzer will be used to sweep through different source frequencies and used to measure the transmitted and reflected

signals of a sample-filled coaxial holder. The travelling incident, reflected, and transmitted waves will thus be used to derive the complex permittivity of a medium in a network using data conversion algorithms. As a precaution, materials with well-known dielectric properties will be measured initially to verify the reliability of the laboratory setup, refined sample handling, and measurement procedure. Once validated, a detailed error analysis comprising all error sources will be investigated to determine how reliable the results are using this particular broadband technique. The end result of this project is an investigation of the permittivity of various geological materials that will help better characterize the accuracy, and thus relieve some ambiguities, for the purpose of future applications in planetary and asteroid radar mapping.

CHAPTER 2 Theoretical Background

2.1 EM Theory

2.1.1 Maxwell's Equations

2.1.1.1 Gauss's Law for Electric Fields

Electric charges produce their own electrostatic fields. The charge distribution is related to the spatial behaviour of the aforementioned field that it produces via Gauss's law for electric fields. This equation is Maxwell's first equation and is as follows [11] [2]:

$$\vec{\nabla} \cdot \vec{\mathrm{E}} = {}^{\rho}/_{\varepsilon_0}$$

where $\vec{\nabla} \cdot$ is the divergence, $\vec{\mathrm{E}}$ is the electric field in Newtons per coulomb, ρ is the charge density in coulombs per cubic metre, and ε_0 is the vacuum or free-space permittivity (8.854 187 817 × 10^{-12} farads per metre).

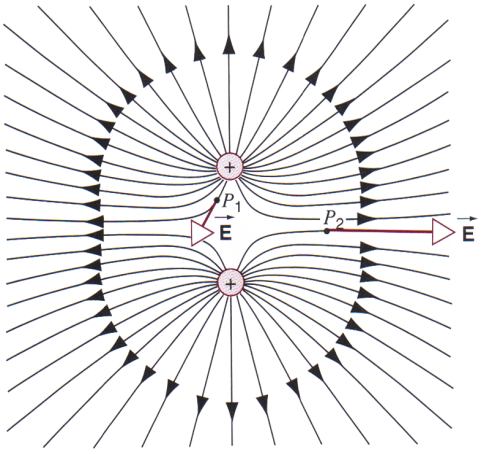

Figure 1 - Two equally positive charges repelled by each other. Notice the divergence of the field lines away from the positive charges [12]

The divergence of the field is another way of describing its inclination to flow away from a point source. In other words, Maxwell's first equation tells us that any electric field diverges, or flows away, from a positive charge and converges, or flows towards, a negative charge. This means that the divergence is zero only at the individual points in space at which there are no charges present [11]. A positive electric field divergence is attributed to a positive charge and a negative divergence to a negative charge.

2.1.1.2 Gauss's Law for Magnetic Fields

Both of Gauss's laws are similar in that they describe the divergence of a field, electric and magnetic respectively, at a point. Gauss's law of magnetic fields is different from the previous law because, unlike electric charges that can be isolated in positive and negative charges, magnetic poles exist solely in pairs. Magnetic north and south monopoles have not been documented in nature and are believed to not exist, thus impacting the spatial behaviour of the magnetic field. This leads to Maxwell's second equation [11] [2] [7]

$$\vec{\nabla} \cdot \vec{B} = 0$$

where $\vec{B}$ is the magnetic field in teslas.

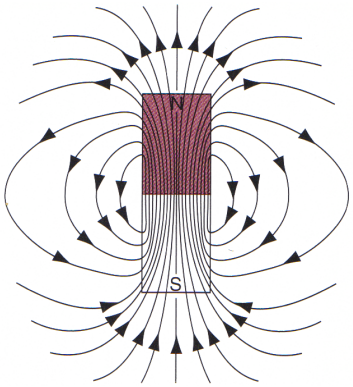

Figure 2 - A bar magnet possesses field lines travelling from north to south. These are closed loops [12]

The divergence of the magnetic field is another way of describing its inclination to flow with greater strength away from a point and with weaker strength toward it. As mentioned earlier, magnetic monopoles do not exist; you cannot have a north pole without a south pole. This means that the magnetic equivalent of the electric charge density ρ must be zero everywhere [11]. In other words, Maxwell's second equation tells us that the divergence of a magnetic field is zero at any point.

2.1.1.3 Faraday's Law

Maxwell's first equation deals with electrostatic fields produced by electric charges, whereas Faraday's law, leading to Maxwell's third equation, deals with induced electric fields produced by a changing magnetic field. Maxwell's third equation is [11] [2] [7]

$$\vec{\nabla} \times \vec{\mathrm{E}} = -\frac{\partial \vec{\mathrm{B}}}{\partial t}$$

where $\vec{\nabla} \times$ is the curl and $\frac{\partial \vec{\mathrm{B}}}{\partial t}$ is the time dependent rate of change of the magnetic field. The curl of the electric field describes the circulatory motion of its field lines around a point. We know from Maxwell's first equation that electrostatic fields have termination points; the flow of the field is from a positive to negative charge, thus no circulatory motion and therefore no curl.

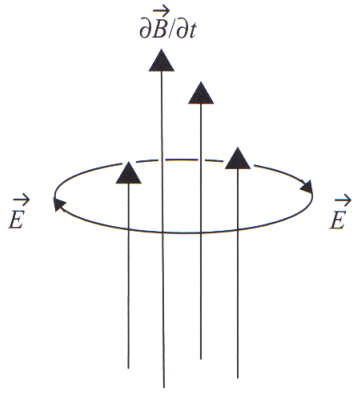

Figure 3 - An electric field generated by a changing magnetic field. Note that the field lines curve back on themselves due to the magnetic field [11]

Induced electric fields are different such that the presence of a changing magnetic field allows the field lines to circulate back on themselves and act as continuous (circulating). This means that they have curl. Maxwell's third equation implies that a faster change in magnetic field produces an induced electric field curl with greater magnitude [11].

2.1.1.4 Ampere-Maxwell Law

The Ampere-Maxwell law is perhaps the most important of the four Maxwell equations. Originally, Ampere discovered that a magnetic field can be generated by an electrical current. This was known as Ampere's law. Maxwell noticed that this law only applied to static situations. He then added a correction to Ampere's law which stated that magnetic fields can be generated by a second method using changing electric fields. The fourth and last Maxwell equation is as follows [11] [2]:

$$\vec{\nabla} \times \vec{\mathrm{B}} = \mu_0 \left(\vec{\mathrm{J}} + \varepsilon_0 \frac{\partial \vec{\mathrm{E}}}{\partial t} \right)$$

where $\vec{\mathrm{J}}$ is the electrical current density in amperes per square metre, $\frac{\partial \vec{\mathrm{E}}}{\partial t}$ is the time dependent rate of change of the electric field, and μ_0 is the vacuum or free space permeability ($4\pi \times 10^{-7}$ volt-seconds per ampere-metre).

The curl of the magnetic field describes the circulatory motion of its field lines around a point. There exist two locations at which the curl of the magnetic field isn't zero; the exact location of current flow or a changing electric field. Maxwell's fourth equation tells us that a changing electric field induces a magnetic field, and also that a changing magnetic field induces an electric field (as seen in the third equation) [11]. This revelation has serious implications such that it allows self-sustaining electromagnetic waves to travel in a vacuum. This gives way to the wave equation.

2.1.2 Maxwell's Equations in Matter

The Maxwell Equations, presented earlier, apply to fields present both in free space and within matter. However, when dealing with electric and magnetic fields inside matter, we must reconsider our treatment of the charge density ρ and electrical current density, $\vec{\mathrm{J}}$. In matter, ρ encompasses both bound and free charges, while $\vec{\mathrm{J}}$ encompasses bound, polarized, and free current. By remembering these important points, new expressions for Gauss' Law for Electric Fields and the Ampere-Maxwell can be developed since they directly involve electric charge and current in their differential forms [13].

2.1.2.1 Modified Gauss' Law for Electric Fields

When an electric field is applied within a dielectric material, equal positive and negative charges are displaced from each other by a distance, d. A measure of this system's overall polarity is called the electric dipole moment $\vec{\mathrm{p}}$ and is expressed as [11]

$$\vec{\mathrm{p}} = Q\vec{\mathrm{d}}$$

where $\vec{\mathrm{d}}$ is a vector expressing the magnitude and direction of the charge separation and Q is the charge (equal for both positive and negative). It is useful to think of this quantity per unit volume as well, and is referred to as the electric polarization $\vec{\mathrm{P}}$ of the dielectric media. Assuming N molecules in the material per unit volume, $\vec{\mathrm{P}}$ is expressed as [11] [7]

$$\vec{\mathrm{P}} = N\vec{\mathrm{p}}$$

As mentioned earlier, the total charge density is separated into bound and free charges as follows [11]:

$$\rho = \rho_b + \rho_f$$

where ρ_b is the volume density of bound charges displaced by the electric field and ρ_f is the free charge density. If the electric polarization isn't uniform and varies from point to point within the material, there will be accumulations of bound charges. It is treated as a divergence (or flow) of the polarization away from a point using [11]

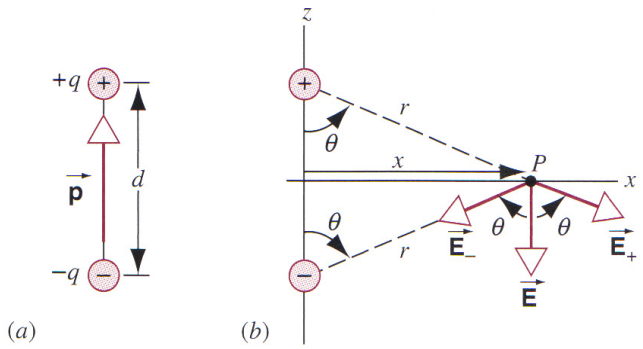

Figure 4 - a) An electric dipole formed by opposite charges that are equal in magnitude. b) The electric field at any point can be found by considering the vector sum of the individual sources [12]

$$\rho_b = -\vec{\nabla} \cdot \vec{\mathrm{P}}$$

where the negative sign arises due to the opposite signs of the charges. If we go back and look at Gauss' law for electric fields and make the appropriate substitutions for total charge density we have [11] [13] [7]

$$\vec{\nabla} \cdot \vec{\mathrm{E}} = {}^{\rho}/_{\varepsilon_0} = {}^{(\rho_b + \rho_f)}/_{\varepsilon_0}$$

$$\vec{\nabla} \cdot \varepsilon_0 \vec{\mathrm{E}} = \rho_b + \rho_f = \left(-\vec{\nabla} \cdot \vec{\mathrm{P}}\right) + \rho_f$$

$$\vec{\nabla} \cdot \varepsilon_0 \vec{\mathrm{E}} + \vec{\nabla} \cdot \vec{\mathrm{P}} = \vec{\nabla} \cdot \left(\varepsilon_0 \vec{\mathrm{E}} + \vec{\mathrm{P}}\right) = \rho_f$$

$$\vec{\nabla} \cdot \vec{\mathrm{D}} = \rho_f$$

where $\vec{D} = \varepsilon_0 \vec{E} + \vec{P}$ and is called the displacement. This is the modified form of Maxwell's first equation for matter.

2.1.2.2 Modified Ampere-Maxwell Law

As with the total charge density in Maxwell's first equation, the total current density is separated into bound, polarized, and free current as follows [11]

$$\vec{J} = \vec{J}_b + \vec{J}_P + \vec{J}_f$$

where $\vec{J}_b$ is the bound current density, $\vec{J}_P$ is the polarization current density, and $\vec{J}_f$ is the free current density. Just as an applied electric field within a dielectric medium produces an electric dipole moment, an applied magnetic field induces a magnetic dipole moment. We saw that the electric dipole moment per unit volume was referred to as the polarization $\vec{P}$. A similar term, magnetization $\vec{M}$, exists since bound currents may also act as additional sources of magnetic fields. Due to its circulatory motion, it is treated as the curl of the magnetization and is [11]

$$\vec{J}_b = \vec{\nabla} \times \vec{M}$$

Any charge movement or displacement is considered electric current. Since polarization within the material may change with time, the polarization current density is defined as its time rate of change with [11]

$$\vec{J}_P = \frac{\partial \vec{P}}{\partial t}$$

If the appropriate substitutions for total current density are made in the Ampere-Maxwell equation, the following results [11] [13] [7]

$$\vec{\nabla} \times \vec{\mathrm{B}} = \mu_0 \left(\vec{\mathrm{J}} + \varepsilon_0 \frac{\partial \vec{\mathrm{E}}}{\partial t} \right) = \mu_0 \left(\vec{\mathrm{J}}_b + \vec{\mathrm{J}}_P + \vec{\mathrm{J}}_f + \varepsilon_0 \frac{\partial \vec{\mathrm{E}}}{\partial t} \right)$$

$$\vec{\nabla} \times \frac{\vec{\mathrm{B}}}{\mu_0} = \vec{\mathrm{J}}_b + \vec{\mathrm{J}}_P + \vec{\mathrm{J}}_f + \varepsilon_0 \frac{\partial \vec{\mathrm{E}}}{\partial t} = \left(\vec{\nabla} \times \vec{\mathrm{M}} \right) + \frac{\partial \vec{\mathrm{P}}}{\partial t} + \vec{\mathrm{J}}_f + \varepsilon_0 \frac{\partial \vec{\mathrm{E}}}{\partial t}$$

$$\vec{\nabla} \times \frac{\vec{\mathrm{B}}}{\mu_0} - \vec{\nabla} \times \vec{\mathrm{M}} = \vec{\nabla} \times \left(\frac{\vec{\mathrm{B}}}{\mu_0} - \vec{\mathrm{M}} \right) = \vec{\mathrm{J}}_f + \frac{\partial \left(\varepsilon_0 \vec{\mathrm{E}} + \vec{\mathrm{P}} \right)}{\partial t}$$

$$\vec{\nabla} \times \vec{\mathrm{H}} = \vec{\mathrm{J}}_f + \frac{\partial \vec{\mathrm{D}}}{\partial t}$$

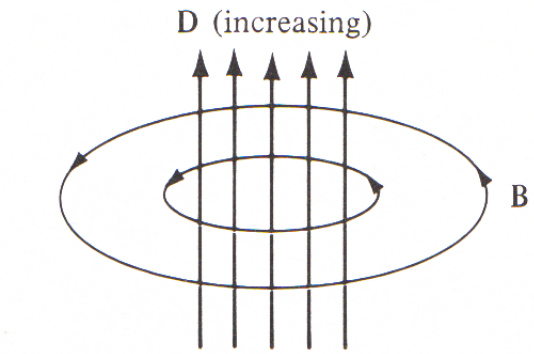

Figure 5 - A curling magnetic field created by a time changing electric flux [13]

where $\vec{\mathrm{H}} = \frac{\vec{\mathrm{B}}}{\mu_0} - \vec{\mathrm{M}}$ and is called the magnetic field strength. Recall that the displacement $\vec{\mathrm{D}} = \varepsilon_0 \vec{\mathrm{E}} + \vec{\mathrm{P}}$ is the same as before. This is the modified form of Maxwell's fourth equation for matter.

2.1.3 The Wave Equation

The grouping of Maxwell's equations from the previous section, leads to a comprehensive theory of electromagnetism as developed by Maxwell himself. Starting with Faraday's law and applying the curl operator to both sides of the equation [11] [13]:

$$\vec{\nabla} \times \left(\vec{\nabla} \times \vec{\mathrm{E}}\right) = \vec{\nabla} \times \left(-\frac{\partial \vec{\mathrm{B}}}{\partial t}\right) = -\frac{\partial\left(\vec{\nabla} \times \vec{\mathrm{B}}\right)}{\partial t}$$

$$\vec{\nabla}\left(\vec{\nabla} \cdot \vec{\mathrm{E}}\right) - \nabla^2 \vec{\mathrm{E}} = -\frac{\partial\left(\vec{\nabla} \times \vec{\mathrm{B}}\right)}{\partial t}$$

Two terms that have been defined earlier can be identified; the divergence of the electric field and the curl of the magnetic field. Substituting these terms from Maxwell's first and fourth equations respectively gives

$$\vec{\nabla}\left({}^{\rho}/_{\varepsilon_0}\right) - \nabla^2 \vec{\mathrm{E}} = -\frac{\partial\left(\mu_0\left(\vec{\mathrm{J}} + \varepsilon_0 \frac{\partial \vec{\mathrm{E}}}{\partial t}\right)\right)}{\partial t} = -\mu_0 \frac{\partial \vec{\mathrm{J}}}{\partial t} - \mu_0 \varepsilon_0 \frac{\partial^2 \vec{\mathrm{E}}}{\partial t^2}$$

$$\nabla^2 \vec{\mathrm{E}} - \mu_0 \varepsilon_0 \frac{\partial^2 \vec{\mathrm{E}}}{\partial t^2} = \mu_0 \frac{\partial \vec{\mathrm{J}}}{\partial t} + \vec{\nabla}\left({}^{\rho}/_{\varepsilon_0}\right)$$

If the wave is propagating in a simple medium, the permittivity and permeability would be $\varepsilon = \varepsilon_0 \varepsilon_r$ and $\mu = \mu_0 \mu_r$ respectively and substituted in the final form of [13]

$$\nabla^2 \vec{\mathrm{E}} - \mu\varepsilon \frac{\partial^2 \vec{\mathrm{E}}}{\partial t^2} = \mu \frac{\partial \vec{\mathrm{J}}}{\partial t} + \vec{\nabla}\left({}^{\rho}/_{\varepsilon}\right)$$

In a region with no charge or current, such as in a vacuum, the equation reduces to [11] [14]

$$\nabla^2 \vec{\mathrm{E}} - \mu_0 \varepsilon_0 \frac{\partial^2 \vec{\mathrm{E}}}{\partial t^2} = 0$$

since both the charge density ρ and electrical current density $\vec{\mathrm{J}}$ are zero. Applying the same set of manipulations to the modified Ampere-Maxwell law, starting with the curl, produces [11] [13]:

$$\vec{\nabla} \times \left(\vec{\nabla} \times \vec{\mathrm{H}}\right) = \vec{\nabla} \times \left(\vec{\mathrm{J}}_f + \frac{\partial \vec{\mathrm{D}}}{\partial t}\right) = \left(\vec{\nabla} \times \vec{\mathrm{J}}\right) + \frac{\partial\left(\vec{\nabla} \times \vec{\mathrm{D}}\right)}{\partial t}$$

$$\vec{\nabla}\left(\vec{\nabla} \cdot \vec{\mathrm{H}}\right) - \nabla^2 \vec{\mathrm{H}} = \left(\vec{\nabla} \times \vec{\mathrm{J}}\right) + \frac{\partial\left(\vec{\nabla} \times \vec{\mathrm{D}}\right)}{\partial t}$$

Note that $D = \varepsilon E$, $B = \mu H$, and $J = \sigma E$ are called constitutive equations and apply to all media [13] [14], where σ is the conductivity in Siemens per metre. By making the appropriate substitutions we can continue [13] [7]:

$$\vec{\nabla}\left(\vec{\nabla} \cdot \left(\frac{\vec{\mathrm{B}}}{\mu}\right)\right) - \nabla^2 \vec{\mathrm{H}} = \left(\vec{\nabla} \times \vec{\mathrm{J}}\right) + \frac{\partial\left(\vec{\nabla} \times \left(\varepsilon \vec{\mathrm{E}}\right)\right)}{\partial t}$$

$$\frac{1}{\mu}\vec{\nabla}(0) - \nabla^2 \vec{\mathrm{H}} = \left(\vec{\nabla} \times \vec{\mathrm{J}}\right) + \varepsilon \frac{\partial\left(-\frac{\partial \vec{\mathrm{B}}}{\partial t}\right)}{\partial t}$$

$$-\nabla^2 \vec{\mathrm{H}} = \left(\vec{\nabla} \times \vec{\mathrm{J}}\right) + \varepsilon \frac{\partial\left(-\frac{\partial\left(\mu \vec{\mathrm{H}}\right)}{\partial t}\right)}{\partial t}$$

$$-\nabla^2 \vec{\mathrm{H}} = \left(\vec{\nabla} \times \vec{\mathrm{J}}\right) - \mu\varepsilon \frac{\partial^2 \vec{\mathrm{H}}}{\partial t^2}$$

$$\nabla^2 \vec{\mathrm{H}} - \mu\varepsilon \frac{\partial^2 \vec{\mathrm{H}}}{\partial t^2} = -\vec{\nabla} \times \vec{\mathrm{J}}$$

again, in a charge- and current-free region, $\vec{\nabla} \times \vec{\mathrm{J}}$ is zero, thus [11] [14]

$$\nabla^2 \vec{\mathrm{H}} - \mu\varepsilon \frac{\partial^2 \vec{\mathrm{H}}}{\partial t^2} = 0$$

Both of these newly derived equations describe a field - electric and magnetic respectively - travelling from one location to the next. In other words, this is a propagating wave. The left side of both the electric and magnetic equations is in the form of what is called the wave equation. The right side describes the sources of the waves [13]. The general form of the wave equation can be expressed as [11] [13]

$$\nabla^2\vec{\mathrm{A}} = \frac{1}{v^2}\frac{\partial^2\vec{\mathrm{A}}}{\partial t^2}$$

where v is the speed at which the wave is travelling and equal to $1/\sqrt{\mu_0\mu_r\varepsilon_0\varepsilon_r}$ in any medium.

2.1.4 The Wave Equation in Simple Media

Waves that propagate in a vacuum are expected to continue travelling at the same intensity given that they do not meet any obstacles. However, waves that propagate in other media which may be lossy are bound to experience absorption resulting in a decay in intensity and amplitude. Media that conduct electricity, such as salt water or metal, can have very high losses. We can account for the effects of these losses by substituting the constitutive relation for the conduction current density ($J = \sigma E$, which is Ohm's law in vector form) and magnetic flux density ($B = \mu H$) into the wave equations, and assuming $\rho = 0$ [13]:

$$\nabla^2\vec{\mathrm{E}} - \mu\varepsilon\frac{\partial^2\vec{\mathrm{E}}}{\partial t^2} = \mu\frac{\partial\vec{\mathrm{J}}}{\partial t} + \vec{\nabla}\left(\rho/\varepsilon\right)$$

$$\nabla^2\vec{\mathrm{E}} - \mu\varepsilon\frac{\partial^2\vec{\mathrm{E}}}{\partial t^2} = \mu\frac{\partial(\sigma\vec{\mathrm{E}})}{\partial t} + 0$$

$$\nabla^2\vec{\mathrm{E}} - \mu\varepsilon\frac{\partial^2\vec{\mathrm{E}}}{\partial t^2} - \sigma\mu\frac{\partial\vec{\mathrm{E}}}{\partial t} = 0$$

and

$$\nabla^2\vec{\mathrm{H}} - \mu\varepsilon\frac{\partial^2\vec{\mathrm{H}}}{\partial t^2} = -\vec{\nabla}\times\vec{\mathrm{J}}$$

$$\nabla^2\vec{\mathrm{H}} - \mu\varepsilon\frac{\partial^2\vec{\mathrm{H}}}{\partial t^2} = -\vec{\nabla}\times\left(\sigma\vec{\mathrm{E}}\right) = -\sigma\left(\vec{\nabla}\times\vec{\mathrm{E}}\right) = -\sigma\left(-\frac{\partial\vec{\mathrm{B}}}{\partial t}\right)$$

$$\nabla^2\vec{\mathrm{H}} - \mu\varepsilon\frac{\partial^2\vec{\mathrm{H}}}{\partial t^2} = \sigma\frac{\partial(\mu\vec{\mathrm{H}})}{\partial t} = \sigma\mu\frac{\partial\vec{\mathrm{H}}}{\partial t}$$

$$\nabla^2\vec{\mathrm{H}} - \mu\varepsilon\frac{\partial^2\vec{\mathrm{H}}}{\partial t^2} - \sigma\mu\frac{\partial\vec{\mathrm{H}}}{\partial t} = 0$$

The last two differential terms for both the electric and magnetic field equations are very important. The first in the general form of $\mu\varepsilon\frac{\partial^2\vec{\mathrm{A}}}{\partial t^2}$ will dominate in an insulating (or lossless medium) and $\sigma = 0$, leaving us with the free-space (vacuum) form of the wave equation. In a conducting medium such as a metallic box or salt water, the second differential in the general form of $\sigma\mu\frac{\partial\vec{\mathrm{A}}}{\partial t}$ will dominate, and $\mu\varepsilon\frac{\partial^2\vec{\mathrm{A}}}{\partial t^2}$ is negligible and can be eliminated. The latter situation will give us the equation for diffusion [13].

2.1.5 Complex Permittivity

Permittivity is an electromagnetic phenomenon, the discovery of which is attributed to Faraday when he was experimenting with capacitors. It is a well-known fact that conductors allow charges to move freely once an external electric field is applied. Conversely, insulators do not allow charges to move freely even in the presence of such

a field [2]. However, it was observed that once an insulator was fit to fill the gap between two parallel-plate conductors, there was an increase in the capacitance. The free-space capacitance of a parallel plate capacitor is defined as [2] [13] [7]:

$$C_0 = {}^{\epsilon_0 A}/_{d}$$

where d is the distance between the plates and A is the area of each plate (it is expected that both have the same dimensions). As the area and distance between the plates remain constant, it is evident that an increase in capacitance is due to the proportional increase in the absolute permittivity. This increase factor is then an inherent property of the insulating, or dielectric, material; it is a property of matter [2].

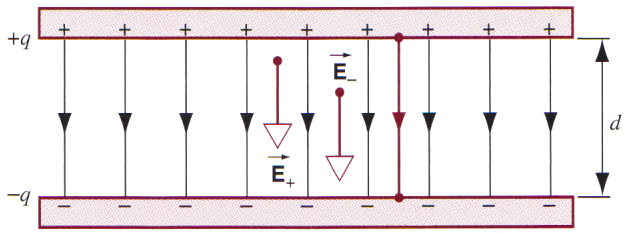

Figure 6 - A parallel plate capacitor. The electric field lines pass from the positive to the negative charges [12]

When dealing with the permittivity of a given material, it is common practice to express it in terms of the free-space permittivity; in other words, the ratio of the amount of energy stored in a given material in relation to that stored in a vacuum due to an applied voltage. This ratio, or factor increase, first observed by Faraday in capacitive materials is called the relative permittivity and is denoted as [2] [13]:

$$\epsilon_r = {}^{\epsilon}/_{\epsilon_0}$$

where ε is the absolute permittivity of the material in Farads per metre. Relative permittivity is often regarded as a complex expression and has two components; one

real and one imaginary [9]. The real part of the permittivity, ε_r', is referred to as the dielectric constant, which is defined as the stored electrical energy within a given medium. The imaginary part, ϵ_r'', is known as the loss factor and, as its name states, is defined as the loss or dissipation of electrical energy within the medium. This relationship is represented in the following complex form [8] [13]:

$$\epsilon_r = \epsilon_r' - j\epsilon_r'' = \epsilon_r' - j\frac{\sigma}{\omega} = \epsilon_r'\left(1 - j\frac{\sigma}{\omega\epsilon_r'}\right)$$

where ω is the angular frequency equal to $2\pi f$, σ is the conductivity in Siemens per metre, and j is $\sqrt{-1}$. The dissipation of electrical energy is often expressed as the loss tangent; the ratio of electrical energy lost in a medium to the energy stored. Its expression takes on the form [15]:

$$\tan\delta = {\epsilon_r''}\Big/{\epsilon_r'}$$

It should be noted that the permittivity response of a given medium or material can change depending on the frequency of the applied field, surrounding temperature, and humidity [8]. The extent to which these factors affect the permittivity depends entirely on the material's inherent properties and is not easily characterized in a general form; their influence is verified under laboratory conditions. Also, all naturally occurring materials such as soil, vegetation, rocks etc. are in fact porous and considered mixtures [16] [17]. The three main constituents of these mixtures are the bulk (or host) material, air, and water usually in the form of moisture.

2.1.6 Wave Propagation

Now that a more matter-friendly expression for two of Maxwell's equations has been devised they can be used along with the two other remaining unmodified equations to

derive the wave equation in a simple lossy material. An expression can be developed to show how the wave propagates in space. Re-examining the wave equation in simple media:

$$\nabla^2\vec{\mathrm{E}} - \mu\varepsilon\frac{\partial^2\vec{\mathrm{E}}}{\partial t^2} - \sigma\mu\frac{\partial\vec{\mathrm{E}}}{\partial t} = 0$$

Waves travelling through a guided line operate in the TEM mode, which means they possess transverse electric and magnetic fields that are orthogonal to the direction of travel. The wave equation above is in its general form. Assuming the wave is travelling in the z-direction with one component of electric field $E = \hat{x}E_x$, the relationship becomes [13]

$$\vec{\mathrm{E}}(z,t) = E_x(z,t) = E_x(z)e^{j\omega t}\hat{x}$$

By substituting this term, the wave equation can be simplified to [13]

$$\frac{\partial^2 E_x(z)}{\partial z^2} + \omega^2\mu\varepsilon\left(1 - j\frac{\sigma}{\omega\varepsilon}\right)E_x(z) = 0$$

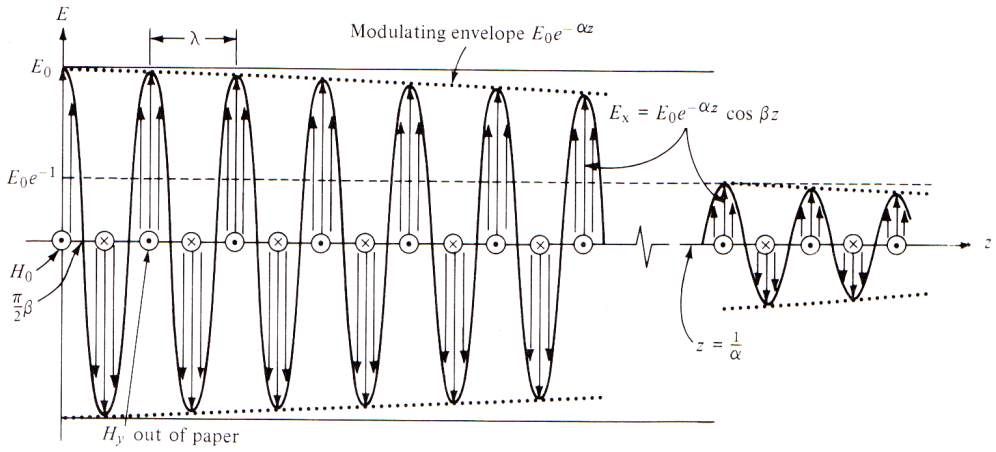

Figure 7 - A wave travelling through a low-loss material with some absorption. Notice the exponential decay in intensity due to the absorbing media [13]

Please note the term $e^{j\omega t}\hat{x}$ was common and eliminated since the right side of the equation is zero. Also, the middle term has the factor $\varepsilon\left(1 - j\frac{\sigma}{\omega\varepsilon}\right)$, which is in the form of the complex permittivity presented in the previous section. In order to show the complex nature of a value, * will be used for notation. Substituting this term results in [13]

$$\frac{\partial^2 E_x(z)}{\partial z^2} + \omega^2\mu\varepsilon^* E_x(z) = 0$$

This equation is that of simple harmonic motion, the solution of which is sinusoidal. The term $\omega^2\mu\varepsilon^*$ is known as the complex phase-propagation constant, represented by β^* where in complex form it is defined as [13]

$$\beta^* = \beta - j\alpha$$

where α is the attenuation constant and β is the phase constant. The solution to the simple harmonic motion equation in the case of plane waves then becomes [13]

$$E_x(z) = E_0^i e^{-j\beta^* z} + E_0^r e^{j\beta^* z}$$

where E_0^i and E_0^r are the amplitudes of the incident and reflected waves respectively. Assuming no reflections and re-substituting the time dependence term $e^{j\omega t}$ removed earlier, we have [13]

$$E_x(z,t) = E_0(e^{j\omega t})e^{-j\beta^* z} = E_0 e^{j(\omega t - \beta^* z)} = E_0 e^{-\alpha z} e^{j(\omega t - \beta z)}$$

This is the final form of the single-frequency solution to the wave equation. Fortunately, this solution allows us to determine the correct behaviour of a wave travelling through a

purely insulating (dielectric) or conducting material simply by setting ε^* equal to ε or $-j\frac{\sigma}{\omega}$ respectively.

2.2 Scattering Parameters

Electromagnetic waves will undergo a certain amount of transmission and reflection when entering media that possess a different impedance from that of the wave's incident medium. Microwave devices, such as Vector Network Analyzers, are defined by these incident electric field discontinuities during wave propagation [18]. Scattering (S) parameters describe the relationship between the initial, transmitted, and reflected wave and can be measured by microwave devices. In an *N*-port microwave network, S parameters represent these relationships using root power waves [19].

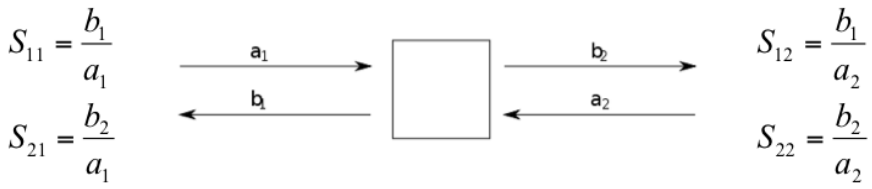

Figure 8 - Two-port network S Parameters [20]

Root power waves are used to describe forward and backward travelling voltage (V_n^+ and V_n^-) and current waves (I_n^+ and I_n^-) at port n of the network. The nth port of the microwave network will have a transmission line with a characteristic impedance of Z_{0n} [19]. Assuming a standard *N x N* matrix as an example, the voltage is obtained through a simple matrix multiplication of the impedance (Z) parameters and the current, and is as follows:

$$\begin{bmatrix} V_1 \\ \vdots \\ V_N \end{bmatrix} = \begin{bmatrix} Z_{11} & \cdots & Z_{1N} \\ \vdots & \ddots & \vdots \\ Z_{N1} & \cdots & Z_{NN} \end{bmatrix} \begin{bmatrix} I_1 \\ \vdots \\ I_N \end{bmatrix}$$

The diagonal portion of the Z parameter matrix is used as the diagonal component of the reference characteristic impedance matrix Z_0, thus representing the characteristic impedance at each individual port. All other elements in the matrix are set to zero. Using this new matrix, an expression for the root power wave (forward and backward respectively) at the *n*th port [19] can be developed:

$$a_n = V_n^+ / \sqrt{Z_{0n}} \text{ and } b_n = V_n^- / \sqrt{Z_{0n}}$$

Knowing that admittance (Y) is the reciprocal of impedance when all reference lines have the same characteristic impedance, in a 2-port network these relationships reduce to:

$$\begin{bmatrix} a_1 \\ a_2 \end{bmatrix} = \begin{bmatrix} \sqrt{Z_{01}} & 0 \\ 0 & \sqrt{Z_{02}} \end{bmatrix}^{-1} \begin{bmatrix} V_1^+ \\ V_2^+ \end{bmatrix} = \begin{bmatrix} \sqrt{Y_{01}} & 0 \\ 0 & \sqrt{Y_{02}} \end{bmatrix} \begin{bmatrix} V_1^+ \\ V_2^+ \end{bmatrix}$$

$$\begin{bmatrix} b_1 \\ b_2 \end{bmatrix} = \begin{bmatrix} \sqrt{Z_{01}} & 0 \\ 0 & \sqrt{Z_{02}} \end{bmatrix}^{-1} \begin{bmatrix} V_1^- \\ V_2^- \end{bmatrix} = \begin{bmatrix} \sqrt{Y_{01}} & 0 \\ 0 & \sqrt{Y_{02}} \end{bmatrix} \begin{bmatrix} V_1^- \\ V_2^- \end{bmatrix}$$

The formal definition for S parameters then becomes [18] [19]

$$S = [b][a]^{-1}$$

2.3 Transmission-Reflection Line Theory

Using the transmission-reflection method, a sample's permittivity and permeability can easily be measured by placing it inside a transmission line. In a typical *N*-port network configuration, all ports have the same characteristic impedance. A reference transmission line with the same characteristic impedance as the ports is placed between two ports, with the sample inserted in this line. Unless the transmission line is empty,

the sample, or material under test (MUT), will undoubtedly have an impedance that differs from that of the reference line. This change in impedance, caused by a change in the wave's propagation environment, will alter the electric field of the normalized incident wave. By investigating the scattering equations at the sample interfaces that relate the S parameters of the sample section to its permittivity and permeability, allows the electromagnetic properties to be deduced [18].

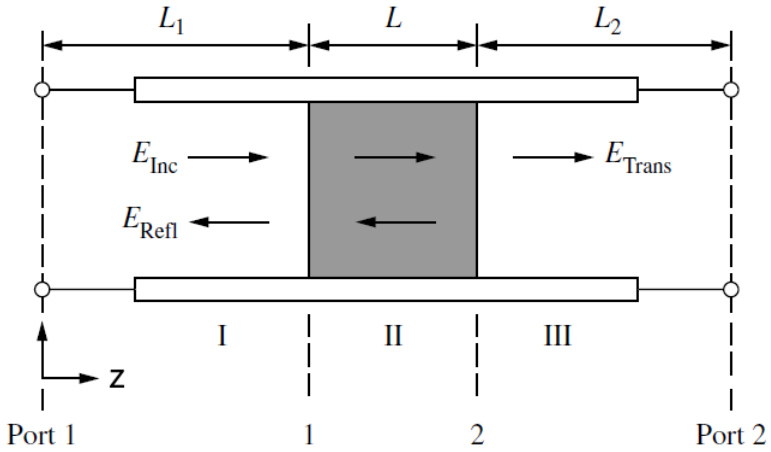

Figure 9 - EM Waves travelling through, and reflected by, a dielectric medium in a transmission line [18]

In Figure 9, the transmission line is divided into three sections along the z-axis which is the direction of wave propagation; air (I), sample material (II), and air (III). Their corresponding lengths and electric fields are L_1, L, L_2, E_I, E_{II}, and E_{III} respectively. The total length of the line is $L_{air} = L_1 + L + L_2$.

For intensity normalized incident waves, their behaviour in all three sections of the transmission line can be expressed as follows [18]:

$$E_I = e^{-\gamma_0 z} + C_1 e^{\gamma_0 z}$$

$$E_{II} = C_2 e^{-\gamma z} + C_3 e^{\gamma z}$$

$$E_{III} = C_4 e^{-\gamma_0 z}$$

where $C_{1\ldots4}$ are constants relating the amplitude/intensity of their respective terms to that of the incident wave's (since it's normalized). Constants γ_0 and γ are propagation constants of the wave in free-space and within the sample medium respectively and are expressed as [18]

$$\gamma_0 = j\sqrt{\frac{\omega^2}{c^2} - \left(\frac{2\pi}{\lambda_c}\right)^2}$$

$$\gamma = j\sqrt{\frac{\omega^2 \mu_r \varepsilon_r}{c^2} - \left(\frac{2\pi}{\lambda_c}\right)^2}$$

where c is the speed of light in a vacuum and λ_c is the cut-off wavelength. Transmission lines operate in the TEM mode with the lowest operable frequency being 0 Hz, equivalent to a cut-off wavelength of ∞ [18] [13] [7]. In order to solve for the unknown constants, we have to set boundary conditions for the fields. Since the electric and magnetic fields are tangential to the surface (orthogonal to the direction of propagation z), we have to ensure they are continuous at the interfaces. It is also assumed that no surface currents are generated. This is satisfied by the conditions [18]

$$E_I|_{z=L_1} = E_{II}|_{z=L_1}$$

$$E_{II}|_{z=L_1+L} = E_{III}|_{z=L_1+L}$$

$$\frac{1}{\mu_0}\frac{\partial E_I}{\partial z}\Big|_{z=L_1} = \frac{1}{\mu_0 \mu_r}\frac{\partial E_{II}}{\partial z}\Big|_{z=L_1}$$

$$\frac{1}{\mu_0\mu_r}\frac{\partial E_{II}}{\partial z}\Big|_{z=L_1+L} = \frac{1}{\mu_0}\frac{\partial E_{III}}{\partial z}\Big|_{z=L_1+L}$$

If we solve the three electric field equations subject to the boundaries above, we obtain the S parameter equations associated with the transmission and reflection of an incident wave through the material [18]:

$$S_{11} = R_1^2\frac{\Gamma(1-T^2)}{1-\Gamma^2T^2}$$

$$S_{22} = R_2^2\frac{\Gamma(1-T^2)}{1-\Gamma^2T^2}$$

$$S_{21} = S_{12} = R_1R_2\frac{\Gamma(1-T^2)}{1-\Gamma^2T^2}$$

where R is the reference plane transformation of the respective port, Γ is the reflection coefficient, and T is the transmission coefficient described by the following expressions respectively [18]

$$R_i = e^{-\gamma_0 L_i}$$

$$\Gamma = \frac{\sqrt{\mu_r/\varepsilon_r}-1}{\sqrt{\mu_r/\varepsilon_r}+1}$$

$$T = e^{-\gamma L}$$

CHAPTER 3 Laboratory Setup and Measurement Procedures

3.1 Test Materials

3.1.1 Rexolite

Rexolite is a cross-linked polystyrene with well-known dielectric properties. Its permittivity has been studied extensively with various techniques and in a wide range of frequency bands. It is a rigid plastic and easy to machine to tight tolerances. Due to its low loss and desirable mechanical properties, it was chosen as an ideal solid MUT to machine and study in order to affirm the validity and accuracy of the transmission line method [21] [22].

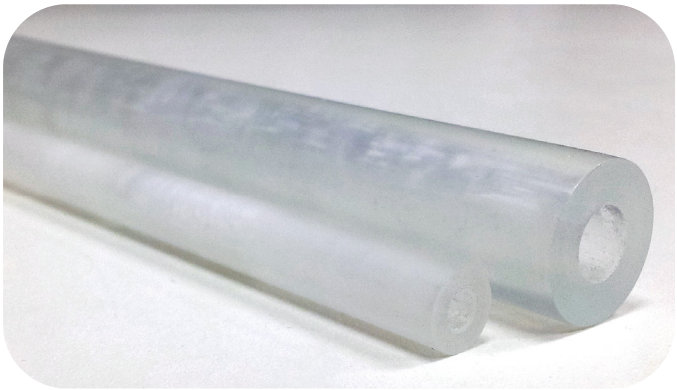

Figure 10 - Machined Rexolite Rods for 7 mm and 14 mm Airlines

One Rexolite rod each was machined for the 7 mm and 14 mm (15 cm length) airline respectively. They were machined with fine tolerances to provide a tight fit and closely match the airline dimensions. The purpose of the rods is to study and determine the accuracies of the transmission line technique when measuring well-behaved solids with stable and well-known dielectric properties. Furthermore, it allows us to determine the effects of known air-gaps due to limitations in machining and how well air-gap correction algorithms perform in order to mitigate said errors.

3.1.2 Teflon

Teflon is the most famously known brand of Polytetrafluoroethylene (PTFE). Commonly used as a coating for non-stick cookware, it is a solid that exhibits great dielectric properties. Since it is much more pliable than Rexolite, it is not ideal for machining into large rods as it will deviate from desired tolerances. Instead, the Teflon was purchased and machined into sample containment caps; one for the 7 mm airline and another for the 14 mm airline.

Coaxial airlines are open ended, rendering it difficult to insert and contain materials that are not solid. Pouring liquids or powders is quite challenging as they will immediately leak into the threads and adapter connectors, potentially causing irreversible damage. Two Teflon end caps, for the purpose of sample containment, were machined and placed at the bottom of the vertically mounted airline. Although they possess the same cross-sectional surface area as the Rexolite rods (same inner and outer diameter), they were only 0.050" in thickness/length. Its equivalent wavelength is equal to that of a 240 GHz wave travelling in free space. This insures minimal wave disruption as approximately 99% of the total fillable volume is still occupied by the MUT and not the Teflon end cap. Furthermore, Teflon has been used in numerous permittivity studies of liquid materials due to its ultra low loss and low dielectric constant that is consistent over a wide range of frequencies [23] [24].

3.1.3 Alumina Grit

Industrial grade pure white alumina, or aluminum oxide, grit was chosen as the main semi-solid material to study and provided by Kramer Industries. It is a low loss material with a relatively high dielectric constant from a geological stand point [25]. It is commonly used as polishing grit due to the abrasive properties stemming from its hardness. The purpose of using alumina is to study and determine the accuracies of the transmission line technique, and the novel in house designed fixture, when measuring

powders with stable and well-known dielectric properties. It is also the second most abundant mineral on the moon [26].

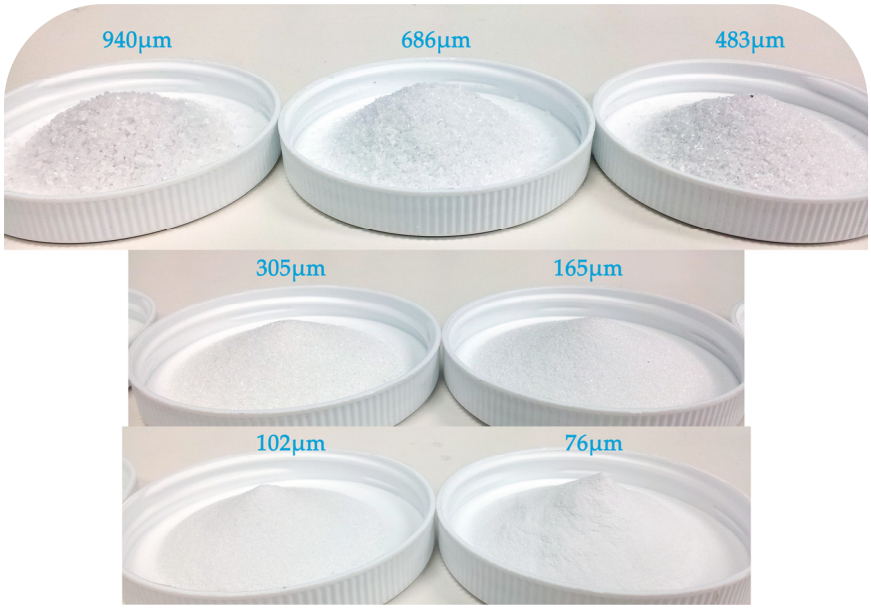

Figure 11 - Various Grain Sizes of Alumina Grit

The relationship between the permittivity and porosity of sintered alumina has been studied in the past [25]. Seven average grain size batches, ranging from 76 – 940 µm, of the material were used in order to draw parallels between the results found using the transmission line technique and previous reports. The grain shapes are angular/sharp, rendering them difficult to sieve in house as they may vary drastically along different axes. The presence of trends and the ability to detect changes in loss tangent with varying grain size are expected. Ideally, these results will coincide with previous works. The alumina samples were provided by Kramer Industries.

3.1.4 Silica Sand

Silica, also known as silicon dioxide, is commonly found occurring in nature as quartz. It is abundant on Earth and readily available in its pure form. It is the most abundant mineral found in lunar highlands, which makes it interesting in terms of space

applications [26]. The silica sand used was provided by Sigma-Aldrich and spherical in particle shape. It was sieved in house to a particle size distribution ranging from 150 to 250 μm.

3.2 Measurement System

3.2.1 Vector Network Analyzer

Electromagnetic waves entering and travelling within a medium travel slower than in free space [9]. Once a wave meets a medium after travelling through free space, it will do a number of things. The extent to which it is affected depends on the inherent properties of the material. There is the incident wave, which is directed towards the material, but there will also be resulting reflected and transmitted waves, which have slightly different characteristics than the incident wave [7]. Normally, the wavelength and velocity of the wave decrease as it passes through the medium (assuming it has a different refractive index from the reference medium). Furthermore, the magnitude (or amplitude) of the wave is attenuated [9]. A Vector Network Analyzer, or VNA for short, can be used to characterize these changes [20].

VNAs are typically 2- or 4-port networks, and have the ability to measure the network parameters of these electrical networks [20]. A VNA consists of a signal source, a receiver, and a display [9]. It sweeps through different signal source frequencies and tunes its receiver to these frequencies to measure the transmitted and reflected signals of a sample. They commonly measure S parameters which provide information about the electrical behaviour of the network once stimulated by an electrical signal [27]. As seen in Chapter 2, S parameters can be used to derive the dielectric properties of a medium in a network [27]. Algorithms to convert these parameters to permittivity and/or permeability results are well established and published in papers, and can be written via a programming language to communicate with the measurement device and convert the S parameters on an external computer.

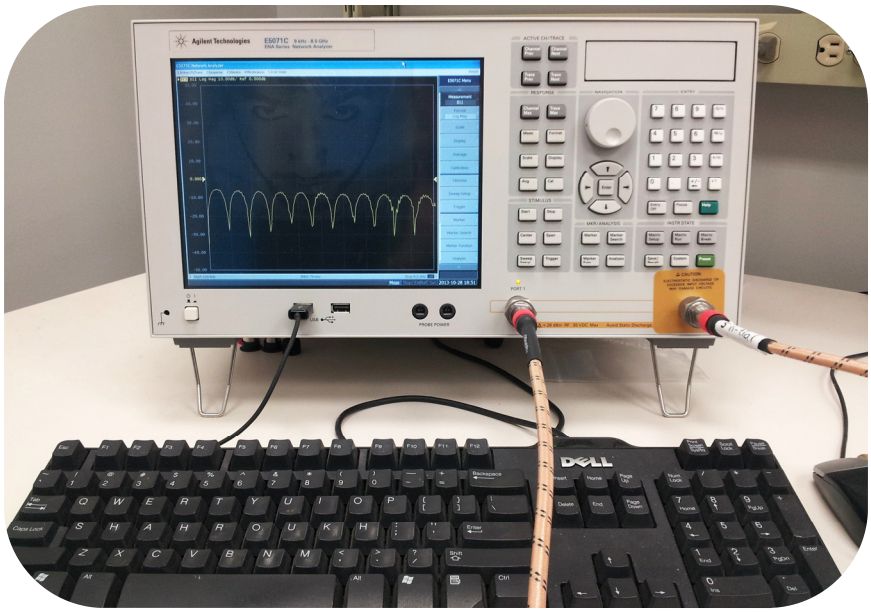

Figure 12 - Agilent E5071C-280 ENA series Vector Network Analyzer

The particular model used to measure the test material S parameters for this research is the Agilent E5071C-280 ENA series VNA. It is a 2-port network device with a test frequency capability spanning from the low frequency radio band to just above the X band; precisely ranging between 9 kHz to 8.5 GHz. Both ports have Type-N female connectors for connecting passive and active devices. The signal source power range is from -55 dBm to +10 dBm, with a receiver dynamic range of over 123 dB. This VNA has a trace noise level below 0.004 dBrms and has a temperature stability of 0.005 dB/°C. The E5071C-280 is also able to measure a maximum of 20,001 points evenly distributed along the specified frequency range. For simplicity, it is equipped with a 10.4 inch XGA color LCD touch screen with a Windows XP Open operating system [28].

3.2.2 7 mm and 14 mm Coaxial Airlines

A coaxial airline consists of a hollow cylindrical transmission line. The inner walls have a smooth contour and acts as the sample holder. Both outer ends are threaded to secure the connectors to both test ports on a Network Analyzer. A center conductor runs

through the center of the hollow cylinder and provides the connection, and is secured in place by the threaded cables on both sides. This implies that the sample must be manufactured into a toroid; a cylinder with a hole in the center.

Figure 13 - HP and General Radio Coaxial Airlines

This technique is considered destructive; a solid MUT has to be machined and prepared in a toroidal shape in order to perform the measurement [9]. It is advised that semi-solids (powders) and liquids not be used; however sample containers and end-caps can be machined in order to house them. The inclusion of such a container would require de-embedding; that is to say that the effects of this new material must be calibrated out to ensure the powder is being measured [29]. However, the effects of the container or end-cap are generally ignored if it is relatively thin in comparison to the total fixture length and has a negligible effect on the permittivity.

A series of coaxial airlines are used for the experiment. The HP (now Agilent) 85051B Verification Kit contains both a 25 Ohm mismatched and 50 Ohm impedance matched airline, both of which have a 7 mm outer diameter, 9.9898 cm electrical length, and spring-loaded supporting tips to mate with APC-7 sexless connectors. Only the 50 Ohm

line is used for measurements for the experiments, as it matches the impedance of the VNA, and has an inner conductor with a 3.04 mm diameter. The operational frequency range is DC to 18 GHz. The environmental requirements to ensure that the calibration conforms to its specifications is an operating temperature range of 20°C to 26°C and non-condensing relative humidity between 0% to 95% [30]. The General Radio Reference-Airline Set contains seven airlines from the 900-LZ series, ranging in length from 2.998 cm to 29.979 cm. All of the coaxial lines have an impedance of 50 Ohms. . The operational frequency range is DC to 8.5 GHz, with similar environmental requirements as the HP airlines [31].

Due to the destructive nature of this technique with solid material, as the technique is intrusive and involves some level of sample preparation, it is not favourable for fast repetitive measurements [8]. Fortunately this method has good accuracy in ϵ_r' measurements and has the ability to measure medium-low to high $\tan\delta$ [29]. It is assumed that the MUT is homogenous and that the faces perpendicular to the long-axis are completely flat and smooth. If the MUT is not uniform in composition then the resulting measurement is assumed to be a weighted average in mass [9]. Assuming that the common sources of error are removed, the accuracy for coaxial airline measurements is ±5% for low to medium dielectric materials [1]. Loss tangent can vary by ±0.01, however, air-gaps can drastically reduce these nominal accuracies [8].

3.2.3 7 mm and 14 mm Calibration Standards

In order to begin using the 7 mm lines, the Agilent 85031B Calibration Kit is needed. It consists of a combination open/short-circuit termination and two 50 Ohm loads. These are precision fixed devices with an APC-7 connection interface. The environmental requirements to ensure that the calibration standards conform to their specifications is an operating temperature range of 15°C to 35°C and non-condensing relative humidity between 0% to 95%. The error-corrected range for any measurement is ±1°C from the calibration temperature [32].

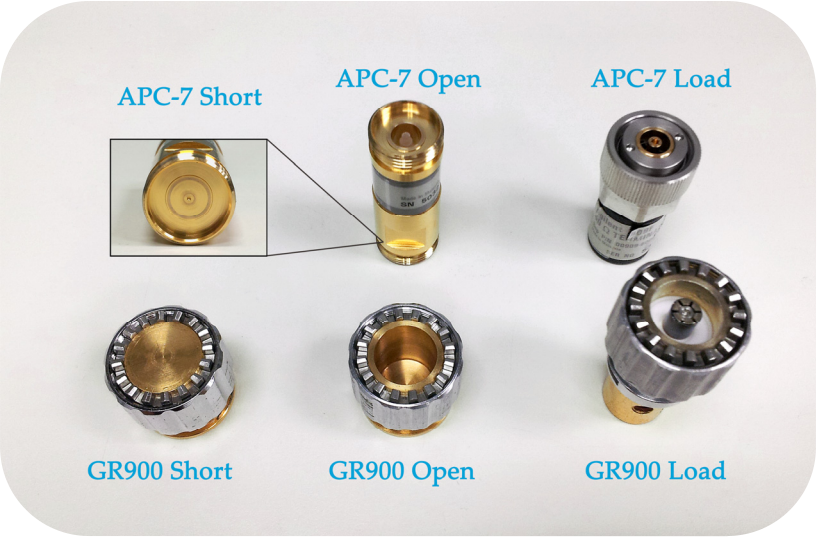

Figure 14 - APC-7 and GR900 Calibration Standards

The General Radio GR900 connector type calibration standards are intended for use between DC to 8.5 GHz, and calibrate the VNA for 14 mm airline use. Due to the design of the GR900 connectors with a centering gear ring and locking nut which cause butt contact between conductors, insertion loss and insertion phase are highly repeatable. The 900-WN short-circuit termination is a fixed position short with a reflection coefficient >0.999. The 900-WO open-circuit termination has a measurement plane position of 0.26 cm and a capacitance of 0.172 ± 0.008 pF at low frequencies. Two standard 50 Ohm loads, the 900-W50, were used as well [31].

3.2.4 Adapters and Cables

Two high stability Microwave/RF cables from Maury Microwave are used to connect the calibration standards and the airlines to both ports of the VNA. The Maury SC-N-MM-48 cables are four feet in length with a Type-N male to male connection. They are rugged and standardized for high-performance applications such as VNAs, bench-top testing, and RF production testing. The main benefit for research is the amplitude and phase stability, with cable flexure, of ±0.015 dB and ±2° respectively. They operate up to a maximum frequency of 18.0 GHz and are crush, fire, and abrasion resistant [33].

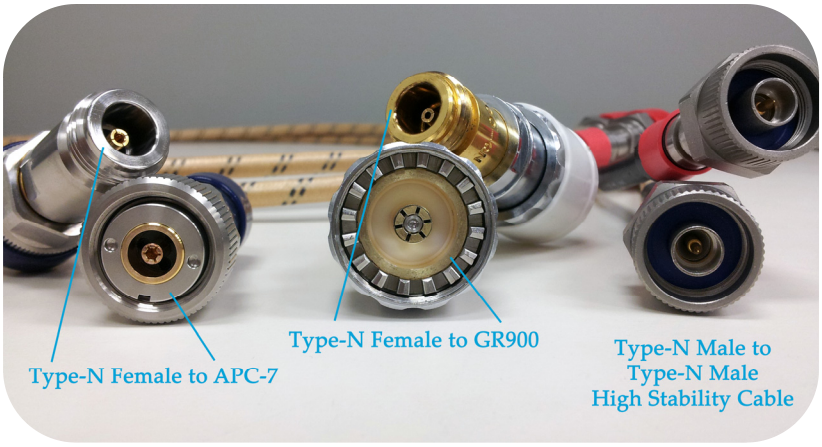

Figure 15 - APC-7, Type-N, and GR900 Adapters and Cables

In order to connect the airlines and calibration standards to the high stability cables, a series of adapters need to be used since the cables have Type-N male connectors. Two Maury Microwave 2606C Type-N female to APC-7 adapters were used in order to connect to the 7 mm airline and calibration standards. The centre conductors are heat treated gold-plated beryllium copper for durability and offer high repeatability. They are rated to operate from DC to 18.0 GHz [33]. For the 14 mm airline and calibration standard connections, two General Radio 900-QNJ Type-N female to GR900 adapters were used. The operational frequency ranges from DC to 8.5 GHz [31]. All adapters are matched with a nominal impedance of 50 Ohms.

3.2.5 High Accuracy Scale

When dealing with semi-solid materials, it's important to have both reliable and accurate measurements of their total mass. This is useful in order to place the permittivity measurements in the appropriate context when comparing them to other studies. Since the total sample occupied volume of an airline is measurable, and the particle density of the material is known, having an accurate balance to weigh the sample will allow an accurate measurement of its porosity. The permittivity of any material is dependent on its packing fraction.

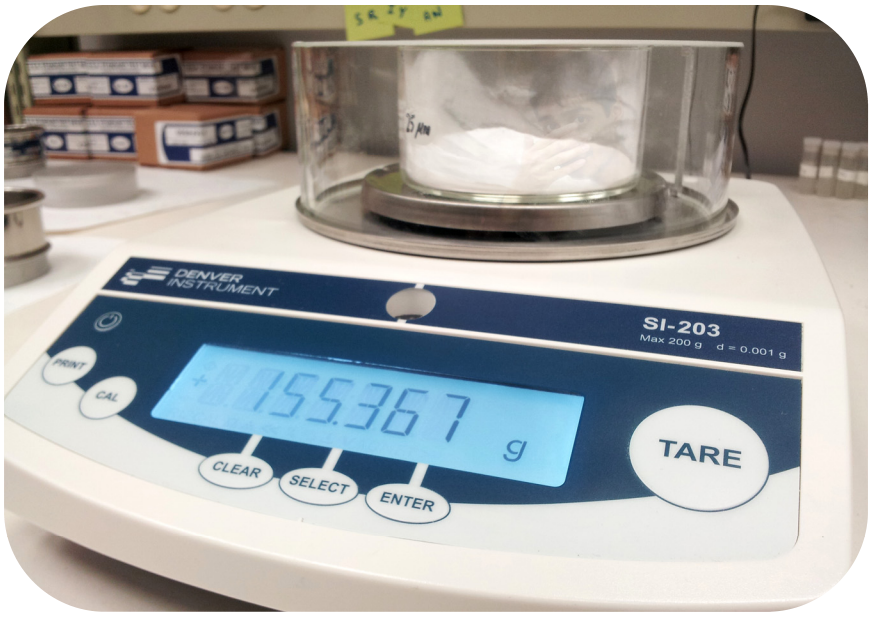

Figure 16 - Denver Instrument SI-203 Summit Series Digital Scale

The Denver Instrument SI-203 top-loading, digital balance is both an accurate and reliable instrument. It is able to weigh materials and display the results on a back-lit digital display in various units including grams, ounces, and pounds. A bubble level and leveling feet are built in for balanced and stable measurements. It is internally automatically calibrated at the touch of a button. The readability and repeatability of this particular model is ±1 mg with a maximum capacity of 200 grams [34].

3.2.6 Test Platform

Perhaps the most challenging aspect of the coaxial airline is the process of filling it with a semi-solid MUT. It is very important for concentricity, in other words a perfectly centered inner conductor, to be maintained. Although this can be easily avoided with careful machining for solid test materials, thus reducing any air-gaps that lead to cylindrical deviations, it is harder to handle for semi-solids that may be packed very densely. This is one of many causes of measurement errors [18]. A novel approach was taken to handle this issue that has yet to be encountered in other works.

In order to address this issue, a semi-solid sample preparation fixture was machined and retro-fitted onto the Gilson Performer III Sieve Shaker. The importance of this fixture is twofold; to facilitate the filling of the airline with powdered samples and to densely and uniformly pack said material. The vibrating base plate and aluminum threaded rods were machined to resemble those included with the sieve shaker, although the rod

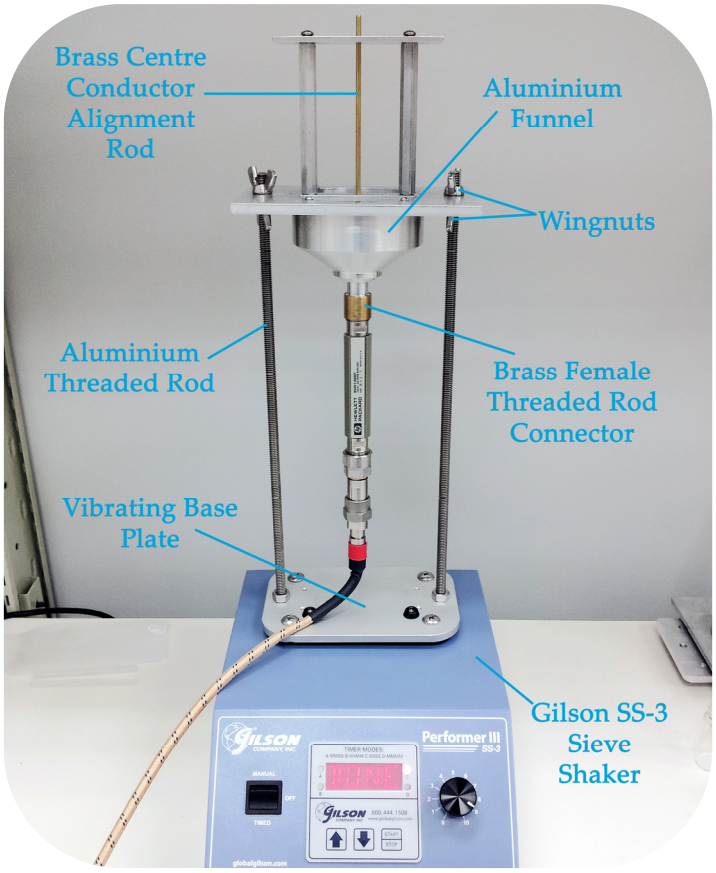

Figure 17 - Semi-solid Sample Preparation Fixture

length was extended in order to accommodate longer airlines. An aluminum plate with an attached funnel was designed, machined, and secured to the rods using wingnuts on either side. An extra plate was added above it and attached with hex spacers. Within the funnel, a small and perfectly centered hollow ring was fastened with a 3 mm hole drilled directly in its centre. The supporting plate of the funnel, as well as the extra plate

positioned above with hex spacers, also had a 3 mm hole centered in alignment with this ring. These three holes acted as a precise guiding system for the brass centre conductor alignment rod, machined with fine tolerances. Once the airline is secured to the funnel using the brass female threaded rod connector, the brass alignment rod is slid into position to come into contact with, and to secure, the centre position of the inner conductor. It should be noted that two sets of funnels and alignment rods were machined; one for the 7 mm airline and one for 14 mm airlines.

The Gilson Performer III Sieve Shaker was used for two reasons: it is a useful device for sieving semi-solid samples and for packing MUTs into the airline. The sieve shaker is designed to be compatible with a wide array of stainless steel and electroformed mesh sieves which are purchased individually, ranging from 4.75 mm to 75 μm for individual particles with opening tolerances of ±2 μm. A tapper assembly is also included that is fastened to the threaded rods with captive knobs with release buttons. This is particularly useful for fine particles that begin to clump and may become isolated due to frictional forces. The Gilson Performer III has a tapping and vibratory frequency of 60 taps/min and 3600 vpm respectively. In addition, a timer and amplitude control knob are included [35].

3.3 Measurement Procedure

3.3.1 Sample Preparation

Sample preparation is a crucial part of the measurement procedure. Both solid and semi-solid (powder) materials need to be well prepared prior to taking measurements. Solid samples were machined into toroids. This is a solid cylinder with a hole in the form of a smaller cylinder passing through its centre, also referred to as a cylindrical shell. The outer diameter of the toroid is the same as the Coaxial Airline's outer conductor, while the inner diameter is the same as its centre conductor. Fine and accurate machining was

necessary in order to eliminate any air-gaps that would have a negative effect on the measurement. Machining was particularly useful for the Rexolite and Teflon samples.

Air-gaps and sample length requirements not being met are common sources of error for solid materials. Air-gaps are created if the MUT doesn't fit the sample holder's cross-section and make contact with the walls [9] [8]. Sample dimensions do not need to satisfy the requirement to be "infinite" in size. This is advantageous as foreign samples

Figure 18 - Thermal Product Solutions Tenney Junior Temperature Test Chamber

such as planetary analogue materials aren't always readily available in large quantities. It should be noted that low loss resolution does depend on the length of the sample confined within the airline or waveguide [8]. It is therefore crucial to have samples fill

the entire length of the line as best as possible without affecting performance. Greater measurement accuracy can be achieved as the ratio of the sample air-gap relative to its own width/diameter decreases [1] [36].

Semi-solids such as alumina and silica were purchased as readily available in different grit and grain sizes. All rocks and other geological material were reduced to powder using a mortar and pestle or swing mill to grind and pulverize the material. This is especially of use when performing an analysis of the effects of porosity on the permittivity of the test material. Once ground and pulverized, a sieve shaker was used on the non-organic granular material to assess and obtain specific particle size distributions.

	Grain Size [μm]						
	76	102	165	305	483	686	940
Mass (Before) [g]	186.163	190.603	193.279	197.084	196.956	191.232	198.264
Mass (After) [g]	186.067	190.543	193.241	197.050	196.925	191.202	198.185

Table 1 - Effects of baking Alumina for a total of 48 hours at a constant temperature of 200 °C

Depending on the melting point of the material, an oven can be used to bake the geological material. This is of great importance as even the slightest bit of trapped moisture will negatively impact the permittivity due to the high dielectric constant and loss of water at room temperature. All geological materials were baked for a total of 48 hours at a constant temperature of 200 °C. The significance of this step in sample preparation was observed once 7 alumina samples of different grain sizes were weighed both before and after baking, as seen in Table 1. Plastics such as Teflon and Rexolite were not baked due to expected irreversible sample deformation.

3.3.2 Test Equipment Handling and Measurement Preparation

The current laboratory test setup consists of the Agilent 85051B coaxial airline and 85031B mechanical calibration kit, General Radio 900-LZ series Reference-Airline set and its corresponding GR900 calibration standards, and the Agilent E5071C network analyzer. The particular airline in use is connected to Ports 1 and 2 of the VNA via two Type-N male to Type-N male cables, each with its own Type-N female to APC-7, or GR900, adapter. In order to perform as accurate a measurement as possible, the VNA is initially run for 2 hours in order to stabilize the temperature of its internal components. It is then calibrated prior to data acquisition using the respective kit's Short, Open, and Load standards. This procedure ensures that transmission and reflection remain constant along all frequencies for a simple through measurement (Port 1 connected directly to Port 2).

Calibration is a process that spans a total of 45 minutes. First, it is important to select the kit being used through the calibration menu of the VNA. The calibration coefficients, or "electrical identity" so to speak, of each standard is preprogrammed into the VNA. The calibration menu of the VNA provides us with a number of options; however the full 2-port calibration was used. This is often referred to as the Short, Open, Thru, and Load (SOTL) technique. There are two mandatory, and one optional, steps to complete for this calibration method; Reflection, Transmission, and Isolation (optional). The Reflection step involves individually connecting a Short, Open, and Load to the measurement planes of each port. The calibration/measurement plane is at the end of each APC-7 or GR900 connector. For Transmission, the APC-7 or GR900 connector from Port 1 is connected directly to that stemming from Port 2. This is called a Thru measurement. Finally, the Isolation option involves placing a 50 Ohm load on each port which is measured simultaneously. Although this is optional, it was done nonetheless as it prevents a certain degree of cross-talk which will be discussed in the next chapter [37]. An important detail is the tolerance of how tightly the APC-7 and GR900 connectors can

be connected. A 12 in-lb precision HP 1250-1874 torque wrench was used to secure all connections to avoid connector damage [38].

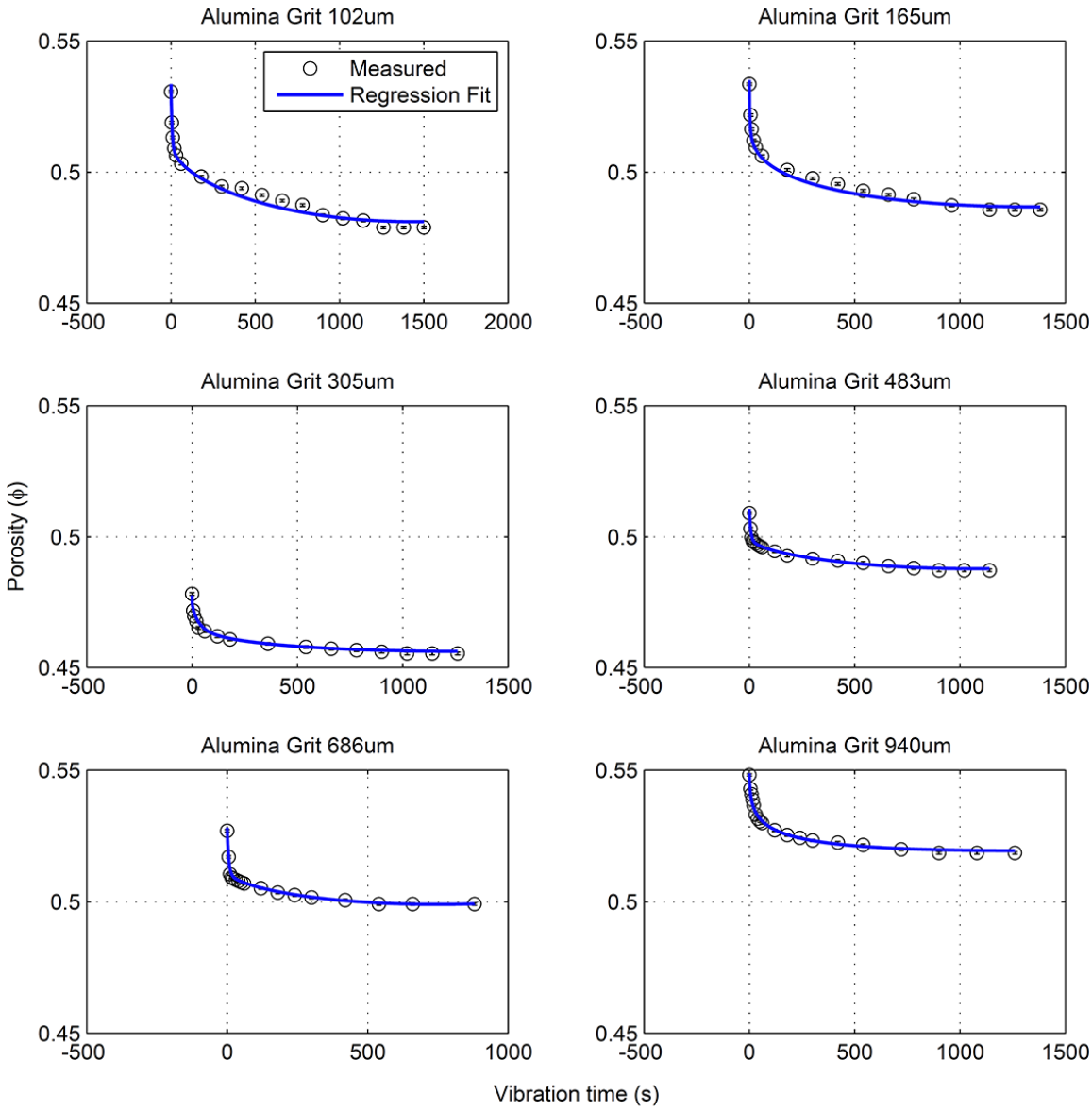

Figure 19 - Packing Curves for Alumina Grit

To avoid calibration drift with time, the samples are prepared simultaneously as calibration occurs. This is applicable to powdered samples only as solid MUTs can be inserted into the line in negligible lengths of time. During this process, the airline in

question is initially attached to the semi-solid sample preparation fixture. The semi-solid MUT is poured to the edge of the outer conductor, which is observed through the top of the aluminum funnel with an LED flashlight; the sieve shaker is used to pack the material more densely. Material is then poured in once again since a certain level of settling has occurred. Once the MUT has reached its packing limit and no more material can be added (as seen in Figure 19), the airline is detached from the fixture. Quick-grip clamps are used to prop the airline vertically and the cable from Port 2 is connected to

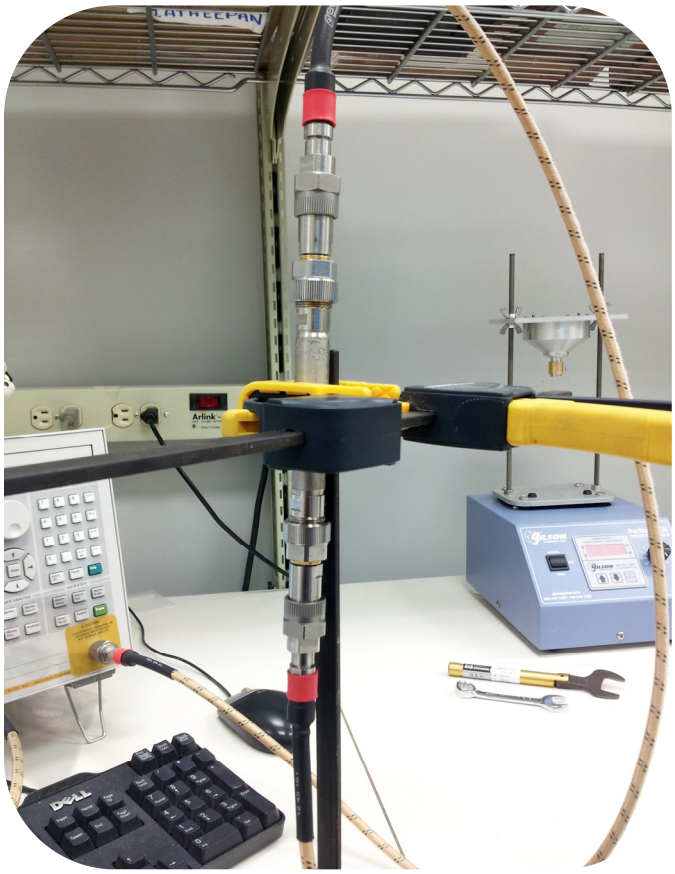

Figure 20 – Sample-filled Airline Mounted Vertically for Permittivity Measurements

the open end of the airline. This is the final position of the sample-filled coaxial airline prior to measurement.

It should be noted that powder-free latex gloves were used for handling all equipment during sample preparation. Furthermore, extra care was taken to clean all contacts, measurement planes, calibration standards, and airlines with >99% isopropyl alcohol and lint-free swabs. Scientific Precision standard Kimwipes were used for cleaning sensitive areas very carefully and also for drying components in conjunction with compressed air. Cleaning was performed both before and after measurements as a precautionary measure. Although unnecessary due to the instant evaporation of a lightly applied layer of isopropyl alcohol, the cleaned surfaces were left to dry for at least 15 minutes. For personal safety, a breathing mask for fine particulates and safety glasses were also used.

3.3.3 Data Retrieval and Storage

The VNA has the option to save trace data to a tabulated text file. Each row consists of one column containing the measurement type and another with the frequency at which the measurement was taken. Each measurement runs for approximately 6 minutes before termination. The unitless magnitude, phase in degrees, and group delay for S parameters S11 and S21 were in their own respective text files and stored in a USB key. This was then transferred over to the data processing computer for analysis. In addition, a LabVIEW VI script can be written to communicate with the instrument via the rear-panel GPIB port in order to extract the data and facilitate data processing. However this option was not considered.

CHAPTER 4 Data Handling and Error Analysis

4.1 Calculating Permittivity

There are a series of data conversion techniques used to calculate the permittivity and permeability values of materials based on initial S parameter measurements. Parallel-plate capacitance and resonant cavity techniques do not rely on the measuring of S parameters and have straightforward equations to extract the permittivity. Furthermore, air-gaps are typically calibrated out using test equipment for the free-space technique and are of no concern for resonators. However, transmission/reflection line techniques rely on S parameter measurements and consequently depend on dimensional constraints, such as sample length, that affect accuracy.

Various popular techniques, such as the Nicholson-Ross-Weir (NRW), NIST, and NIST Non-Iterative, are used to convert these parameters to permittivity values [29]. The computations are lengthy and will not be presented. However an overview of advantages and disadvantages will be discussed below.

4.1.1 Nicholson-Ross-Weir Algorithm

The NRW method is a combination of ideas put forward initially by Nicholson and Ross in 1970 and then Weir in 1974 [39] [40]. Both the forward and reverse S parameters (S11, S21, S12, and S22) are used to derive the reflection and transmission coefficients of the material and thus the permittivity. S parameters S11 and S21 (forward) can be used alone to perform the calculations as well. The NRW algorithm is most commonly used for data conversion in transmission/reflection line measurement techniques, mainly for short and lossy solids [29].

The NRW technique is fast as it is not computationally intensive due to its non-iterative nature. Also, both non-magnetic and magnetic material can be measured to also obtain

the permeability of the sample. Unfortunately this is a trade-off as it has medium accuracy due to a number of disadvantages. It is not suitable for low-loss materials at frequencies that are multiples of one half-wavelength in the sample. The optimum sample thickness is one fourth of the wavelength, which is why samples are to be kept short. These areas also will diverge drastically from the rest of the measurement spectrum and cause spikes in the broadband analysis of the MUT's electrical properties. This is due to the phase uncertainty measured by the VNA having a strong influence on small S parameter values. A remedy would be to reduce the sample length. However the extent to which this is done depends on the permittivity and permeability which is presumed to be unknown at the time of measurement [29].

4.1.2 NIST Non-Iterative Algorithm

Baker-Jarvis et al. designed the NIST Iterative technique in 1990 as an improvement to the NRW technique. It is intended to recover and stabilize the permittivity spikes that arise from using the aforementioned technique [41]. As with the NRW technique, both the forward and reverse S parameters are used to derive the permittivity. However S11 and S21 can be used alone to perform the calculations as well. A root finding technique (Newton-Raphson) is used to offer stable solutions and determine the MUT's permittivity without increasing the computational difficulty. It is a commonly used algorithm for transmission/reflection line and high-temperature free-space techniques [29].

This technique is advantageous as the samples can be of arbitrary length, since the inaccuracies caused by having sample lengths that are multiples of one half-wavelength are eliminated. This implies that, in contrast to the NRW method, the NIST iterative technique is suitable for low-loss samples [29]. The uncertainty is inversely proportional to the length of the sample [41]. The results are smooth and stable across a very broad range of frequencies. This makes it highly accurate. As it is iterative, computations are extremely slow with an average processor. Unfortunately, an initial guess of the

permittivity is required which is problematic for new materials. Furthermore, it is assumed that the relative permeability of the sample is 1 (i.e. non-magnetic) [29].

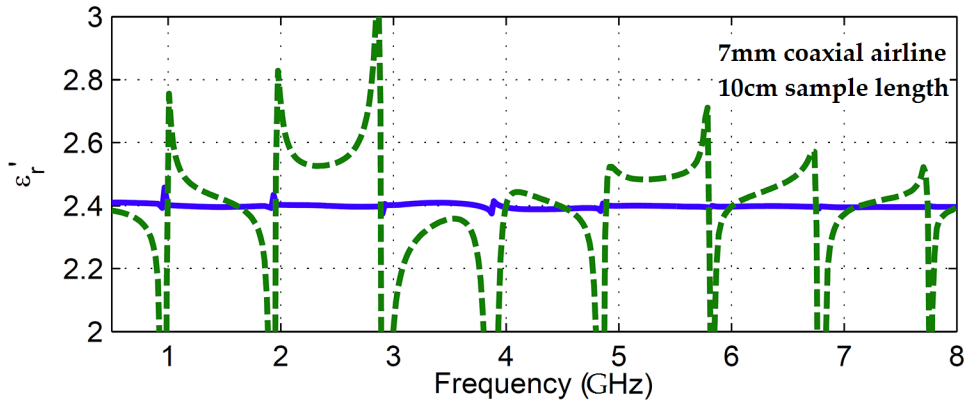

Figure 21 - Dielectric constant of Rexolite (raw) v. frequency as determined by the NRW technique (dashed green line) and the NIST Iterative technique (solid blue line)

In 1997, Boughriet et al. sought to combine the positive aspects of the NRW technique with that of the NIST Iterative technique; the NRW technique being a fast conversion technique with medium accuracy whereas the NIST Iterative technique is slow but possesses higher accuracy [42]. Again, S11 and S21 can be used alone to perform the calculations as well. It is commonly used for transmission/reflection line and high-temperature free-space techniques [29].

The Non-Iterative technique is non-divergent throughout the full frequency spectrum of measurements and provides smooth results. Arbitrary sample lengths can be used and will not affect the accuracies. Unlike the Iterative counterpart by Baker-Jarvis et al. (1990), there is no initial guess of permittivity needed. As there is no iteration involved in the calculations, the data conversion process is much faster than the NIST Iterative technique [29]. The uncertainty for materials with various loss-types, including low-loss, is comparable to the high accuracy of the NIST technique [42]. It is assumed that the relative permeability of the sample is 1; therefore it is ideally used for non-magnetic MUTs [29].

4.2 Vector Network Analyzer Error Sources and Mitigation

4.2.1 Systematic Errors

Systematic errors are characterizable errors caused by limitations in the VNA resulting from unwanted reflections, signal leakage, and frequency response errors. There is no precise dependence or relationship between these errors and time, however they are considered repeatable. Systematic errors comprise directivity, tracking, source and load match, and dynamic accuracy errors. All except the latter are quantifiable and characterized during a full two-port calibration, then reduced, if not completely eliminated, thereafter. However some residual errors persist and may never be completely removed due to calibration standard imperfections [43].

4.2.1.1 Directivity

When performing reflection measurements, the limitation in its dynamic range is attributed to directivity errors. Before the device under test (DUT) or MUT receives the signal, it initially passes the reflected wave detector of the VNA. The vector sum of all the signals initially reaching this receiver is known as directivity. This sum may include leakage signals that are detected but never reflected by the DUT or MUT, thus accumulating error [18].

4.2.1.2 Tracking

Tracking errors are frequency response errors that occur in both the reflection and transmission of signals, where the signal path of the test receiver does not completely track that of the reference receiver [43]. This arises from losses occurring along the path, delays in phase, and imperfections in the detectors hindering their response [18].

4.2.1.3 Source/Load Impedance Matching

Source and load match errors arise due to impedance mismatches as seen by the DUT looking back to Port 1 (source) and into Port 2 (load) respectively. The entire signal reflected and/or transmitted by the DUT is ideally received by the source and load

receiver of the VNA. However various internal reflections and reflections off of Ports 1 and 2 are never received and ultimately unaccounted for by the respective receiver [43].

4.2.1.4 Dynamic Accuracy

Dynamic accuracy errors are dependent on the input power level (dBm) of the source signal and are specified in decibels. It is the only type of systematic error that cannot be eliminated and is most often not reducible. Dynamic accuracy errors mostly comprise of compression and cross-talk errors. Compression is a non-linear behaviour in a receiver characterized by a reduction in gain at high input signal levels. Cross-talk is leakage signal from Port 1's receiver to that at Port 2 without having passed through the DUT. The dynamic range of a receiver is the linear region between the compression zone and the cross-talk and noise floor [43].

In order to avoid receiver compression, an input signal power level of -10dBm was used on the VNA. Averaging over five measurements as well as a specified intermediate frequency bandwidth (IFBW) of 10 Hz were used to reduce the noise floor as much as possible. This allows us to narrow in on the frequency of interest. Furthermore, cross-talk was reduced below the noise floor by performing an isolation calibration as detailed in Section 3.3.2 [43].

4.2.2 Random Errors

Random errors cannot be characterized like systematic errors and are unpredictable. Unfortunately this means that they also cannot be removed by calibrating the system; however their effects can be minimized. Instrument noise, connector repeatability, and cable stability are the main causes of random errors [18].

4.2.2.1 Noise

Noise is dependent on the limit of the sensitivity of the individual components within the VNA [43]. Averaging over five measurement sweeps, as well as using the narrowest

possible IFBW (10 Hz), was done to reduce the noise floor. This however also has the disadvantage of increasing measurement times considerably. Source signal power was also increased to a maximum of -10dBm not only to avoid compression, but to ensure as wide a dynamic range as possible.

4.2.2.2 Connector Repeatability

Connector repeatability depends entirely on the level of torque applied to all connections within the test system [43]. Since many connections are made prior to any measurement when repeatedly connecting and removing standards during calibration, these errors can add up quickly and result in poor repeatability. A 12 in-lb precision HP 1250-1874 torque wrench was used to secure all connections not only to avoid connector damage, but also to have consistency in the applied mating torque. The torque wrench was verified by the manufacturer and calibrated to apply torque within spec.

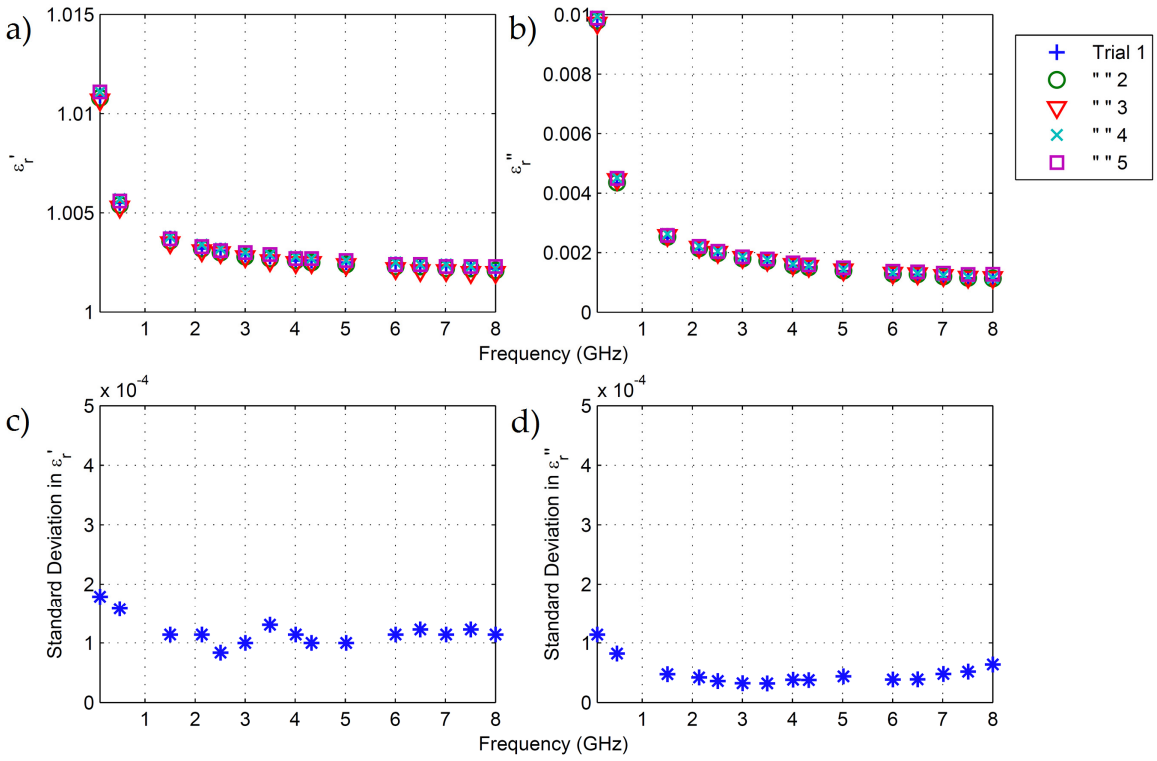

Figure 22 - Connector Repeatability Using a Calibrated 12 lb-in Torque Wrench

In order to evaluate the repeatability of all connections made from calibration to sample evaluation, the entire measurement procedure outlined in Section 3.3 was repeated 5 times for an empty 7 mm airline. An empty airline was chosen since the properties of air do not change in a stable environment; each subsequent measurement of the airline would only be different from the last due to the torquing of the connectors. Each measurement was stored and the standard deviation for both the dielectric constant and loss was calculated at 15 evenly spread frequencies along the entire spectrum.

In Figure 22, we have the five trial measurements of the dielectric constant, loss, and their respective standard deviations. The dielectric constant of air has an average standard deviation equal to 1.0×10^{-4}. It is thought that this is a result of minute differences in torque between measurements having an effect on the apparent length of the line as seen by the calibration planes. The standard deviation of the loss is considerably lower with an average of 5.0×10^{-5}. In Chapter 5 we will see that these results are far below the measurement errors due to the VNA.

4.2.2.3 Cable Stability

Cable quality is the limiting factor that determines cable stability and its influence on the overall achievable measurement accuracy. Cable stability is dependent on its mechanical stability and effects phase measurements. The Maury SC-N-MM-48 cables were chosen as they are rugged and crush, fire, and abrasion resistant. They possess high amplitude and phase stability, during flexure, of ±0.015 dB and ±2° respectively [33]. Moreover, cable flexure and movement was completely avoided during calibration and the bend radii during measurements were kept as large as possible.

4.2.3 Drift & Stability

Drift & Stability errors in the test system hinder its performance, and occur when environmental conditions vary after calibration. If the test environment is stable and the ambient temperature is the same during both calibration and measurement, drift is

minimized. VNA drift is time dependent and is most affected by changes in temperature and humidity [43]. Drift is reset in a sense once calibration is complete. In order to avoid drift errors, measurements were completed immediately after a full two-port calibration. As presented earlier in Section 3.2.3, the error-corrected range for any measurement is ±1°C from the calibration temperature [32]. In order to guarantee these figures, all instances of calibration and measurement were performed in a laboratory with an ambient temperature and humidity of 21.5 ± 1°C and 45 ± 5% respectively. Additionally, the VNA was warmed up for 2 hours prior to calibration in order to stabilize its electronic components.

4.3 Calibration Error Sources and Mitigation

In Section 3.2.3 we saw that the environmental requirements to ensure that both the 7 mm and 14 mm calibration standards conform to their specifications is an operating temperature range of 15°C to 35°C and non-condensing relative humidity between 0% to 95%. Furthermore, the error-corrected range for any measurement is ±1°C from the calibration temperature [32]. However other factors exist that can affect calibration.

As mentioned earlier, all calibration standards have a set of definitions, or calibration coefficients, preprogrammed into the VNA. These definitions are also provided on a separate disk. A terminating short is often assumed to be an ideal short with a reflection coefficient of -1 for large connectors such as an APC-7 and GR900, otherwise a third order polynomial inductance model is used. A third order polynomial capacitance model is used for the open termination. Fixed loads are assumed to have a reflection coefficient of 0 [37]. These definitions are determined by the manufacturer and not the end-user. The calibration standards purchased possess certificates of coefficient verification, and have been taken care of and cleaned from then on in order to avoid any contact surface damage that may alter its guaranteed performance.

Another factor that affects calibration is time. After calibration, a variety of environmental variables such as temperature and humidity may fluctuate and affect the state of the VNA. This fluctuation can be greatly reduced by having a stable ambient temperature, such as that of the lab environment used to perform our measurements; however, calibration drift may still persist due to imperfections in the VNA. It should be noted that drift is a result of the difference in test environment during and after calibration, and does not reflect how accurate the calibration coefficients of the standards are.

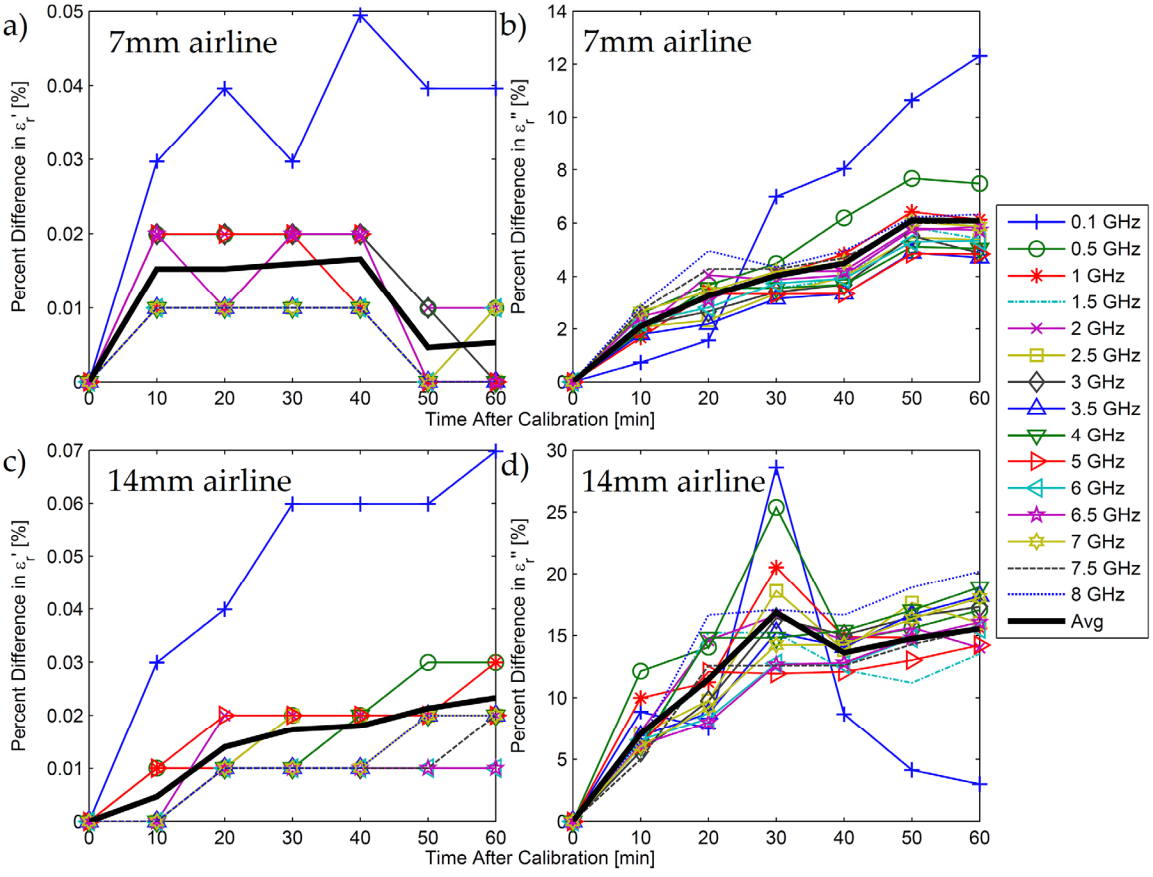

Figure 23 – Air Measurement Drift v. Time After Calibration

In Figure 23, we see the effects of measurement drift with respect to an initial measurement of air (empty airline) performed immediately after calibrating the system

($t = 0$). A measurement was then performed every 10 minutes for a total of 1 hour. In order to generate the data, the percent difference between the initial measurement and each subsequent one thereafter was calculated. This was done for both the 7 mm and 14 mm (10 cm length) airline. Although it is evident from the dielectric constant and loss measurements for both the 7 mm and 14 mm line that the lowest frequencies are affected most, the average drift along the whole frequency spectrum is problematic nonetheless. This is especially true for loss measurements. Even so, a steady increase in drift over time is apparent. It is for this reason that all measurements are performed immediately after calibration in order to minimize the effects of calibration drift.

4.4 Sample Error Sources and Mitigation

4.4.1 Mating Plane Face

As seen in Section 2.1.6, if we have a wave propagating in the +z direction, its electric and magnetic field components are orthogonal to each other as well as to the direction of travel. In the case of a coaxial airline, the wave is travelling through and in the direction of the centre conductor with both field components radiating orthogonally out. It is required that the sample ends be perfectly flat and perpendicular to the centre conductor. Any deviation in flatness would cause the fields to momentarily travel in two

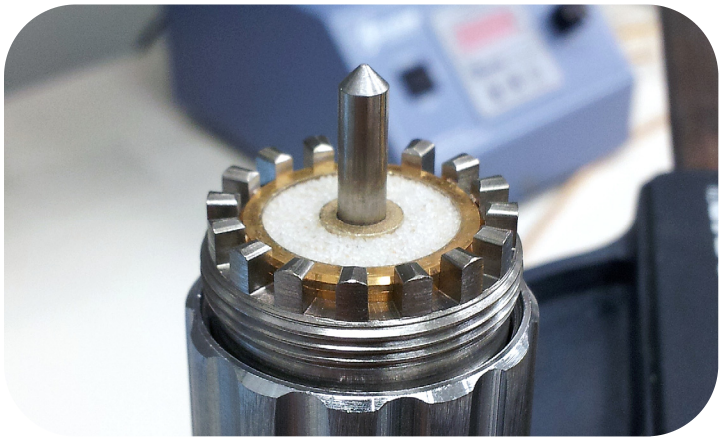

Figure 24 - Granular Sample End in a 14 mm Coaxial Airline

different materials; the sample and air. This will undoubtedly cause unwanted phase changes that will affect the resulting measurement.

Solid samples such as Rexolite were machined to have flat sample ends. Granular materials pose a different problem as the position of individual grains can easily change. Furthermore, after shaking and packing the material, the sample end may not sit flat. In order to address this issue, a flat dummy adapter was pressed against the exposed end of the coaxial airline. This caused the top layer of material to flatten and also collected any excess grains that extended beyond the mating plane. As seen in Figure 24, a flat sample end was achieved using this technique just before measuring the material.

4.4.2 Length

When calibration is performed, the VNA recognizes the calibration planes as the measurement planes i.e. ends of the DUT or MUT. For our measurements to be valid, the calibration planes and sample ends should be one and the same. If any length of transmission line is added between the calibration plane and sample end, phase correction is necessary for the measured S parameters [18]. In order to avoid these unnecessary corrections, solid samples were machined to match the length of the airline and granular materials filled the lines from end to end.

In Figure 25, we see that the total measurement uncertainty due to all S parameter magnitude and phase errors varies according to airline length (error calculations are discussed in Section 4.6). The data was generated by calculating the S parameter uncertainties of a single air measurement along the full frequency spectrum for 5 different 14 mm airlines of varying length. As the ratio between airline length and signal wavelength increases, the total measurement uncertainty in both dielectric constant and

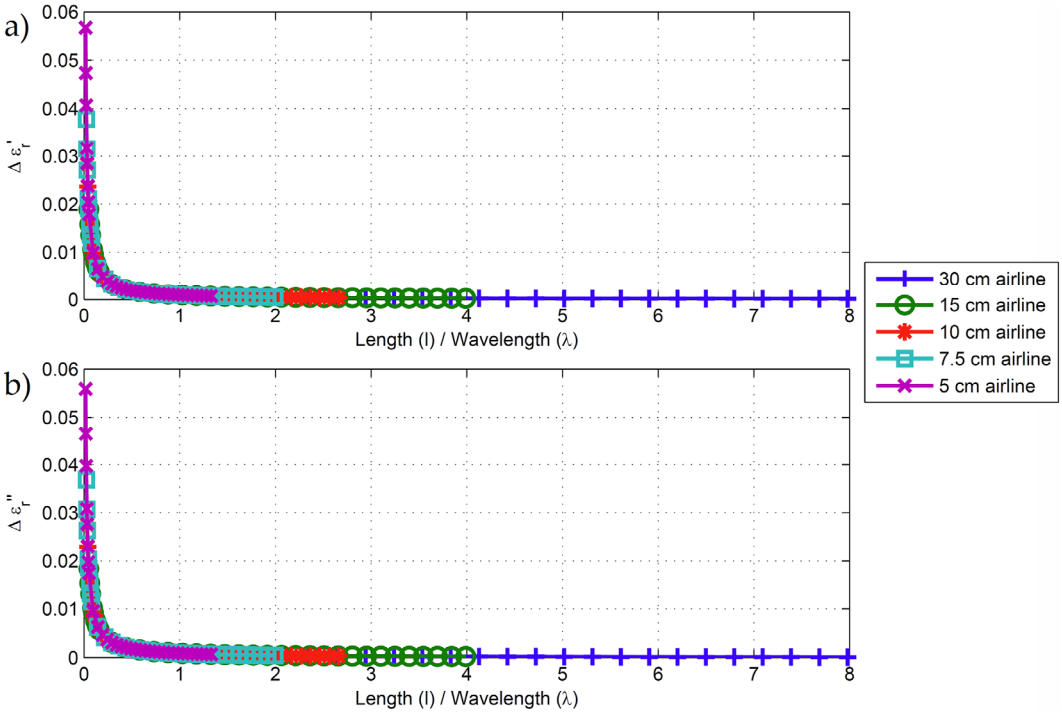

Figure 25 - Effect of Airline Length on S Parameter Influenced Permittivity Uncertainties

loss decreases accordingly. Consequently, this implies that S parameter uncertainties are directly proportional to frequency. Using this information it follows that a measurement performed at 4 GHz with a 14 mm-30 cm airline is just as accurate as a measurement performed at 8 GHz with a 14 mm-15 cm airline. It is therefore most advantageous to use lengthy airlines. However this is also impractical due to the amount of material needed. In the case of the 14 mm coaxial airlines, the 15 cm line was used as a balance between accuracy and sample requirements.

4.4.3 Air-gap Correction

It is known that for both the coaxial airline and rectangular waveguide, air-gaps and sample length requirements not being met are common sources of error. Air-gaps are created if the MUT does not fit the sample holder's cross-section and make close contact with the cavity walls [9] [8]. As with the parallel-plate capacitor, ideal experimental accuracies of 5% can be achieved, but air-gaps and fixture problems can decrease the

accuracy to 15% [15]. This is a 10% increase in experimental uncertainty. Larger air-gaps will inevitably increase the uncertainty. There are two types of air-gap correction; coaxial and waveguide gap correction. The respective correction is applied once the permittivity data has been obtained after data conversion.

For the coaxial gap correction, the three terms L_1, L_2, and L_3 must be calculated. They are obtained as follows [29]:

$$L_1 = \ln\frac{D_2}{D_1} + \ln\frac{D_4}{D_3}, \qquad L_2 = \ln\frac{D_3}{D_2}, \qquad L_3 = \ln\frac{D_4}{D_1}$$

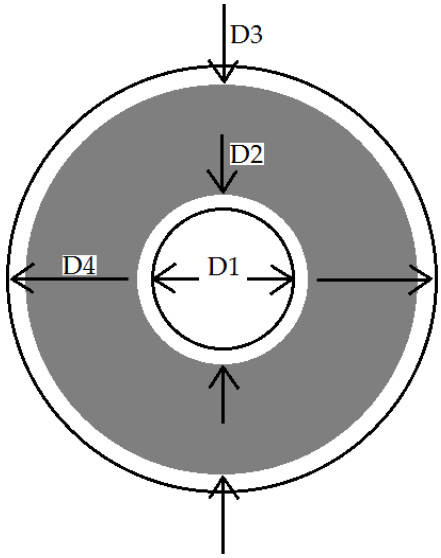

Figure 26 - Cross section of sample-filled airline (solid MUT in grey)

Here D_1 is the diameter of the inner conductor in the airline, D_2 is the inner diameter of the toroidal sample, D_3 is the outer diameter of the sample, and D_4 is the diameter of the coaxial airline itself (see Figure 26). Using these terms, an expression can be determined to obtain the real and imaginary corrected relative permittivity values ε'_{rc} and ε''_{rc} from the measured values ε'_{rm} and ε''_{rm} respectively. If need be, the corrected complex relative permeability μ_{rc} can also be obtained from the measured value μ_{rm} albeit with a

different set of expressions that are not presented here. The permittivity correction equations are as follows [29]:

$$\varepsilon'_{rc} = \varepsilon'_{rm} \frac{L_2}{L_3 - \varepsilon'_{rm} L_1}$$

$$\varepsilon''_{rc} = \left(\varepsilon'_{rc} \times \frac{\varepsilon''_{rm}}{\varepsilon'_{rm}} \right) \frac{L_3}{L_3 - L_1 \varepsilon'_{rm} \left(1 + \left[\frac{\varepsilon''_{rm}}{\varepsilon'_{rm}} \right]^2 \right)}$$

These equations were entered into Wolfram Mathematica and solved for the measured permittivity ε'_{rm} and ε''_{rm}. A MATLAB script was written using these new expressions for the correction equations in order to iterate over a series of corrected, or known, values of dielectric constant ε'_{rc} and loss ε''_{rc}. By simultaneously iterating over a range of specified air-gaps between the sample and inner and outer conductors, we can then calculate ε'_{rm} and ε''_{rm} since they are the only remaining unknowns. This program allows us to predict what we will be measuring, assuming that the equations are as accurate as presented, given a sample material whose properties are already known.

In Figure 27 and Figure 28 we have four plots each with the simulation results for a 7 mm and 14 mm airline respectively; a) the effects of inner conductor air-gaps on the measured dielectric constant, b) the effects of outer conductor air-gaps on the measured dielectric constant, c) the effects of inner conductor air-gaps on the measured dielectric loss, and d) the effects of outer conductor air-gaps on the measured dielectric loss.

From the simulation we immediately notice a difference between the effects of inner and outer air-gaps. In Figure 27a, we see that for a material with a dielectric constant of $\varepsilon'_r = 4$ and an inner air-gap of 0.2 mm, the measured dielectric constant has a 20% decrease in value. By contrast in Figure 27b, the same material with an air-gap of 0.2 mm

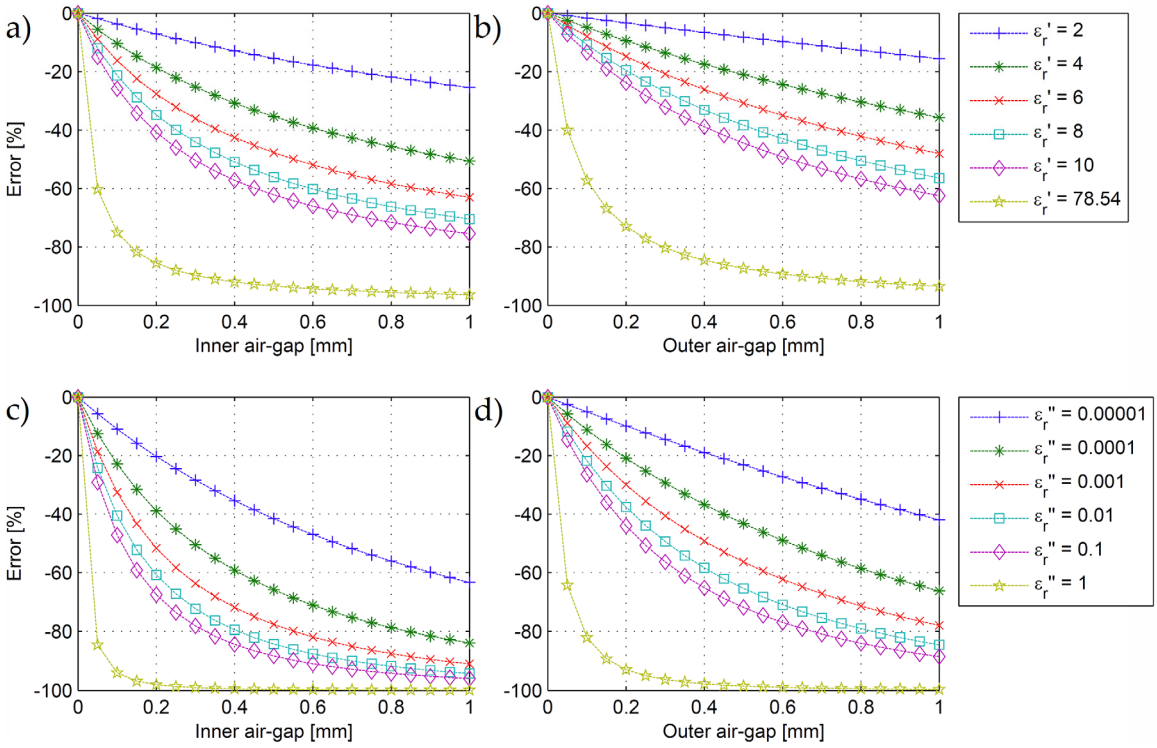

Figure 27 - Effects of MUT Inner and Outer Air-gaps on Measured Permittivity in a 7 mm Coaxial Airline

at the outer conductor instead causes a 10% decrease in measured dielectric constant. This is most likely due to the fact that the incident wave's electric and magnetic fields travelling in the +z direction originate at the inner conductor, and its intensity is most concentrated in and around this region. This effect is also apparent for the dielectric loss results in Figure 27c and Figure 27d.

While Figure 27 examined the effects of inner and outer air-gaps on the measured permittivity in a 7 mm coaxial airline, Figure 28 illustrates the same effects for a 14 mm airline. However, for the material with $\varepsilon_r' = 4$ and an inner air-gap of 0.2 mm, the

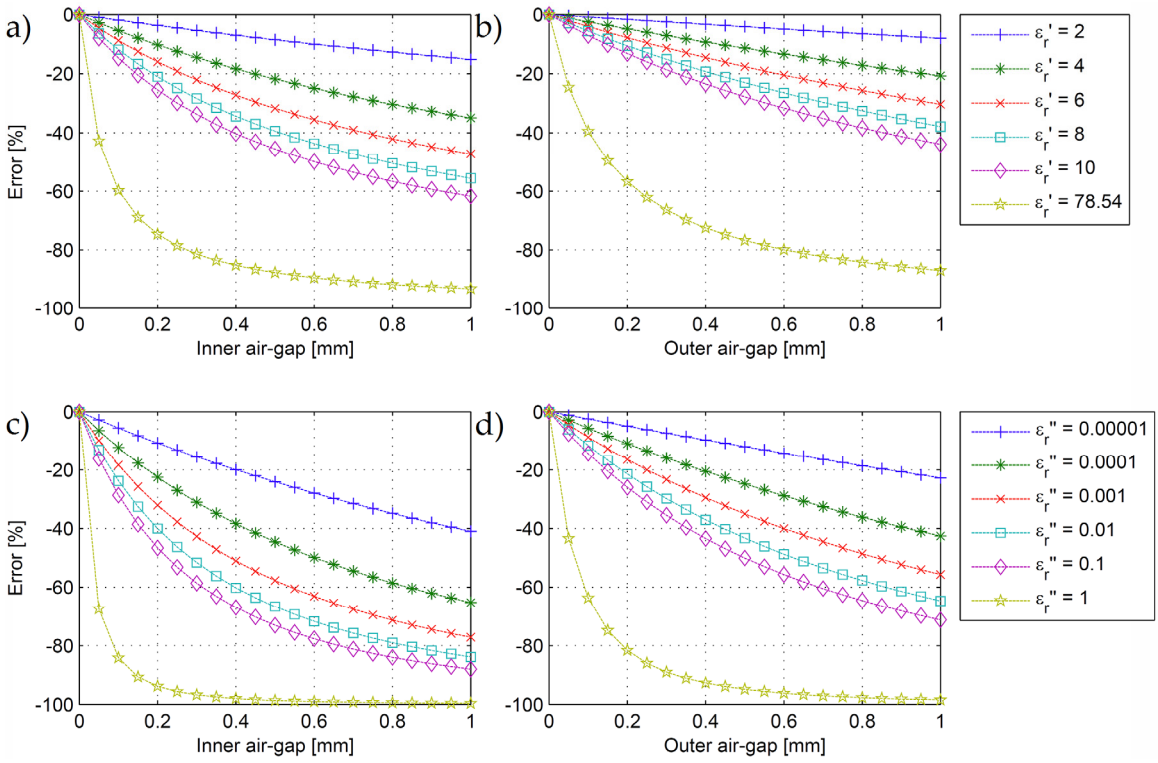

Figure 28 - Effects of MUT Inner and Outer Air-gaps on Measured Permittivity in a 14 mm Coaxial Airline

measured dielectric constant has a 10% decrease in value for a 14 mm airline whereas it was 20% for the 7 mm airline. This is due to the fact that the same air-gap represents a larger percentage of the total fillable volume of the 7 mm airline. Since air has a dielectric constant of $\varepsilon_r' \cong 1$ and loss of $\varepsilon_r'' \cong 0$, it follows that materials with large permittivity are most affected by air-gaps.

Although solid MUTs can be machined to close tolerances and, assuming perfect cylindricity, can be corrected using the air-gap equations, granular materials pose a more complex challenge. For solids, effective machining is the best solution in order to mitigate the effects of air-gaps. Powders with angular/sharp particles will most likely possess higher porosities around the edges of the sample holder regardless of packing. Although smaller particle sizes will reduce this effect, the difference in porosity within

the bulk of the material and at the edges of the airline could be problematic for medium to large grains. The only viable solution is to give preference to the 14 mm airline for permittivity measurements of granular materials.

4.5 Measurement Procedure Repeatability

In order to evaluate the repeatability of any measurement, the entire measurement procedure outlined in Section 3.3 was repeated 5 times for the 7 mm airline packed with silica sand. A granular material was chosen in order to represent a worst case scenario in repeatability, since each subsequent filling of the airline is slightly different from the last. This is in contrast to a solid sample that does not change. Each measurement was stored and the standard deviation for both the dielectric constant and loss was calculated at 15 evenly spread frequencies along the entire spectrum. All of this was then repeated with the 14 mm (15 cm length) airline to determine any discrepancies, should they exist.

In Figure 29, we have the five trial measurements of the dielectric constant, loss, and their respective standard deviations. The dielectric constant of the silica sand measurements has an unusually high standard deviation compared to that of its corresponding loss measurements, and is on average equal to 0.0023. It is thought that this is a result of minute amounts of granular loss between measurements having a larger effect on a 7 mm airline than it would on a 14 mm airline, due to the percent loss in mass. The standard deviation of the loss is considerably lower with an average of 0.0005. This is thought to be due to the fact that while some grains were gained/lost between measurements, the airline was filled nonetheless and the incident wave's phase change was not affected as much.

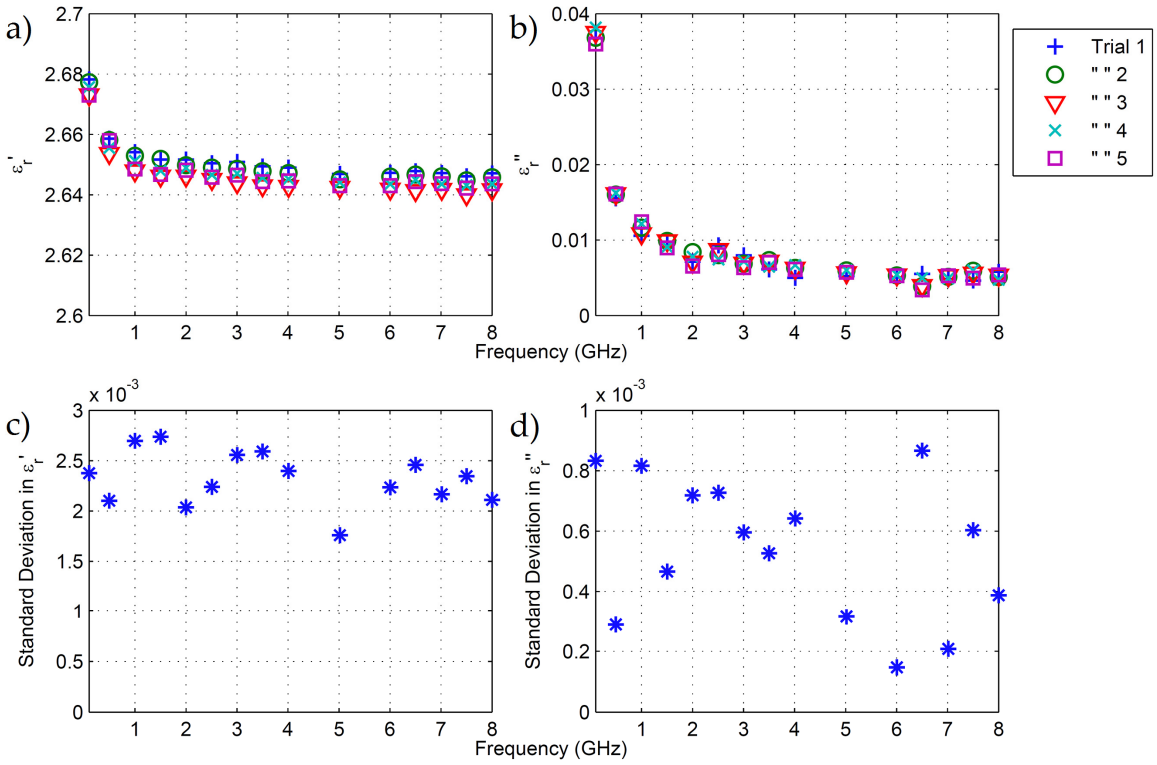

Figure 29 - Measurement Procedure Repeatability Using a 7 mm Airline

The results of the repeatability test for the 14 mm (15 cm length) airline proved to be much more reliable as seen in Figure 30. Whereas there was a large standard deviation in dielectric constant for the 7 mm line, we see here one with a mean value of 0.0007. The standard deviation in loss is quite similar to that of the 7 mm line and has a mean value of 0.0004. It should be noted that these values encompass not only the repeatability of the test system involving the shaking and packing of the granular materials into the airline, but also the repeatability of the connections made during the entire measurement procedure. These values represent absolute deviations which are much more crucial to quantify than percent deviations, especially for loss measurements.

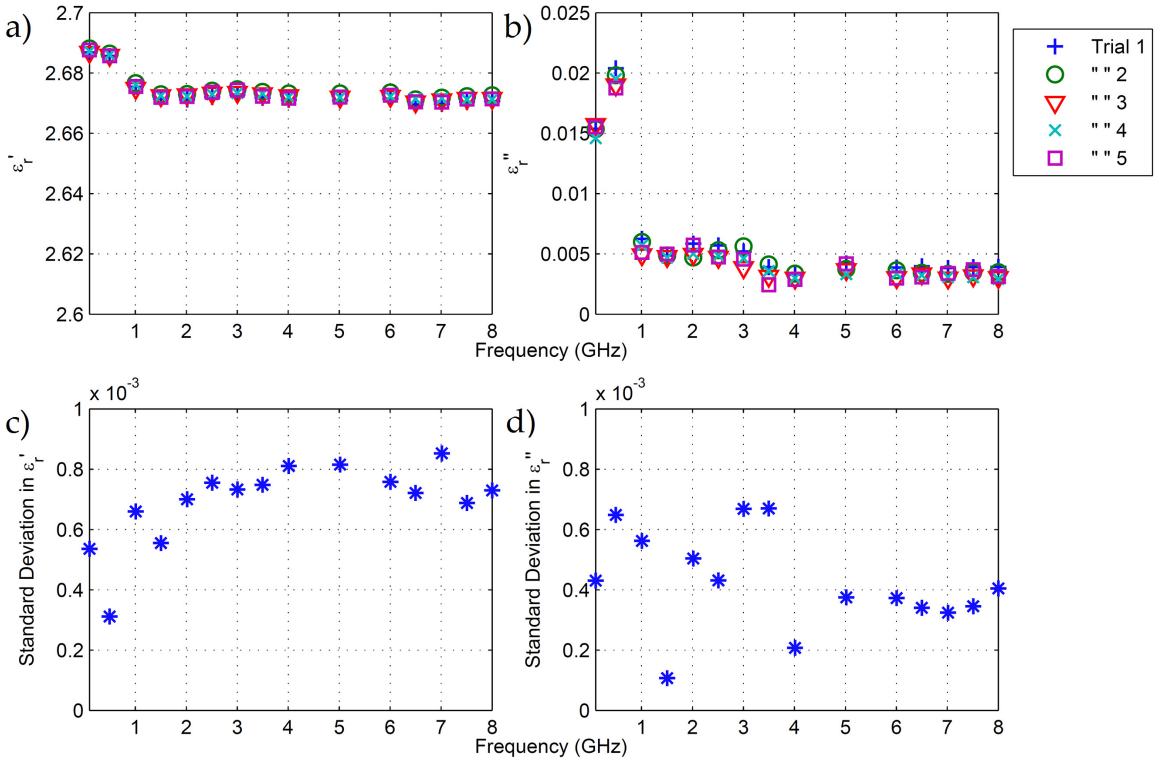

Figure 30 - Measurement Procedure Repeatability Using a 14 mm (15 cm length) Airline

4.6 Error Analysis

Based on the aforementioned error sources from Sections 4.2 to 4.4, the most problematic for all material types that cannot be mitigated are Network Analyzer dynamic accuracies, sample length uncertainties, and, exclusively applicable to solid samples, air-gap uncertainties. Partial derivative analysis can be used to calculate the absolute error in each air-gap corrected permittivity measurement and can be separated into its respective real and imaginary components as follows

$$\Delta\varepsilon'_{rc} = \left[\left(\frac{\partial\varepsilon'_{rc}}{\partial\varepsilon'_{rm}}\Delta\varepsilon'_{rm}\right)^2 + \left(\frac{\partial\varepsilon'_{rc}}{\partial D_1}\Delta D_1\right)^2 + \left(\frac{\partial\varepsilon'_{rc}}{\partial D_2}\Delta D_2\right)^2 + \left(\frac{\partial\varepsilon'_{rc}}{\partial D_3}\Delta D_3\right)^2 + \left(\frac{\partial\varepsilon'_{rc}}{\partial D_4}\Delta D_4\right)^2\right]^{1/2}$$

$$\Delta\varepsilon_{rc}''$$
$$= \left[\left(\frac{\partial\varepsilon_{rc}''}{\partial\varepsilon_{rm}'}\Delta\varepsilon_{rm}'\right)^2 + \left(\frac{\partial\varepsilon_{rc}''}{\partial\varepsilon_{rm}''}\Delta\varepsilon_{rm}''\right)^2 + \left(\frac{\partial\varepsilon_{rc}''}{\partial D_1}\Delta D_1\right)^2 + \left(\frac{\partial\varepsilon_{rc}''}{\partial D_2}\Delta D_2\right)^2 + \left(\frac{\partial\varepsilon_{rc}''}{\partial D_3}\Delta D_3\right)^2 + \left(\frac{\partial\varepsilon_{rc}''}{\partial D_4}\Delta D_4\right)^2\right]^{1/2}$$

where ΔD_1, ΔD_4, ΔD_2, and ΔD_3 are the uncertainties associated with the airline inner and outer diameters as well as the solid sample inner and outer diameters respectively. These expressions propagate all errors that lead up to performing air-gap corrections on solid samples using the correction technique presented by Youngs (1990). The uncertainties $\Delta\varepsilon_{rm}'$ and $\Delta\varepsilon_{rm}''$ strictly encompass all errors in the initial permittivity measurements prior to any air-gap corrections and are expressed as follows

$$\Delta\varepsilon_{rm}' = \left[\left(\Re\mathrm{e}\left(\frac{\partial\varepsilon_{rm}}{\partial|S11|}\right)\Delta|S11|\right)^2 + \left(\Re\mathrm{e}\left(\frac{\partial\varepsilon_{rm}}{\partial|S21|}\right)\Delta|S21|\right)^2 + \left(\Re\mathrm{e}\left(\frac{\partial\varepsilon_{rm}}{\partial\angle S11}\right)\Delta\angle S11\right)^2 + \left(\Re\mathrm{e}\left(\frac{\partial\varepsilon_{rm}}{\partial\angle S21}\right)\Delta\angle S21\right)^2 + \left(\Re\mathrm{e}\left(\frac{\partial\varepsilon_{rm}}{\partial l}\right)\Delta l\right)^2\right]^{1/2}$$

$$\Delta\varepsilon_{rm}'' = \left[\left(\Im\mathrm{m}\left(\frac{\partial\varepsilon_{rm}}{\partial|S11|}\right)\Delta|S11|\right)^2 + \left(\Im\mathrm{m}\left(\frac{\partial\varepsilon_{rm}}{\partial|S21|}\right)\Delta|S21|\right)^2 + \left(\Im\mathrm{m}\left(\frac{\partial\varepsilon_{rm}}{\partial\angle S11}\right)\Delta\angle S11\right)^2 + \left(\Im\mathrm{m}\left(\frac{\partial\varepsilon_{rm}}{\partial\angle S21}\right)\Delta\angle S21\right)^2 + \left(\Im\mathrm{m}\left(\frac{\partial\varepsilon_{rm}}{\partial l}\right)\Delta l\right)^2\right]^{1/2}$$

where $\Delta|S11|$, $\Delta|S21|$, $\Delta\angle S11$, and $\Delta\angle S21$ are the Network Analyzer dynamic accuracies associated with S11 and S21 magnitude and phase respectively, and Δl is the sample/airline length uncertainty. Again, $\Delta\varepsilon_{rm}'$ and $\Delta\varepsilon_{rm}''$ are all that is needed to be calculated when performing measurements with liquid and/or semi-solid (powdered) materials that do not require air-gap correction.

Another measurable quantity that is important to constrain and is applicable to semi-solids only is sample porosity. Although this doesn't directly affect the permittivity uncertainties using the coaxial airline technique, it is important to characterize nonetheless for comparative studies. Again, partial derivative analysis is used to calculate the absolute error in porosity and is represented by the following equation

$$\Delta\phi = \frac{\partial\phi}{\partial\rho_b}\underbrace{\sqrt{\left(\frac{\partial\rho_b}{\partial m}\Delta m\right)^2 + \left(\frac{\partial\rho_b}{\partial v}\overbrace{\sqrt{\left(\frac{\partial v}{\partial l}\Delta l\right)^2 + \left(\frac{\partial v}{\partial r_1}\Delta r_1\right)^2 + \left(\frac{\partial v}{\partial r_2}\Delta r_2\right)^2}}^{\Delta v}\right)^2}}_{\Delta\rho_b}$$

where $\Delta\rho_b$ is the uncertainty in bulk density of the sample filling the airline, Δm is the uncertainty in material mass, Δv is the uncertainty in airline volume, and Δr_1 and Δr_2 are the uncertainties associated with the airline inner and outer radii respectively. The following standard equations for porosity, density, and volume of a cylindrical shell were used

$$\phi = 1 - {}^{\rho_b}/_{\rho_p}$$

$$\rho_b = {}^{m}/_{v}$$

$$v = \pi r_2^2 l - \pi r_1^2 l = \pi(r_2^2 - r_1^2)l$$

where ρ_p is the powdered sample's theoretical particle density.

Dimensional analysis of the material under test and airlines was performed using various measurement methods. A digital caliper was used to measure the overall length of each airline centre conductor, which corresponds to its electrical length. Small hole gages paired with a micrometer were used to measure the outer conductor radius of the 7 mm airline as well as the inner diameter of all solid samples. A telescoping hole gage

and micrometer were used to measure the outer diameter of the 14 mm airline. Measurement of the outer diameter of all solid samples was done using only a micrometer. All powder material mass was measured using a digital scale.

	Δl [cm]	$\Delta D_1/\Delta r_1$ [cm]	ΔD_2 [cm]	ΔD_3 [cm]	$\Delta D_4/\Delta r_2$ [cm]	Δm [g]
Uncertainty	±0.001	±0.00025	±0.00025	±0.00025	±0.00025	±0.001
Method	Digital Caliper	Hole Gage Micrometer	Hole Gage Micrometer	Micrometer	Hole Gage Micrometer	Scale

Table 2 - Sample and Airline Dimensional Uncertainties with Corresponding Measurement Methods

It's important to establish that permittivity uncertainties due to length and air-gaps can be reduced considerably by using high accuracy measurement tools. Tools exist in the market today that can measure length accurately to ±1 μm. Uncertainty in material porosity can also be reduced by using high-end digital scales that have a readability of ±0.01 mg. Unfortunately, the biggest limiting factor is S parameter dynamic accuracy and is still problematic for low-loss measurements using the coaxial airline technique with even the most accurate VNA.

CHAPTER 5 Test Measurement Results

5.1 Empty Airline – Air

Alongside solid materials, the permittivities of gases are relatively easy to measure as they don't require any sort of packing as with granular materials. In Figure 31, the results from the Air (empty airline) measurements in this work are plotted. The measurements were performed with both the 7 mm and 14 mm-10 cm airlines and a frequency range of 0.22 – 8 GHz. This was done in order to obtain a better understanding of the limitations of the airlines themselves.

The dielectric properties of air at various frequencies, pressures, and temperatures have been studied extensively in the distant past for the purpose of radar range determination. Hector and Schultz (1936) studied dry air at 900 kHz and the results were found using a heterodyne beat frequency technique [44]. Hughes and Armstrong (1952) used the resonant cavity technique to measure the permittivity of dry air at 3 GHz [45]. Jordan et al. (1934) studied the effects of various frequencies, from 0 – 70 kHz, and pressures on the dielectric properties of air using a capacity-resistance bridge circuit [46]. Using the resonant cavity technique at a wavelength of 10 cm (3.036 GHz), Phillips (1950) studied the effects of moisture trapped in air [47]. The measurements performed for Air in this thesis are in good agreement with the results of the aforementioned published works.

As discussed by Hughes and Armstrong (1952), it is generally accepted that the dielectric constant of air is independent of frequency all the way up to 30 GHz and obtained a value of 1.000569 [45]. Although the results from this thesis may suggest that the dielectric constant decreases with increasing frequency, this was seen in Section 4.4.2 to be a consequence of airline length. In other words, as the

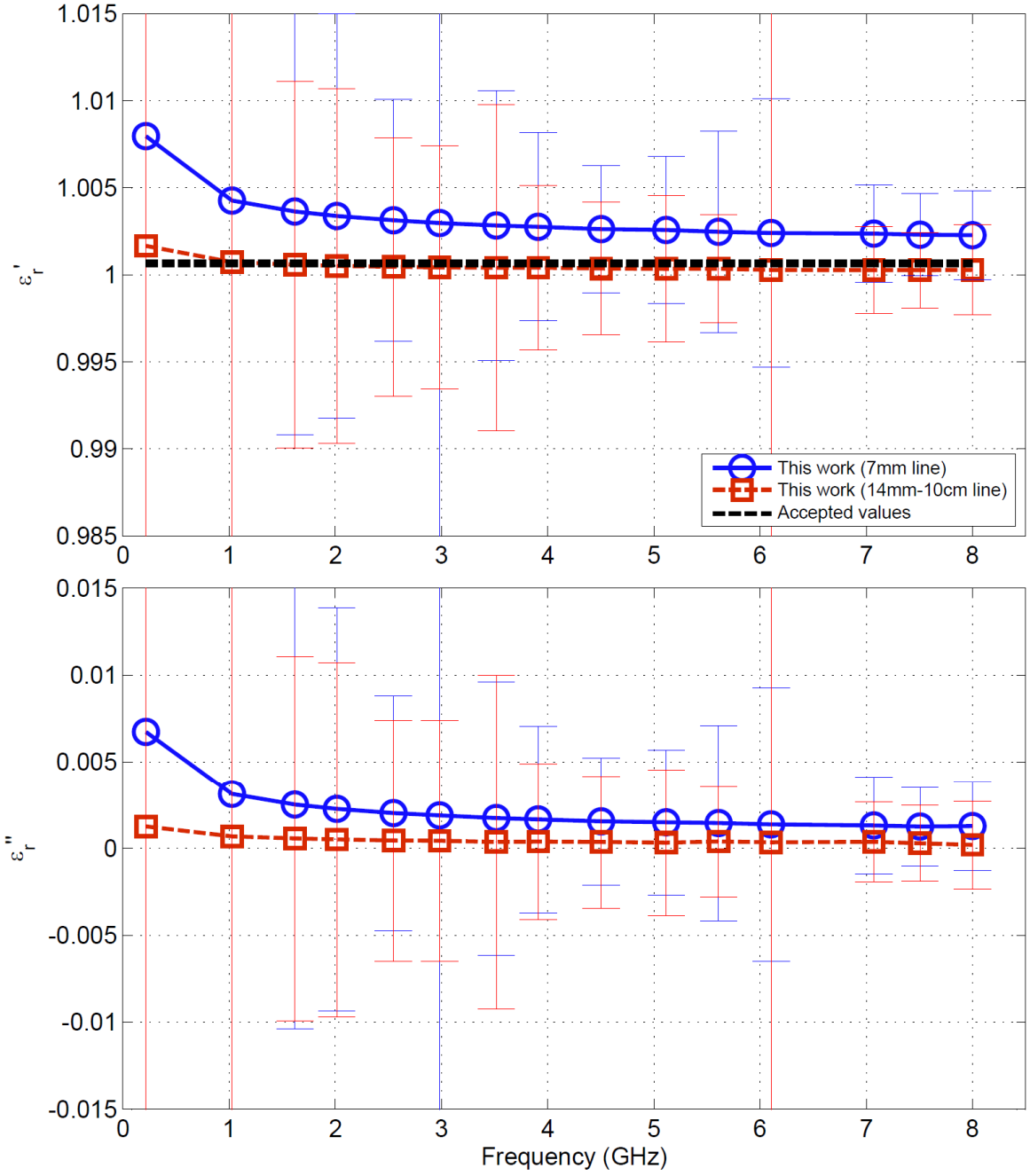

Figure 31 - Permittivity of Air

ratio between airline length and signal wavelength increases, the total measurement uncertainty in both dielectric constant and loss decreases accordingly. Hector and Schultz (1936) measured a value of 1.00058986, while Jordan et al. (1934) observed values

ranging between 1.000589 – 1.000593 from 0 – 70 kHz with no particular trend [44] [46]. These results are for dry air however. All measurements performed for the purpose of this thesis were performed in a laboratory with humidity of 45 ± 5% respectively. The results from Phillips (1950) showed the effects of water vapour on the dielectric constant of air, which was shown to vary linearly from a value of 1.0005548 to 1.000735 between 0 – 88.1% relative humidity. These results fall within the error bounds of the measurements performed here. Since air has a negligible dielectric loss and is considered as lossless as a vacuum, the relatively high losses measured here are a consequence of the losses of the coaxial lines themselves.

5.2 Granular MUTs

5.2.1 Silica Sand

In Figure 32, the results from the silica sand measurements in this work are plotted against that of other publications. The measurements were performed with both the 7 mm and 14 mm-10 cm airlines and a frequency range of 0.22 – 8 GHz. Matzler (1998) studied dry desert sand from Tunisia for the purpose of active and passive microwave remote sensing. The permittivity was measured in the frequency range of 0.245 – 6 GHz using the resonant cavity technique [48]. Njoku and Kong (1977) measured the permittivity of sand over a wide frequency range (only 0.3 – 8.5 GHz is presented here) with varying degrees of water content [49]. Stuchly (1970) measured the permittivity of four different granular solids, sand being one of them, at 9.4 GHz with varying degrees of water content using the very-long-sample method [50]. All measurements presented in Figure 32 were performed at room temperature and normal atmospheric conditions.

The porosities of the fully packed 7 mm and 14 mm lines are 0.3706 ± 0.0006 and 0.3537 ± 0.0004 respectively. Although it was initially expected that the porosities

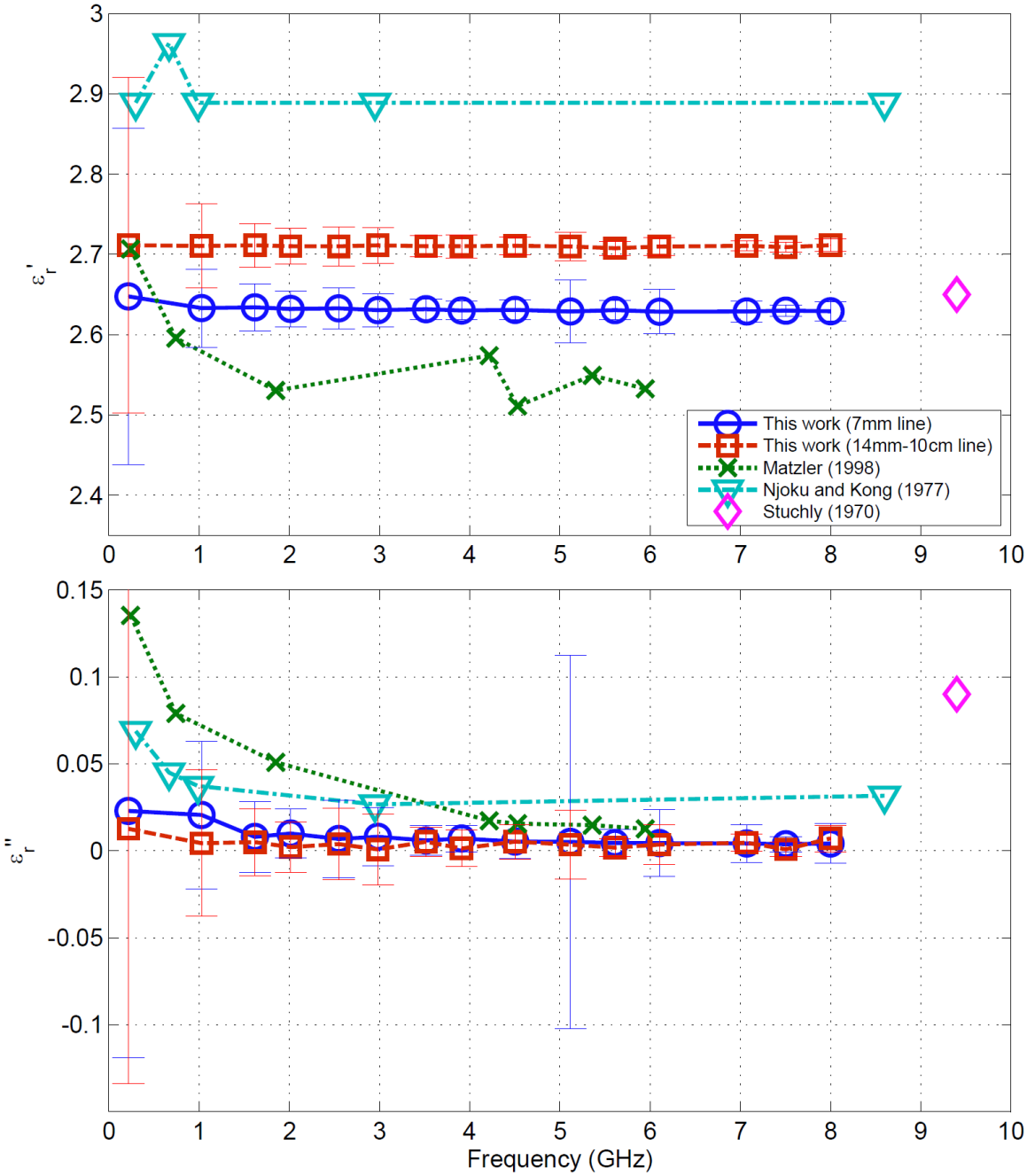

Figure 32 - Permittivity of Sand from this work compared to other published works

would be much closer considering the slightly more round shape of the grains as compared to the alumina studied in Section 5.2.2, the 14 mm line was better suited for packing due to its larger diameter. The corresponding bulk densities are 1.67 g/cm^3 and

1.71 g/cm^3 respectively, compared to $1.43 - 1.50\ g/cm^3$ by Matzler (1998) and 1.70 g/cm^3 by Stuchly (1970) [48] [50].

The measurements performed for Sand in this thesis are in good agreement with those of published works with comparable conditions. It is most probable that the slightly higher values in dielectric constant and loss in the results from Njoku and Kong (1977) are due to the residual moisture of 0.003 cm^3/cm^3 in the sand, as water possesses high permittivity [49]. The results from Matzler (1998) have a lower dielectric constant than the measurements in this work due to a higher porosity (more air) [48]. This also explains the increase in loss due to the interactions with air at the grain boundaries. The results from Stuchly (1970) closely resemble the dielectric constant measured in this thesis [50]. Given that the porosities are the same, this helps validate the results.

5.2.2 Alumina Grit

In Figure 33, it is seen that alumina grains of a particular size are better packed in the 14 mm airline than its 7 mm counterpart. It is important to remember that it is the bulk porosity within the airlines that is being measured. If we think about the porosity at the airline conductor edges (where the grains meet the inner and outer conductor) and that in between the edges as separate entities, grain shape and size will ultimately determine the degree of divergence of the two values. We can thus conclude that, provided as fully packed an airline as possible with the sieve shaker, the porosity at the airline conductor edges is greater in the 7 mm airline. This is especially true due to the angular shape of the grains. This effect is much more prominent in the larger grains but decreases as grain size decreases; ultimately when the boundaries shrink. Ideally, a tightly packed granular material with an infinitesimally small grain size will possess an edge porosity equal to the bulk porosity. It is for this reason that the greatest decrease in porosity for the 14 mm line (as compared to the 7 mm line) is seen with the 940 μm grains, and the smallest change in porosity is observed with the 102 μm grains.

Consequently due to this phenomenon, the dielectric constants increase between the 7 mm and 14 mm lines for each respective grain size (as expected) due to the decrease in bulk porosity.

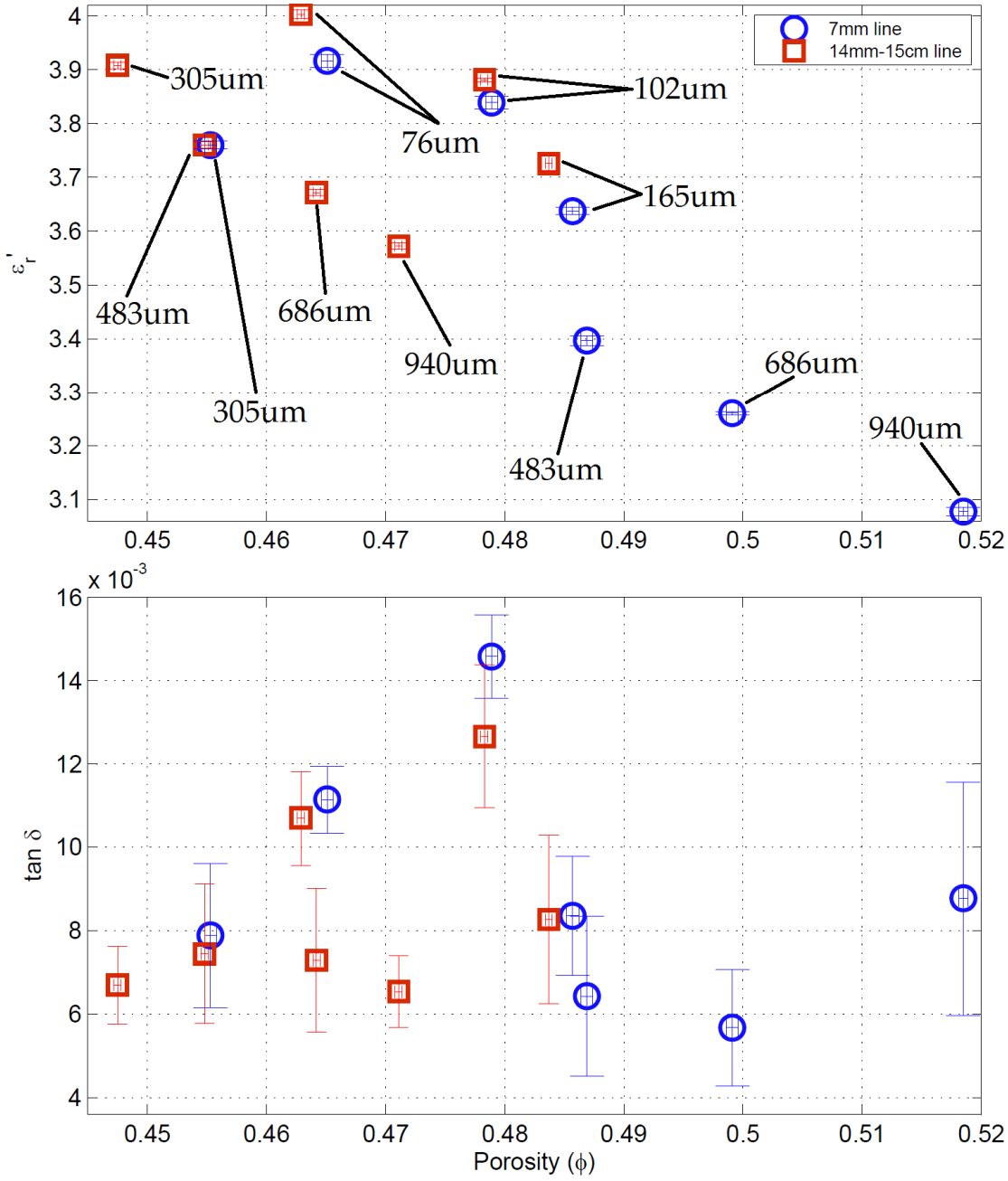

Figure 33 - Permittivity of Alumina measured with 7 mm-10 cm and 14 mm-15 cm airlines at 7.5 GHz

Interestingly however, the loss tangents all appear to be the same in both lines. In general the loss tangents measured with the 14 mm line are lower than that of the 7 mm line. This can be seen especially with the 102 µm and 165 µm pairings in the plot and also in the pair comprised of the 305 µm (7 mm) and 483 µm (14 mm) measurements, where each respective pair have similar porosities. Some errors are much greater than others due to the corresponding porosity causing a resonance to appear in and around 7.5 GHz, which is a persistent problem with this technique. It is hypothesized that no observable trend in loss tangent is present due to the fact that we are observing a small region of porosities.

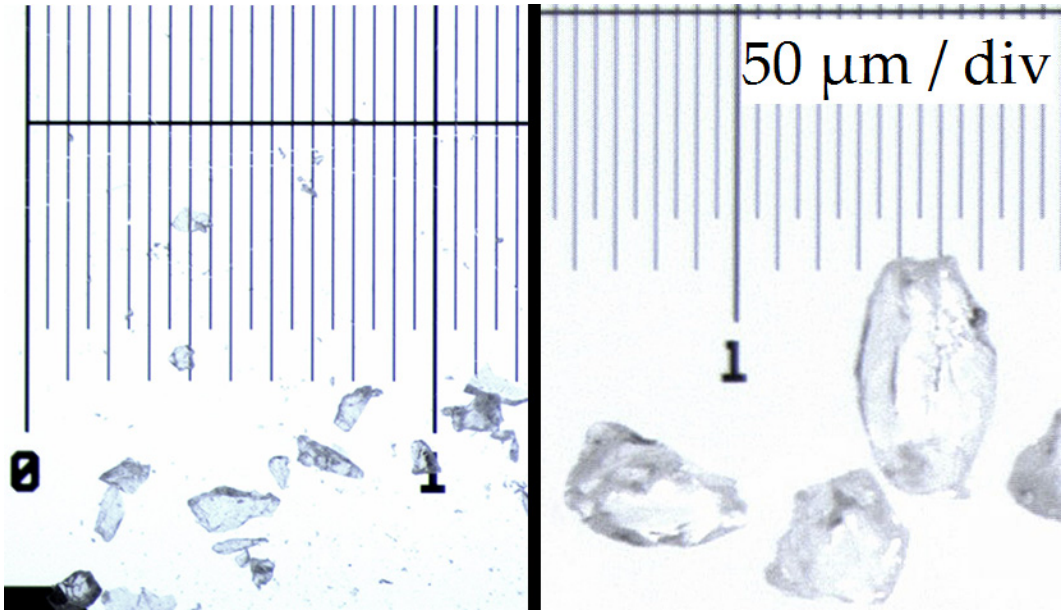

Figure 34 - 76 µm (left) and 305 µm (right) Alumina grain shapes

Another interesting pattern is the break in slope that is observable in both the 7 mm and 14 mm data. A difference in the grain manufacturing process between the 940 µm-305 µm and 165-76 µm batch of samples is theorized. This was ultimately observed to be due to the much sharper and triangular shape of the latter batch as observed with a microscope (see Figure 34).

For the 165-76 μm batch we see that the porosities between the 7 mm and 14 mm are almost the same. However, the 14 mm line dielectric constants are greater. This is most likely due to the fact that edge effects have less of an influence on the larger airline (for a given air-gap) than they do on the smaller line. Quite simply, a given air-gap comprises a smaller percentage of the total fillable area in the larger airline than in the smaller one. This phenomenon was discussed in greater detail in Section 4.4.3. In short, the increase in permittivity is related to edge effects on the centre and outer conductors, where smaller grains provide better contact with them by covering more surface area, thus reducing "air-gaps". In the end, it can be said that the 14 mm-15 cm line proves more reliable especially with the decrease in air-gap and length uncertainties.

In Figure 35, the results from all alumina measurements in this work are plotted against that of other publications. The most thorough work on alumina grit was done by Penn et al. (1997), where both the dielectric constant and loss tangent of sintered alumina and the effects of grain size and porosity were measured and studied at 9 GHz [25]. Krupka et al. (1998) measured the temperature effects on the permittivity of alumina at 7.53 GHz, though there is no mention of the grain size or porosity of the ceramic [22]. The result at room temperature is presented here. The loss tangent of alumina as a result of introducing different levels of dry and moist nitrogen gas was studied by Molla et al. (1999) at frequency ranges of 0.001 Hz – 100 MHz and 12 – 18 GHz; however, the result at 15 GHz before the introduction of nitrogen gas is used here. The alumina sample was compacted into a disc with a porosity of 42% with no specified grain size [51]. Vila et al. (1998) investigated the effects of impurities on several grades of alumina over a wide frequency range of 1 kHz to 15 GHz. However, the resulting porosities of all types of alumina studied were plotted solely against their respective dielectric constants measured at 15 GHz, and is presented here [52]. All published results used cylindrical resonant cavities to perform the measurements, and ceramic disks made by compacting commercially available alumina powder.

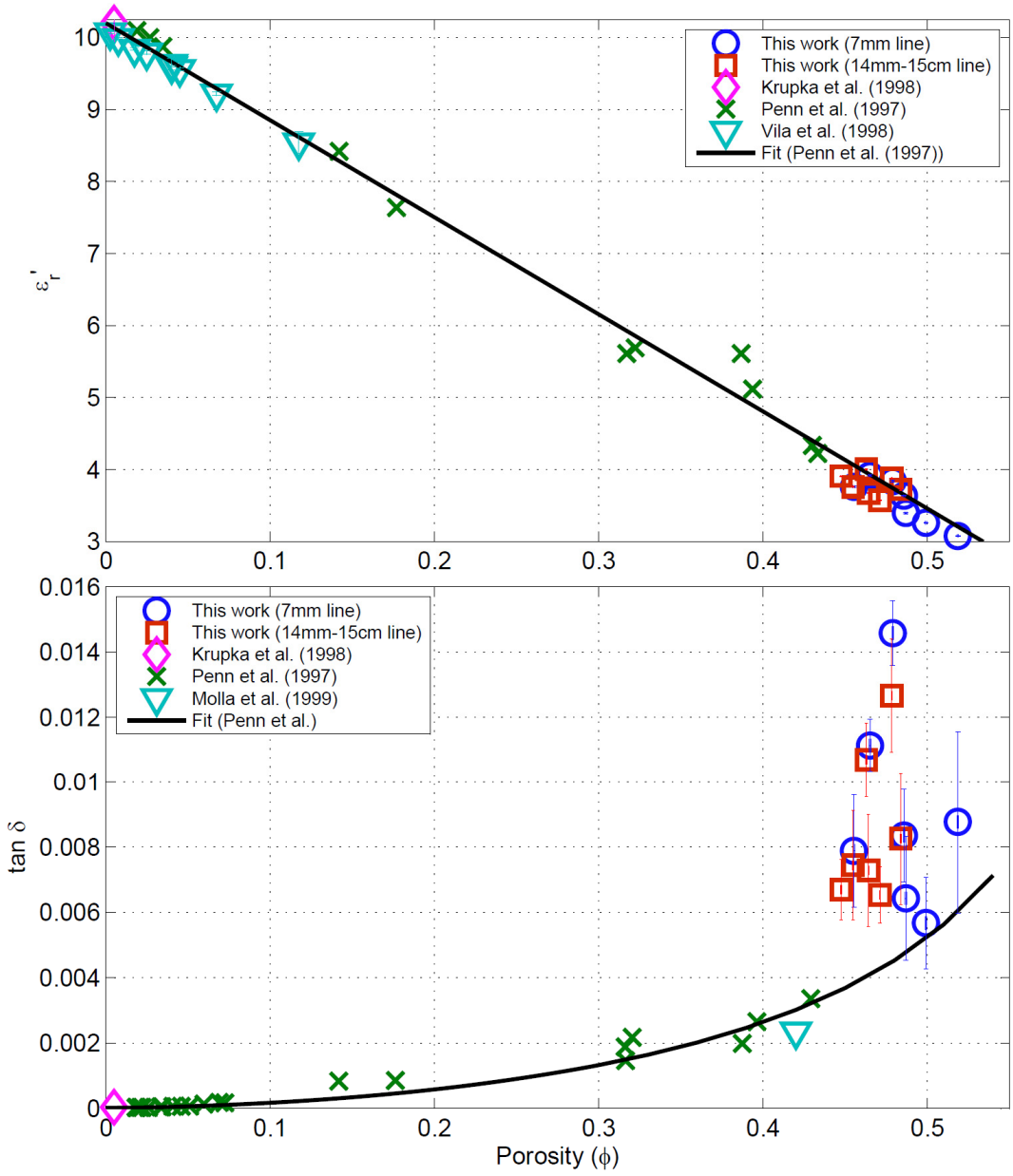

Figure 35 - Permittivity of Alumina from this work compared to other published works

Penn et al. (1997) provided a fit for the measured dielectric constant of alumina using a general relationship for spherical pores in a dielectric. Noting that the loss tangent increases alongside the porosity, they also developed an expression for the relationship between the loss tangent and porosity of a densely packed ceramic [25]. These fits are presented in the respective subplots of Figure 35 in order to place the measurements

from this thesis, as well as those of the other papers presented, in the appropriate context.

It is evident that Penn et al. (1997) covered a wider range of porosities than most studies. The fit provided for the dielectric constant illustrates this thesis' use of the broadband technique as equally capable and effective at providing excellent results as the more accurate resonant cavity technique. This can be seen by how accurate the results at the studied porosities are and how good of an extension they are to previous work done in the field with alumina, including that of Penn et al. (1997) and the others provided here. Assuming a hypothetical scenario where all the measurements are done in a vacuum, the dielectric constant of the pores would be equal to 1. This would indicate that as the porosity increases, the fit should theoretically approach 1 in both the x and y axis. It is for this reason that a more accurate fit would need to be developed in future studies in order to better reflect the permittivity of high porosity ceramics.

It has been observed that while the dielectric constant of a porous media decreases with increasing porosity, the loss tangent increases (Penn and Molla). This is especially evident from the results of Penn et al. (1997), which span a wide array of porosities. However, the loss tangent results of porous alumina from this thesis are not entirely conclusive. While it is true that the results possess a higher porosity and consequently a higher loss tangent, as expected, than those reported by other authors for lower porosities, it is difficult to observe a definitive trend due to the large measurement errors. It would also be beneficial to study a much wider range of porosities in a future study to determine if the expected trend is still present, regardless of the limitations of the coaxial technique.

5.3 Solid MUTs – Rexolite

In Figure 36, the results from all Rexolite measurements in this work are plotted against those of other publications. The measurements from this thesis presented in Figure 36

are based on Rexolite rods measured with 7 mm-10 cm and 14 mm-15 cm airlines over a frequency range of 0.16 – 8 GHz, and have been corrected for air-gaps. Garcia-Ruiz et al.

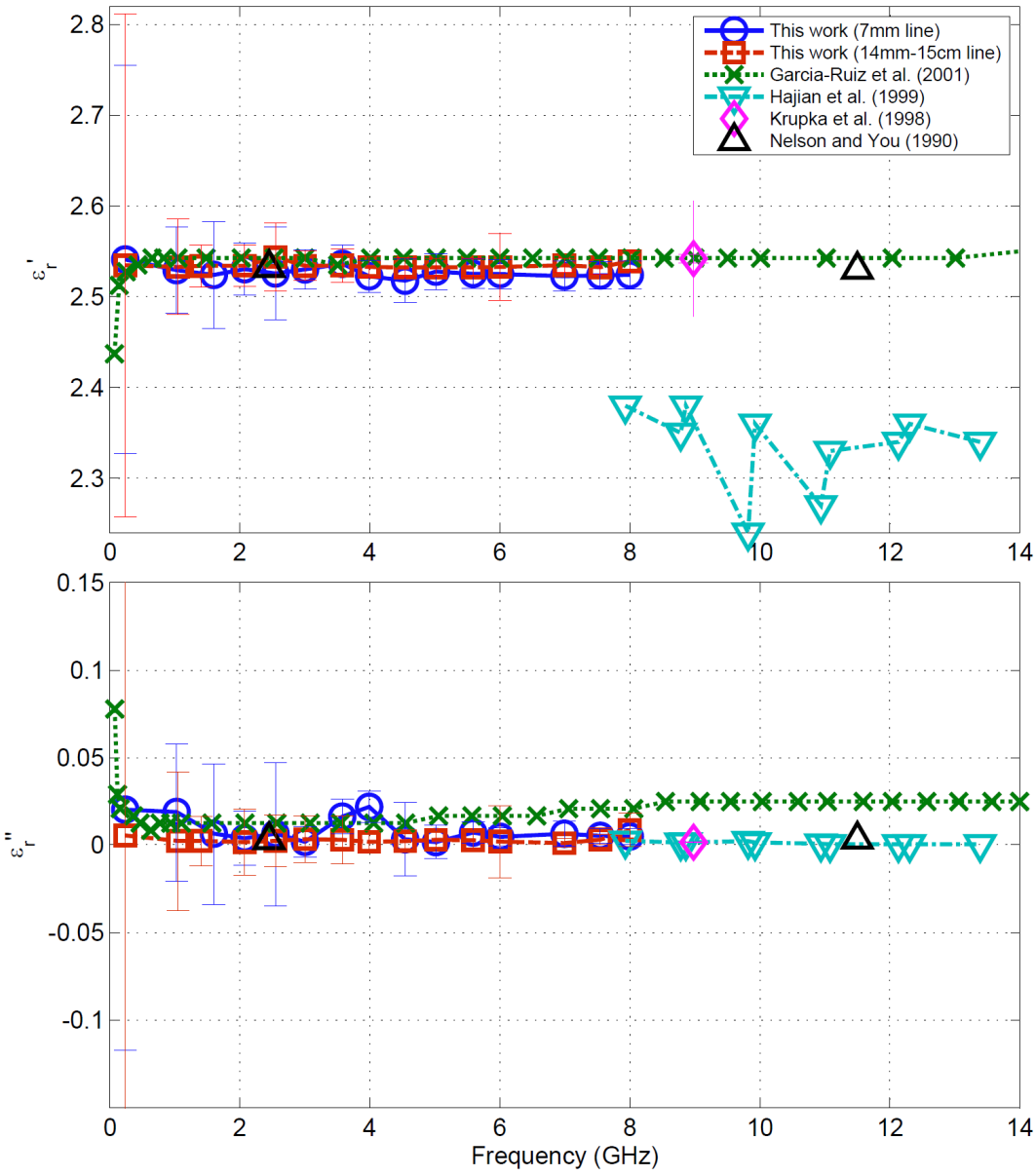

Figure 36 - Permittivity of Rexolite from this work compared to other published works

(2001) did a survey of the permittivity of Rexolite using both the coaxial probe and free-space technique. However only the results of the former have been plotted [53]. A

waveguide resonator was used by Hajian et al. (1999) in order to characterize the permittivity of Rexolite from 7.93 – 13.3899 GHz [54]. Krupka et al. (1998) measured the temperature effects on the permittivity of Rexolite at 8.98 GHz using a resonant cavity [22]. The result at room temperature is presented here. Nelson and You (1990) investigated both pulverized and solid samples, as well as the relationship between the two via extrapolation, at frequencies of 2.45 GHz, 11.5 GHz, and 22.0 GHz using a waveguide [55]. The results presented here are solely from the measurements performed on the solid rods. Although more work has been done at much higher frequencies, they were omitted due to any possible influences frequency holds on the resulting measurement.

It is not known why the results for the dielectric constant of Rexolite from Hajian et al. (1999) using the waveguide resonator seem to differ from all other work, although they claim that they are in good agreement with given values in literature. The results from this thesis for the dielectric constant using both airlines are in great agreement with the results in the literature provided. As expected, the 14 mm airline provided slightly more stable results (less deviation from the average) than the 7 mm airline. Furthermore, there was less dielectric loss in the 14 mm results, as seen with equally porous granular material such as silica in Section 5.2.1. While confidence can be placed in the dielectric constant results, especially as the amount of uncertainty decreases with increasing frequency, the dielectric loss results are quite uncertain. Ultimately, all dielectric loss measurements performed using the broadband coaxial airline technique seem to be limited by the losses of the airline itself.

5.4 Case Study

As a case study, a preliminary measurement of the permittivity of olivine, which is a known lunar simulant, was performed. The majority of meteorites that fall to Earth, called Chondrites, are believed to come from a parent S-type asteroid and are rich in

olivine and pyroxene; however, they have different spectral properties which provides the lack of a proper link. It is believed that space weathering and processes such as the bombardment of micrometeorites on the upper layers of asteroids alter the surface spectral properties [56]. It is for this reason that there is interest in determining how space weathering processes affect the dielectric properties of space materials such as olivine, in particular the losses.

Three different olivine samples were provided courtesy of researcher Jeffrey J. Gillis-Davis from the University of Hawai`i at Manoa; San Carlos (Arizona, USA) olivine, Reade Advanced Materials fresh olivine, and Reade olivine with laser simulated space weathering. The experimental setup used by Gillis-Davis is similar to that of Yamada et al. (1999), but loose olivine powder with grain sizes similar to planetary surfaces (<75 μm) was used rather than pressed pellets of material. Space weathering was achieved using the facilities at the University of Hawai`i at Manoa with the laboratory equipment consisting of a Nd:YAG (1064 nm) pulsed (20 Hz) laser, and a turbo and roughing pump combination to achieve a vacuum of $2 - 3 \times 10^{-6}$ torr. The pulse duration of the laser is 5 - 7 ns, which is comparable to the timescale of micrometeorite impacts. The weathered Reade olivine sample was irradiated with 80 mJ per pulse for 10 minutes.

Due to the simulated space weathering being a lengthy process, small amounts of the material were produced. For this reason the 7 mm-10 cm airline was used. Although unfavorable compared to the larger and lengthier airlines, it requires the least amount of material to be filled. The results of the measurements can be found below.

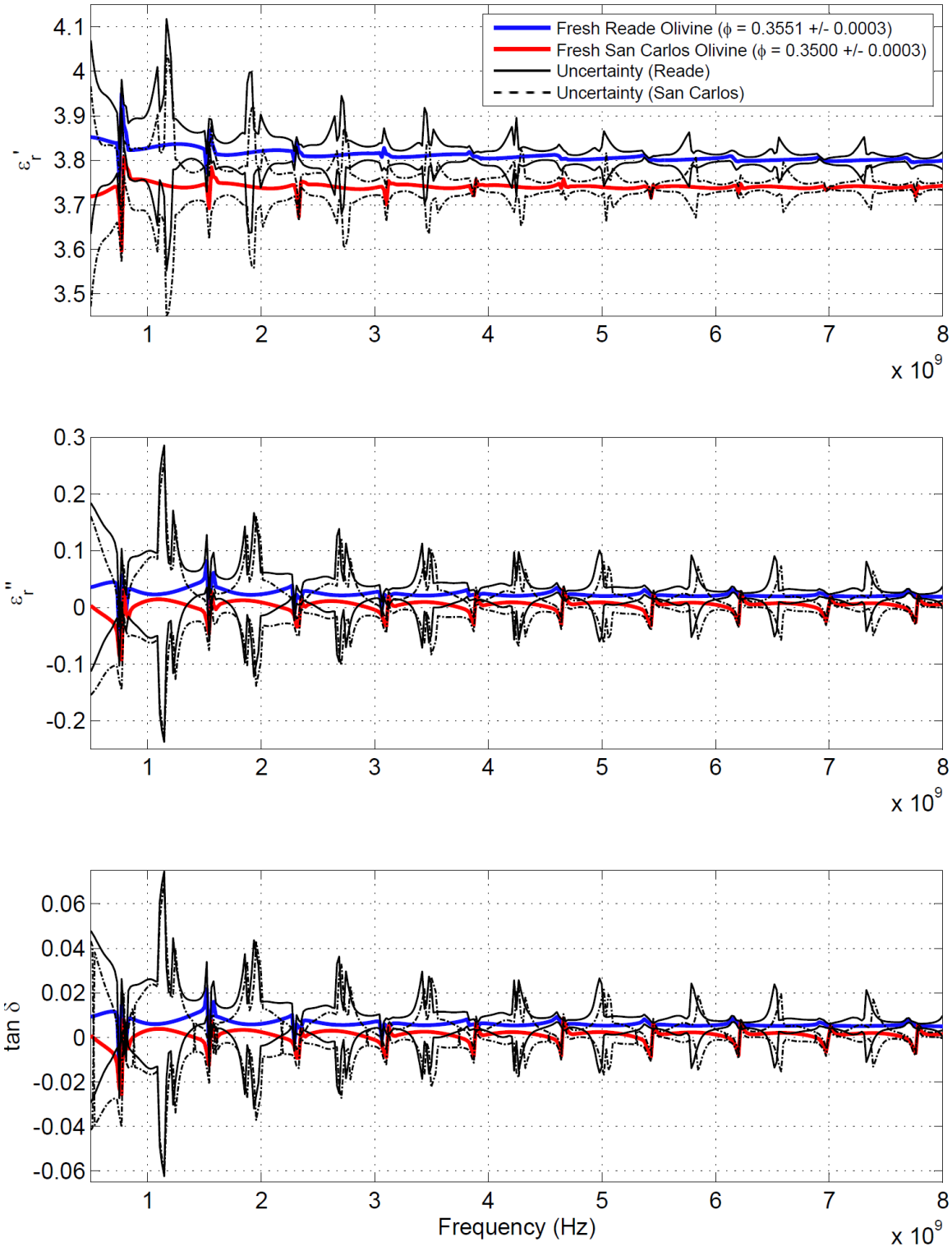

Figure 37 - Permittivity of Fresh Reade and San Carlos Olivine v. Frequency

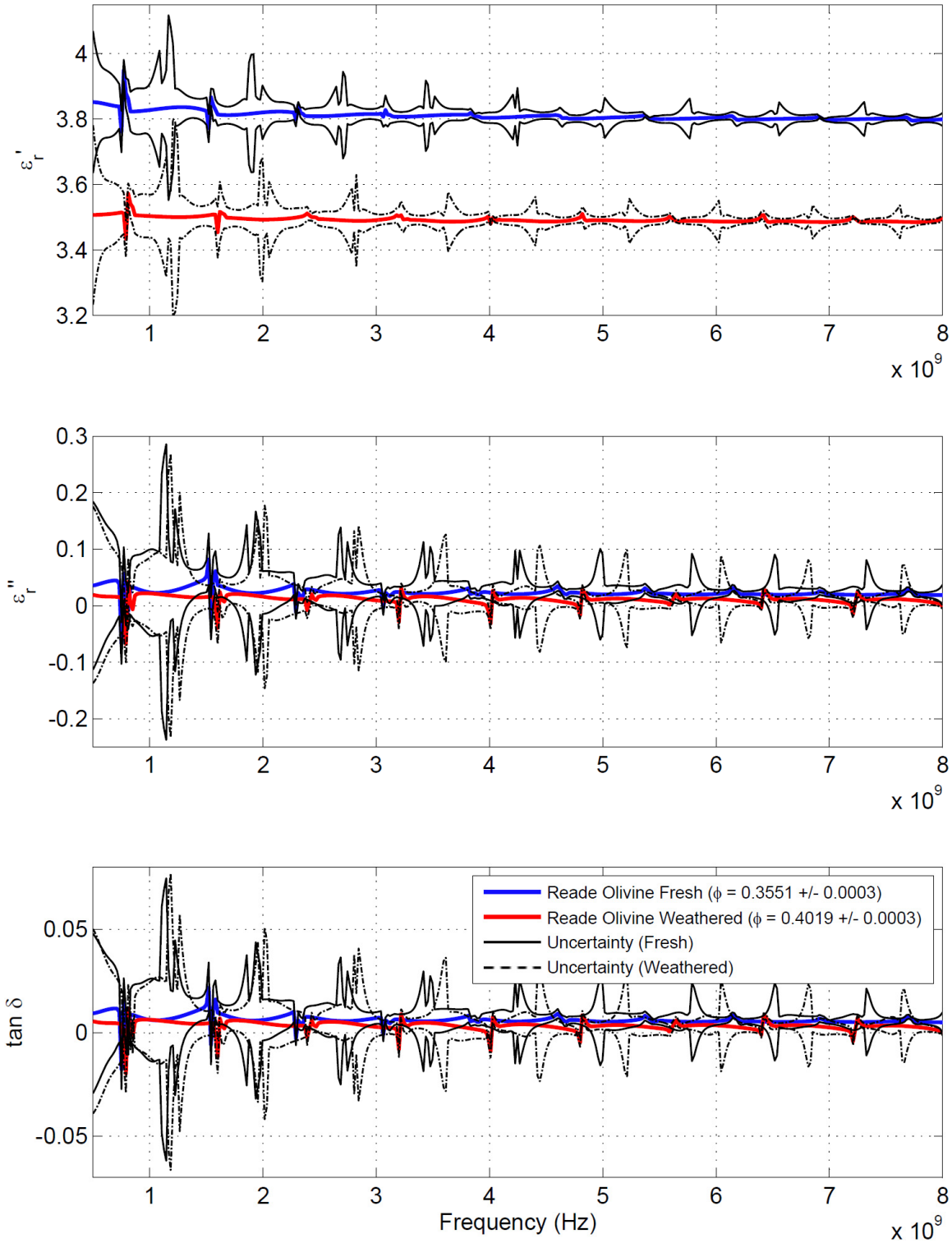

Figure 38 - Permittivity of Fresh and Weathered Reade Olivine v. Frequency

Although the fresh Reade and San Carlos olivine samples could be packed very well and with similar porosities of 0.3551 ± 0.0003 and 0.3500 ± 0.0003 respectively, the weathered Reade sample was much more difficult to pack with a final porosity of 0.4019 ± 0.0003. It was initially believed that the weathering process would not affect the grain size, however it was later considered that the weathered sample possesses more static forces than the unweathered samples, since the weathering process increases the amount of nanophase iron. Using backscattered electron images, Yamada et al. (1999) showed that even irradiation levels well below those used to render the sample used in this thesis were responsible for fragmentary particle loss between larger grains. Furthermore, micron-sized holes were formed due to surface evaporation at 30 mJ. Additional exposure increased the size of the holes on the grain surfaces and caused the grain edges to lose sharpness [56]. It is believed that this phenomenon is responsible for the decrease in bulk density.

In Figure 37, the measured dielectric constant, loss, and calculated loss tangent of the Reade and San Carlos olivines are shown. At first glance it is seen that the Reade olivine has a higher dielectric constant and loss than the San Carlos sample. As the amount of iron differs between different types of olivine, the result presented is most likely indicative of lower iron content in the San Carlos sample. Although the uncertainties for the losses are great, this is a plausible scenario given the greater accuracy in dielectric constant.

Comparing the fresh and weathered Reade samples in Figure 38, it is somewhat more difficult to draw an absolute conclusion. Again, due to the irradiation process and its effect on the weathered grains, it was not possible to pack both samples with the same porosity. While the fresh Reade olivine could have been packed more lightly to counteract this effect, there is no control over local porosities within the material itself and how much they differ from the overall bulk porosity. In order to discover any possible trends, the permittivities of the two samples were plotted against each other.

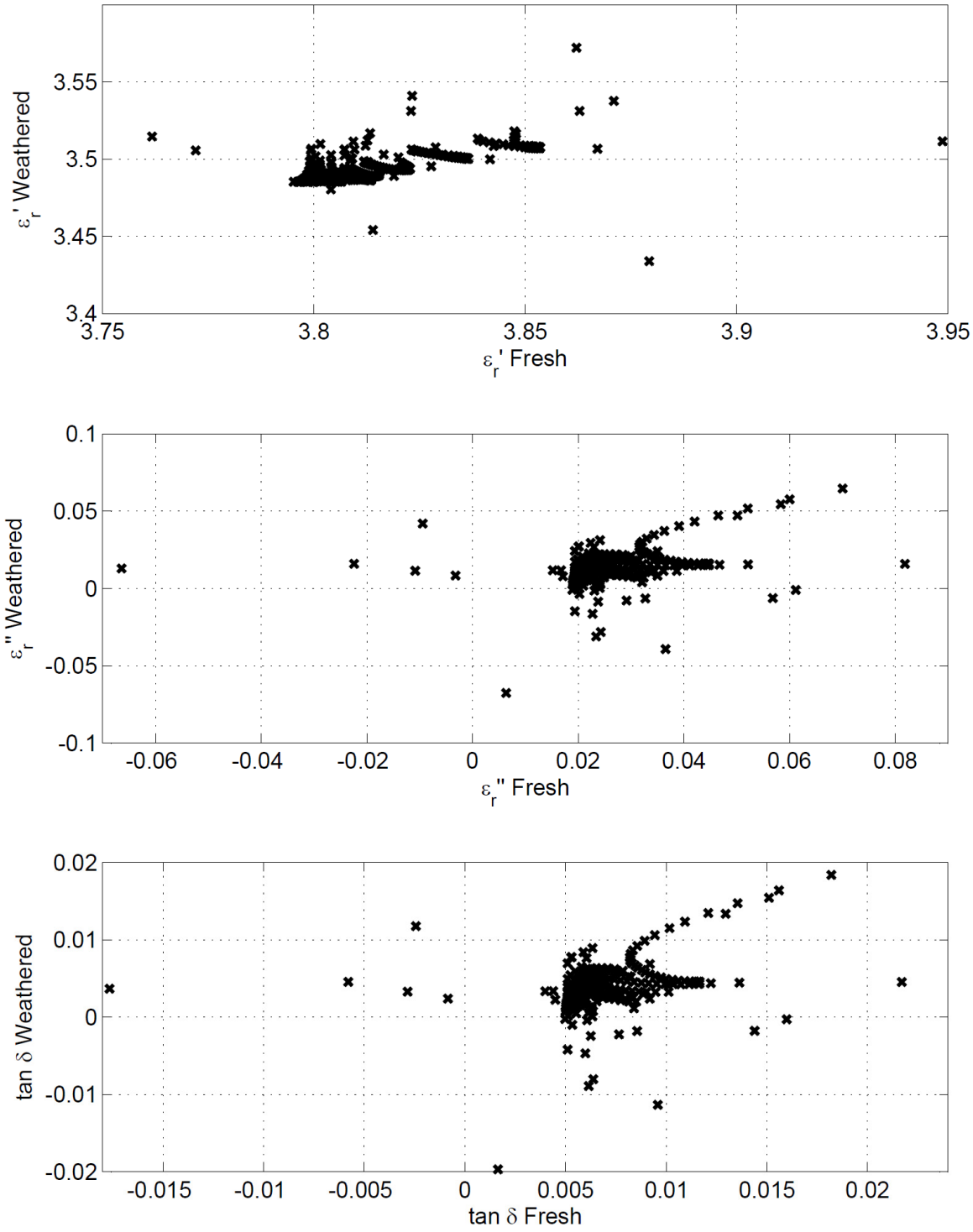

Figure 39 - Permittivity of Weathered Reade Olivine v. Fresh Reade Olivine

Since the weathering process increases the amount of nanophase iron, it was expected that the weathered sample would yield a higher loss. However from the results we see that the permittivity of the weathered sample is lower than that of the fresh sample. With different porosities it is difficult to understand whether this is a consequence of more air being present, although Penn et al. (1997) suggested a proportional increase in loss tangent with porosity for alumina grains [25]. In Figure 39, the scattered points deviating from the main cluster are due to the resonances present in the measurements. Unfortunately no observable trend is present that would indicate the presence of nanophase iron or other changes brought on during the weathering process. Given the magnitude of the uncertainties involved for the losses as well as the difference in porosity, the results are inconclusive.

CHAPTER 6 Conclusion

6.1 Conclusion

Radar is a valuable tool for the investigation of planetary surfaces and asteroids. It permits constraints on the physical and chemical properties of the regolith. Although variations in radar albedo are a good indicator of changes in near-surface regolith structure, density, and metal content, additional work is required to constrain the radar characteristics of geological materials. The aim of this thesis has thus been two-fold: to develop a procedure to perform accurate and repeatable broadband permittivity measurements of geological materials and to present a detailed error analysis comprising all characterizable error sources.

Chapter 3 provided an overview of the newly developed measurement procedure. The most challenging aspect of the coaxial airline technique is the process of filling it with granular samples. A novel approach was taken to handle this issue that has yet to be encountered in other works. In order to address this issue, a semi-solid sample preparation fixture was designed, machined, and retro-fitted onto the Gilson Performer III Sieve Shaker. Using the vibrating base of the shaker, this newly developed fixture was successfully able to facilitate the filling of the airline with granular samples and to densely and uniformly pack said material. The fixture allowed a brass rod to align and secure the centre position of the airline inner conductor, which is also a new approach developed for the purpose of this study.

The detailed error analysis presented in Chapter 4 provided an overview of the common error sources encountered, as well as appropriate mitigation, while performing broadband permittivity measurements: VNA errors (Systematic, Random, Drift/Stability), calibration errors, sample related errors, and measurement procedure repeatability. The most problematic for all material types that cannot be mitigated are Network Analyzer dynamic accuracies, sample length uncertainties, and air-gap

uncertainties which are unique to solid samples. Partial derivative analysis was used to develop an expression to calculate the absolute error, comprising all characterizable error sources, of each permittivity measurement.

It was shown that longer airlines led to a reduction in S Parameter influenced permittivity uncertainties for a given frequency. Consequently this implies that as measurement frequency increases, S parameter uncertainties decrease. A 14 mm-15 cm airline is the ideal choice as it provides a balance between the amount of material needed to fill the airline and the influence of S Parameter uncertainties. Air-gaps between the sample and airline conductors caused a deviation from the real permittivity value of the material. Inner air-gaps presented a greater problem. A material with an actual dielectric constant of $\varepsilon_r' = 4$ and an inner air-gap of 0.2 mm led to a 20% decrease in the measured value with a 7 mm airline. By contrast, the same material with an air-gap of 0.2 mm at the outer conductor instead causes a 10% decrease in measured dielectric constant. Materials with greater permittivity experience larger errors. An immediate solution is to use airlines with larger diameters in order to minimize these errors, such as the 14 mm airline. Also crucial is measurement drift over time, which is shown to cause a drift in percent difference up to 15% for loss measurements after 60 minutes. It is thus important to perform measurements immediately following calibration.

Connector repeatability has an average standard deviation equal to 0.0001 for the dielectric constant and 0.00005 for the loss. Measurement procedure repeatability using the 7 mm airline has an average standard deviation equal to 0.0023 for the dielectric constant and 0.0005 for the loss, and 0.0007 and 0.0004 respectively for the 14 mm airline. Based on the results presented in Chapter 5, the measurements are much more repeatable than they are accurate. The uncertainty in dielectric constant and loss varied from ± 0.1 to ± 0.3 at very low frequencies where the wavelength greatly exceeded the airline length (MHz), and ± 0.01 to ± 0.03 at high frequencies (GHz). In rare instances, or

when measuring an empty airline, the uncertainties would dip down to ± 0.001 although this is seen as an exception to the rule rather than the rule itself. These values of uncertainty are acceptable for dielectric constant measurements. However they are unacceptable for dielectric loss measurements, especially for radar studies where most regolith have low losses with values $< 10^{-4}$. Therefore, this thesis confirms the commonly held belief regarding poor accuracy in dielectric loss measurements with the transmission line technique and the value ± 0.01 presented by Baker-Jarvis et al. (1995) [8].

6.2 Future Work

Although the results presented here have demonstrated the effectiveness of the newly developed measurement procedure as well as confirmed the commonly held notion of low accuracy, it could be further developed. Future work to develop a method to further compact and press samples within the airline, using a more powerful shaker platform or alternative method, can be used to attain lower porosities. The ability to pack the airline more densely will allow a more accurate comparison to the work of Penn et al. (1997) for the permittivity of alumina, especially for the loss tangent measurements that don't follow the trend from the aforementioned study. An in depth study similar to the approach used by Penn et al. (1997) would be of particular interest for common planetary analogue materials, as a means to develop a complete database of permittivities for future missions.

As S Parameter uncertainties are the biggest contributors to the total uncertainty of the broadband technique permittivity measurements, additional work to either circumvent or remove these uncertainties altogether would be highly beneficial. New approaches to the calibration technique would also help eliminate the inherent losses of the coaxial airlines that were not accounted for in this study. Furthermore, investigating resonant cavity techniques would be the next logical step in order to accurately measure the

dielectric loss, and thus the loss tangent, of analogue materials at specific frequencies of interest for future radar studies.

BIBLIOGRAPHY

[1] J. H. Grosvenor, "NIST Measurement Service for Electromagnetic Characterization of Materials," 1993.

[2] R. P. Feynman, R. B. Leighton and M. Sands, The Feynman Lectures on Physics: The New Millenium Edition, 6th ed., vol. 2: Mainly Electromagnetism and Matter, Basic Books, 2011.

[3] R. Carley and E. Heggy, "Characterization of the Density Dependent Dielectric Properties of Mars-like Soils: Implications for Mars Radar Studies," in *37th Annual Lunar and Planetary Science Conference*, 2006.

[4] J. L. Davis and A. P. Annan, "Ground-Penetrating Radar for High Resolution Mapping of Soil and Rock Stratigraphy," *Geophysical Prospecting,* vol. 37, no. 5, pp. 531-551, 1989.

[5] M. J. Campbell and J. Ulrichs, "Electrical Properties of Rocks and Their Significance for Lunar Radar Observations," *J. Geophys. Res.,* vol. 74, no. 25, pp. 5867-5881, 1969.

[6] E. Heggy, P. Paillou, G. Ruffie, J. Malezieux, F. Costard and G. Grandjean, "On Water Detection in the Martian Subsurface Using Sounding Radar," *Icarus,* vol. 154, no. 2, pp. 244-257, 2001.

[7] L. C. Shen and J. A. Kong, Applied Electromagnetism, 1st ed., R. Kingman and M. Gallantz, Eds., PWS Publishers, 1983.

[8] J. Baker-Jarvis, C. Jones, B. Riddle, M. Janezic, R. Geyer, J. Grosvenor and C. Weil, "Dielectric and magnetic measurements: A survey of nondestructive, quasi-nondestructive, and process-control techniques," *Research in Nondestructive Evaluation,* vol. 7, pp. 117-136, 1995.

[9] Agilent, "Agilent Basics of Measuring the Dielectric Properties of Materials," *Application Note,* Vols. 5989-2589EN, June 2006.

[10] H. E. Bussey, "Dielectric Measurements in a Shielded Open Circuit Coaxial Line,"

Instrumentation and Measurement, IEEE Transactions on, vol. 29, no. 2, pp. 120-124, june 1980.

[11] D. Fleisch, A Student's guide to Maxwell's equations, Cambridge University Press, 2008.

[12] D. Halliday, R. Resnick and K. S. Krane, Physics, 5th ed., vol. 2, John Wiley & Songs, Inc., 2002.

[13] M. A. Plonus, Applied Electromagnetics, 1st ed., P. D. Nalle and M. Gardiner, Eds., McGraw-Hill Book Company, 1978.

[14] M. N. Sadiku and K. Demarest, "Wave Propagation," in *Electronics, Power Electronics, Optoelectronics, Microwaves, Electromagnetics, and Radar: Microwaves, Electromagnetics, and Radar*, 3rd ed., R. C. Dorf, Ed., CRC Press, 2006, pp. 16-1 - 16-5.

[15] T. Q. Ho, J. C. Logan, J. H. Schukantz, F. W. Shaw and R. Q. Welch, "Measurement of Electromagnetic Properties of Composite Materials," 1993.

[16] F. T. Ulaby, R. K. Moore and A. K. Fung, Microwave Remote Sensing, Active and Passive, vol. 3, Artech House, 1986.

[17] J. Wang, "The dielectric properties of soil-water mixtures at microwave frequencies," *Radio Science,* vol. 15, no. 5, pp. 977-985, 1980.

[18] L. F. Chen, C. Ong, C. Neo, V. Varadan and V. K. Varadan, Microwave electronics: measurement and materials characterization, Wiley, 2004.

[19] M. B. Steer and R. J. Trew, "Microwave Devices," in *Electronics, Power Electronics, Optoelectronics, Microwaves, Electromagnetics, and Radar: Microwaves, Electromagnetics, and Radar*, 3rd ed., R. C. Dorf, Ed., CRC Press, 2006, pp. 18-1 - 18-2.

[20] Agilent, "Understanding the Fundamental Principles of Vector Network Analysis," *Application Note,* Vols. 5965-7707E, August 2000.

[21] W. Bridges, M. Klein and E. Schweig, "Measurement of the Dielectric Constant and Loss Tangent of Thallium Mixed Halide Crystals KRS-5 and KRS-6 at 95 GHz," *Microwave Theory and Techniques, IEEE Transactions on,* vol. 30, no. 3, pp. 286-292,

1982.

[22] J. Krupka, K. Derzakowski, B. Riddle and J. Baker-Jarvis, "A dielectric resonator for measurements of complex permittivity of low loss dielectric materials as a function of temperature," *Measurement Science and Technology,* vol. 9, no. 10, p. 1751, 1998.

[23] K. Folgero and T. Tjomsland, "Permittivity measurement of thin liquid layers using open-ended coaxial probes," *Measurement Science and Technology,* vol. 7, no. 8, p. 1164, 1996.

[24] D. Vincent, L. Jorat, J. Monin and G. Noyel, "Improvement of the transmission/reflection method for dielectric and magnetic measurements on liquids between 0.1 and 20 GHz," *Measurement Science and Technology,* vol. 5, no. 8, p. 990, 1994.

[25] S. J. Penn, N. M. Alford, A. Templeton, X. Wang, M. Xu, M. Reece and K. Schrapel, "Effect of porosity and grain size on the microwave dielectric properties of sintered alumina," *Journal of the American Ceramic Society,* vol. 80, no. 7, pp. 1885-1888, 1997.

[26] S. Taylor, Lunar science: A post-Apollo view, 1975.

[27] S. Y. Liao, Microwave Devices and Circuits, 2nd ed., G. Hubit, Ed., Prentice-Hall, 1985.

[28] Agilent, "E5071C ENA Network Analyzer," *Data Sheet,* Vols. 5989-5479EN, August 2012.

[29] R. &. Schwarz, "Measurement of Dielectric Material Properties," 2006.

[30] Agilent, "Agilent Technologies 85051B 7 mm Verification Kit," *User's and Service Guide,* 2013.

[31] General Radio Company, "General Radio Catalog 73," *Catalog,* 1972.

[32] Agilent, "Agilent Technologies 85031B 7 mm Calibration Kit," *User's and Service Guide,* 2010.

[33] Maury Microwave, "Precision Calibration & Interconnect Solutions," *Catalog,* 2013.

[34] Denver Instrument, "Summit Series: Analytical and Toploading Balances,"

Application Note, 2013.

[35] Gilson Company, Inc,, "Performer III 3in Sieve Shaker SS-3," *Operating Manual,* 2013.

[36] C. Weil, M. Janezic and E. Vanzura, "Intercomparison of Permeability and Permittivity Measurements Using the Transmission/Reflection Method in 7 and 14 mm Coaxial Air Lines," 1997.

[37] Agilent, "Specifying Calibration Standards and Kits for Agilent Vector Network Analyzers," *Application Note,* Vols. 5989-4840EN, March 2011.

[38] HP, "Coaxial Systems: Principles of Microwave Connector Care," *Application Note,* Vols. 5954-1566, October 1988.

[39] A. M. Nicolson and G. F. Ross, "Measurement of the Intrinsic Properties of Materials by Time-Domain Techniques," *Instrumentation and Measurement, IEEE Transactions on,* vol. 19, no. 4, pp. 377-382, nov. 1970.

[40] W. Weir, "Automatic measurement of complex dielectric constant and permeability at microwave frequencies," *Proceedings of the IEEE,* vol. 62, no. 1, pp. 33-36, jan. 1974.

[41] J. Baker-Jarvis, E. Vanzura and W. Kissick, "Improved technique for determining complex permittivity with the transmission/reflection method," *Microwave Theory and Techniques, IEEE Transactions on,* vol. 38, no. 8, pp. 1096-1103, aug. 1990.

[42] A.-H. Boughriet, C. Legrand and A. Chapoton, "Noniterative stable transmission/reflection method for low-loss material complex permittivity determination," *Microwave Theory and Techniques, IEEE Transactions on,* vol. 45, no. 1, pp. 52-57, {jan} 1997.

[43] Agilent, "Agilent Vector Network Analyzer Receiver, Dynamic Accuracy: Specifications and Uncertainties," *Technical Overview,* Vols. N5247-90003, September 2011.

[44] L. G. Hector and H. L. Schultz, "The Dielectric Constant of Air at Radiofrequencies," *Physics,* vol. 7, no. 4, pp. 133-136, Apr 1936.

[45] J. V. Hughes and H. Armstrong, "The Dielectric Constant of Dry Air," *Journal of Applied Physics,* vol. 23, no. 5, pp. 501-504, May 1952.

[46] A. R. Jordan, J. W. Broxon and F. C. Walz, "Dependence of the Dielectric Coefficient of Air Upon Pressure and Frequency," *Phys. Rev.*, vol. 46, pp. 66-72, Jul 1934.

[47] W. Phillips, "The Permittivity of Air at a Wavelength of 10 Centimeters," *Proceedings of the IRE,* vol. 38, no. 7, pp. 786-790, July 1950.

[48] C. Matzler, "Microwave permittivity of dry sand," *Geoscience and Remote Sensing, IEEE Transactions on,* vol. 36, no. 1, pp. 317-319, 1998.

[49] E. G. NJOKU and J.-A. Kong, "Theory for passive microwave remote sensing of near-surface soil moisture," *Journal of Geophysical Research,* vol. 82, no. 20, pp. 3108-3118, 1977.

[50] S. Stuchly, "Dielectric properties of some granular solids containing water," *J. Microwave Power,* vol. 5, no. 2, pp. 62-68, 1970.

[51] J. Molla, M. Gonzalez, R. Vila and A. Ibarra, "Effect of humidity on microwave dielectric losses of porous alumina," *Journal of applied physics,* vol. 85, no. 3, pp. 1727-1730, 1999.

[52] R. Vila, M. Gonzalez, J. Molla and A. Ibarra, "Dielectric spectroscopy of alumina ceramics over a wide frequency range," *Journal of nuclear materials,* vol. 253, no. 1, pp. 141-148, 1998.

[53] I. Garcia-Ruiz, C. Aviles-Castron and H. Jardon-Aguilar, "Measuring Complex Permittivity of Materials for Frequencies Under 18 GHz," *Applied microwave and Wireless,* vol. 13, no. 6, pp. 56-85, 2001.

[54] M. Hajian, K. T. Mathew and L. P. Ligthart, "Measurements of complex permittivity with waveguide resonator using perturbation technique," *Microwave and Optical Technology Letters,* vol. 21, no. 4, pp. 269-272, 1999.

[55] S. Nelson and T.-S. You, "Relationships between microwave permittivities of solid and pulverised plastics," *Journal of physics D: applied physics,* vol. 23, no. 3, p. 346,

1990.

[56] M. Yamada, S. Sasaki, H. Nagahara, A. Fujiwara, S. Hasegawa, H. Yano, T. Hiroi, H. Ohashi and H. Otake, "Simulation of space weathering of planet-forming materials: Nanosecond pulse laser irradiation and proton implantation on olivine and pyroxene samples," *Earth Planets and Space,* vol. 51, no. 11, pp. 1255-1265, 1999.

[57] Thermal Product Solutions, "Tenney Junior Series," *Application Note,* 2013.

APPENDICES

Appendix A: MATLAB Code

The code below was written in MATLAB programming language. The NIST Non-Iterative technique was implemented in order to convert the S Parameters, which are imported from comma separated value (CSV) files, into the dielectric constant, loss, and loss tangent. The CSV files are exported from the Network Analyzer and relocated to the working directory of the MATLAB environment. Uncertainty analysis is performed and the results are then plot. Lastly, fifteen evenly spread points along the frequency spectrum, containing permittivity and its corresponding uncertainty data, are output to a CSV file.

```
clear all
clc
format long

%Permittivity Determination using Non-Iterative Method
%MSc Research: Permittivity Measurements
%by Shahroukh Sotodeh
%Lassonde School of Engineering (formerly ESSE Department)


%PROMPT USER FOR NAMING FILES CORRECTLY
user_prompt_input    =    input('Please    enter    the    material/chemical    being
analysed:\n', 's');
chem = user_prompt_input;

user_prompt_input = input('Please enter the particle size in micrometers:\n',
's');
grit = user_prompt_input;

user_prompt_input = input('What sample set is this? (in 0x format):\n', 's');
sample_set = user_prompt_input;


%CHANGE THIS IF NEEDED CHANGE THIS IF NEEDED CHANGE THIS IF NEEDED
%Default parameters if above prompt is commented out

% chem = 'Alumina_Grit_';          %MEASUREMENT SPECIMEN TYPE
% grit = num2str(076);             %PARTICLE SIZE
% sample_set = num2str(01);        %SAMPLE/POPULATION NUMBER
exten = '.csv';


e_0 = 8.854187817620*10^-12;         %Permittivity of vacuum (F/m)
u_0 = 4*pi*10^-7;                    %Permeability of vacuum (V*s/A*m)
```

```
c = (1)*1/sqrt(e_0*u_0);            %Speed of light (m/s)
e_r_air = 1.00058986;               %Dielectric Constant of Air (STP @ 0.9 MHz)

c_air = c / e_r_air;

f_c                                                                             =
0.00000000000000000000000000000000000000000000000000000000000000000000000000000
000000000000000000000000000000001;     %Cut-off frequency (Hz)
lam_c = (c/f_c)*100;    %Cut-off wavelength (cm)


%Data input from files
Nrows = numel(textread('S11_MAG.csv','%1c%*[^\n]')) - 1;
f_0 = csvread('S11_MAG.csv', 3, 0, [3,0,Nrows,0]);
S11_mag = csvread('S11_MAG.csv', 3, 1, [3,1,Nrows,1]);
S11_phase = csvread('S11_PHASE.csv', 3, 1, [3,1,Nrows,1]);
S21_mag = csvread('S21_MAG.csv', 3, 1, [3,1,Nrows,1]);
S21_phase = csvread('S21_PHASE.csv', 3, 1, [3,1,Nrows,1]);

% S22_mag = csvread('S22_MAG.csv', 3, 1, [3,1,Nrows,1]);
% S22_phase = csvread('S22_PHASE.csv', 3, 1, [3,1,Nrows,1]);
% S12_mag = csvread('S12_MAG.csv', 3, 1, [3,1,Nrows,1]);
% S12_phase = csvread('S12_PHASE.csv', 3, 1, [3,1,Nrows,1]);


%Average both sets of S-Parameters
%S11_mag2 = (S11_mag + S22_mag)/2;
S11_mag2 = S11_mag;
%S11_phase2 = (S11_phase + S22_phase)/2;
S11_phase2 = S11_phase;
%S21_mag2 = (S21_mag + S12_mag)/2;
S21_mag2 = S21_mag;
%S21_phase2 = (S21_phase + S12_phase)/2;
S21_phase2 = S21_phase;

%   Coaxial Airline Length
% L = 9.9873;                  %07mm airline - 10 cm
% L = 4.997;                 %14mm airline - 5 cm
% L = 7.495;                  %14mm airline - 7.5 cm
% L = 9.993;                 %14mm airline - 10 cm
 L = 14.9835;                %14mm airline - 15 cm
% L = 29.979;                 %14mm airline - 30 cm

%   Air-gap correction 7mm
D1 = 0.30404; %7mm airline centre-conductor diameter (cm)
D4 = 0.69926; %7mm airline outer diameter (cm)
D2 = 0.30658; %Rexolite sample inner diameter (cm)
D3 = 0.69646; %Rexolite sample outer diameter (cm)

% % Air-gap correction 14mm
% D1 = 0.62052; %14mm airline centre-conductor diameter (cm)
% D4 = 1.42824; %14mm airline outer diameter (cm)
% D2 = 0.62128; %Rexolite sample inner diameter (cm)
% D3 = 1.42341; %Rexolite sample outer diameter (cm)

L1 = log(D2/D1) + log(D4/D3);
L2 = log(D4/D1);
L3 = log(D3/D2);
```

```
%Pre-allocate some arrays and matrices for speed
wave = zeros(1, length(f_0));
harmonic = zeros(1, length(f_0));

lam_0 = zeros(1, length(f_0));
S11 = zeros(1, length(f_0));
S21 = zeros(1, length(f_0));
V1 = zeros(1, length(f_0));
V2 = zeros(1, length(f_0));
X = zeros(1, length(f_0));
gam = zeros(1, length(f_0));
T = zeros(1, length(f_0));
ln_1_T = zeros(1, length(f_0));
A = zeros(1, length(f_0));
lam_og = zeros(1, length(f_0));
mu_eff = zeros(1, length(f_0));
ep_eff = zeros(1, length(f_0));
mu_r = zeros(1, length(f_0));
ep_r = zeros(1, length(f_0));

mu_r_dS11mag = zeros(1, length(f_0));
ep_r_dS11mag = zeros(1, length(f_0));
mu_r_dS21mag = zeros(1, length(f_0));
ep_r_dS21mag = zeros(1, length(f_0));
mu_r_dS11phase = zeros(1, length(f_0));
ep_r_dS11phase = zeros(1, length(f_0));
mu_r_dS21phase = zeros(1, length(f_0));
ep_r_dS21phase = zeros(1, length(f_0));

dielec = zeros(1, length(f_0));
lossfac = zeros(1, length(f_0));
losstan = zeros(1, length(f_0));


%New Dielectric Constant and Dielectric Loss values
%due to respective S-Parameter errors
dielec_dS11mag = zeros(1, length(f_0));
lossfac_dS11mag = zeros(1, length(f_0));
losstan_dS11mag = zeros(1, length(f_0));
dielec_dS21mag = zeros(1, length(f_0));
lossfac_dS21mag = zeros(1, length(f_0));
losstan_dS21mag = zeros(1, length(f_0));

dielec_dS11phase = zeros(1, length(f_0));
lossfac_dS11phase = zeros(1, length(f_0));
losstan_dS11phase = zeros(1, length(f_0));
dielec_dS21phase = zeros(1, length(f_0));
lossfac_dS21phase = zeros(1, length(f_0));
losstan_dS21phase = zeros(1, length(f_0));


%Air-gap CORRECTED Dielectric Constant and Dielectric Loss
dielec_corr = zeros(1, length(f_0));
lossfac_corr = zeros(1, length(f_0));
losstan_corr = zeros(1, length(f_0));


%Uncertainties
```

```
S11_mag_upper = zeros(1, length(f_0));
delta_S11_mag_dB = zeros(1, length(f_0));          %dB
delta_S11_mag = zeros(1, length(f_0));          %unitless

S11_phase_upper = zeros(1, length(f_0));
delta_S11_phase = zeros(1, length(f_0));        %degrees

S21_mag_upper = zeros(1, length(f_0));
delta_S21_mag_dB = zeros(1, length(f_0));          %dB
delta_S21_mag = zeros(1, length(f_0));          %unitless

S21_phase_upper = zeros(1, length(f_0));
delta_S21_phase = zeros(1, length(f_0));        %degrees

delta_length = 0.001;               %in cm
delta_D1 = 0.00025;                 %in cm
delta_D2 = 0.00025;
delta_D3 = 0.00025;
delta_D4 = 0.00025;
delta_ermreal = zeros(1, length(f_0));
delta_ermimag = zeros(1, length(f_0));
delta_ermtan = zeros(1, length(f_0));


%Final uncertainties due to S-Parameters, length, and air-gaps (includes
%others)
error_dielec_Sparam = zeros(1,length(f_0));
error_lossfac_Sparam = zeros(1,length(f_0));
error_losstan_Sparam = zeros(1,length(f_0));

error_dielec_length = zeros(1, length(f_0));
error_lossfac_length = zeros(1, length(f_0));
error_losstan_length = zeros(1, length(f_0));

error_dielec_airgap = zeros(1, length(f_0));
error_lossfac_airgap = zeros(1, length(f_0));
error_losstan_airgap = zeros(1, length(f_0));


percenterror_S_param_dielec = zeros(1,length(f_0));
percenterror_S_param_lossfac = zeros(1,length(f_0));
percenterror_S_param_losstan = zeros(1,length(f_0));

percenterror_length_dielec = zeros(1,length(f_0));
percenterror_length_lossfac = zeros(1,length(f_0));
percenterror_length_losstan = zeros(1,length(f_0));

percenterror_airgap_dielec = zeros(1,length(f_0));
percenterror_airgap_lossfac = zeros(1,length(f_0));
percenterror_airgap_losstan = zeros(1,length(f_0));


%Final uncertainties due to S Parameters and Length combined
error_dielec_total = zeros(1, length(f_0));
error_lossfac_total = zeros(1, length(f_0));
error_losstan_total = zeros(1, length(f_0));

percenterror_total_dielec = zeros(1,length(f_0));
```

```
percenterror_total_lossfac = zeros(1,length(f_0));
percenterror_total_losstan = zeros(1,length(f_0));



n=0;
freq_flag = 0;
sign = 0;



%----------------------SECTION I-----------------------
%CALCULATE UNCERTAINTY IN MAG AND PHASE of S-PARAMETERS
%       INPUT UNCERTAINTY INTO NEW S-PARAMETERS
%------------------------------------------------------

for i=1:length(f_0)
    %Magnitude Dynamic Accuracy
    delta_S11_mag_dB(i) = - 1.6866e-017*( 20*log10(S11_mag2(i)) )^10 - 5.7972e-
015*( 20*log10(S11_mag2(i)) )^9 - 7.7776e-013*( 20*log10(S11_mag2(i)) )^8 -
4.9817e-011*( 20*log10(S11_mag2(i)) )^7 - 1.3321e-009*( 20*log10(S11_mag2(i))
)^6    +    7.9937e-009*(    20*log10(S11_mag2(i))    )^5    +    1.1928e-006*(
20*log10(S11_mag2(i)) )^4 + 1.9484e-005*( 20*log10(S11_mag2(i)) )^3 + 3.8701e-
005*( 20*log10(S11_mag2(i)) )^2 - 0.0016659*( 20*log10(S11_mag2(i)) ) +
0.024593;
    delta_S21_mag_dB(i) = - 1.6866e-017*( 20*log10(S21_mag2(i)) )^10 - 5.7972e-
015*( 20*log10(S21_mag2(i)) )^9 - 7.7776e-013*( 20*log10(S21_mag2(i)) )^8 -
4.9817e-011*( 20*log10(S21_mag2(i)) )^7 - 1.3321e-009*( 20*log10(S21_mag2(i))
)^6    +    7.9937e-009*(    20*log10(S21_mag2(i))    )^5    +    1.1928e-006*(
20*log10(S21_mag2(i)) )^4 + 1.9484e-005*( 20*log10(S21_mag2(i)) )^3 + 3.8701e-
005*( 20*log10(S21_mag2(i)) )^2 - 0.0016659*( 20*log10(S21_mag2(i)) ) +
0.024593;

    %Phase Dynamic Accuracy
    delta_S11_phase(i) = 9.6451e-018*( 20*log10(S11_mag2(i)) )^10 + 4.8901e-
015*( 20*log10(S11_mag2(i)) )^9 + 1.1884e-012*( 20*log10(S11_mag2(i)) )^8 +
1.5829e-010*( 20*log10(S11_mag2(i)) )^7 + 1.2006e-008*( 20*log10(S11_mag2(i))
)^6    +    5.1271e-007*(    20*log10(S11_mag2(i))    )^5    +    1.1348e-005*(
20*log10(S11_mag2(i)) )^4 + 9.2704e-005*( 20*log10(S11_mag2(i)) )^3 -
0.00030021*( 20*log10(S11_mag2(i)) )^2 - 0.011088*( 20*log10(S11_mag2(i)) ) +
0.16977;
    delta_S21_phase(i) = 9.6451e-018*( 20*log10(S21_mag2(i)) )^10 + 4.8901e-
015*( 20*log10(S21_mag2(i)) )^9 + 1.1884e-012*( 20*log10(S21_mag2(i)) )^8 +
1.5829e-010*( 20*log10(S21_mag2(i)) )^7 + 1.2006e-008*( 20*log10(S21_mag2(i))
)^6    +    5.1271e-007*(    20*log10(S21_mag2(i))    )^5    +    1.1348e-005*(
20*log10(S21_mag2(i)) )^4 + 9.2704e-005*( 20*log10(S21_mag2(i)) )^3 -
0.00030021*( 20*log10(S21_mag2(i)) )^2 - 0.011088*( 20*log10(S21_mag2(i)) ) +
0.16977;

    %Add ERROR for UPPER bound (multiplication due to log rules)
    S11_mag_upper(i) = S11_mag2(i) * 10^(delta_S11_mag_dB(i) / 20);
    S21_mag_upper(i) = S21_mag2(i) * 10^(delta_S21_mag_dB(i) / 20);


    S11_phase_upper(i) = S11_phase2(i) + delta_S11_phase(i);
    S21_phase_upper(i) = S21_phase2(i) + delta_S21_phase(i);

    if(S11_phase_upper(i) > 180)
        S11_phase_upper(i) = S11_phase_upper(i) - 360;
```

```
    end

    if(S21_phase_upper(i) > 180)
        S21_phase_upper(i) = S21_phase_upper(i) - 360;
    end

end



%-----                                   -----
%---------------SECTION II-----------------
%CALCULATE PERMITTIVITY FROM COLLECTED DATA
%-----------------------------------------
%-----                                   -----

for i=1:length(f_0)

    lam_0(i) = (c/f_0(i))*100;    %Free-space wavelength (cm)

    %Convert to rectangular notation
    S11(i)                                                                  =
complex(S11_mag2(i)*cosd(S11_phase2(i)),S11_mag2(i)*sind(S11_phase2(i)));
    S21(i)                                                                  =
complex(S21_mag2(i)*cosd(S21_phase2(i)),S21_mag2(i)*sind(S21_phase2(i)));

    % Calculate X (root of reflection coefficient) from equation (1.2)
    V1(i) = S21(i) + S11(i);
    V2(i) = S21(i) - S11(i);

    X(i) = (1 - V1(i)*V2(i)) / (V1(i) - V2(i));


    % Calculate Gamma (reflection coefficient) from equation (1.1)
    gam(i) = 0;
    gam1 = X(i) + sqrt(X(i)^2 - 1);
    gam2 = X(i) - sqrt(X(i)^2 - 1);

    % Determine correct root with condition |GAMMA| < 1
    if(abs(gam1) < 1)
        gam(i) = gam1;
        if(i==1)
            sign = 1;
        end

        sign = 1;
    else
        gam(i) = gam2;
        if(i==1)
            sign = 2;
        end

        sign = 2;
    end

    % Calculate T (transmission coefficient) from equation (1.3)
    T(i) = (S11(i) + S21(i) - gam(i)) / (1 - (S11(i) + S21(i)) * gam(i));
```

```
    %Find wavelength in sample to find root n to solve for phase ambiguity
    if(i ~= length(f_0))
        if(  ((S21_phase2(i)  <  0.00000  &&  S21_phase2(i)  >=  -179.99000)  &&
(S21_phase2(i+1) >= 0.00000 || S21_phase2(i+1) < -179.99000)) )

            ln_1_T(i)     =     complex(log(1/(real(T(i))^2+imag(T(i))^2)^0.5),-
1*atan2(imag(T(i)),real(T(i))) + 2*pi*n);

            n=n+1;

            if n==1
                freq_flag = i;
            end
        else
            ln_1_T(i)     =     complex(log(1/(real(T(i))^2+imag(T(i))^2)^0.5),-
1*atan2(imag(T(i)),real(T(i))) + 2*pi*n);
        end
    elseif(i == length(f_0))
        %do nothing
        ln_1_T(i)       =       complex(log(1/(real(T(i))^2+imag(T(i))^2)^0.5),-
1*atan2(imag(T(i)),real(T(i))) + 2*pi*n);

    end

    if i==337
        fprintf('Regular\n');
        ln_1_T(i)
    end

    % Calculate A from equation (3.4)
    A(i) = 1 / sqrt(-(ln_1_T(i) / (2 * pi * L))^2);

    %Find wavelength in empty cell
    lam_og(i) = 1 / sqrt(1/lam_0(i)^2 - 1/lam_c^2);

    %Assume non-magnetic materials only
    mu_eff(i) = 1;
    ep_eff(i) = (lam_og(i)/A(i))^2 ;

%     mu_eff(i) = (lam_og(i)/A(i)) * ((1+gam(i)) / (1-gam(i)));
%     ep_eff(i) = (lam_og(i)/A(i)) * ((1-gam(i)) / (1+gam(i)));

    % Calculate u_eff (effective permeability) from equation (3.6)
    mu_r(i) = mu_eff(i);

    % Calculate e_eff (effective permittivity) from equation (3.7)
    ep_r(i)     =     (     1     -     lam_0(i)^2/lam_c^2     )*ep_eff(i)     +
(lam_0(i)^2/lam_c^2)/mu_eff(i);
    dielec(i) = real(ep_r(i));
    lossfac(i) = -imag(ep_r(i));
    losstan(i) = lossfac(i)/dielec(i);

    %Air-gap correction (Series of Capacitors model)
    dielec_corr(i) = dielec(i) * (L2 / (L3 - dielec(i)*L1));
    lossfac_corr(i)  =  (dielec_corr(i)*lossfac(i)/dielec(i))  *  L3  /  (  L3-
L1*dielec(i) * (1 + (lossfac(i)/dielec(i))^2) );
    losstan_corr(i) = lossfac_corr(i)/dielec_corr(i);
```

```
    %----------------------------------------
    % -------UNCERTAINTY/ERROR ANALYSIS-------
    %----------------------------------------

    delta_S11_mag(i) = abs(S11_mag_upper(i) - S11_mag2(i));
    delta_S21_mag(i) = abs(S21_mag_upper(i) - S21_mag2(i));


    %Uncertainty due to S-Parameters
    if sign == 1
        %Positive GAMMA ROOT
        error_dielec_Sparam(i)  =  abs(  sqrt(  real(  der_S11mag(S11_mag2(i),
S21_mag2(i), S11_phase2(i), S21_phase2(i), L, lam_0(i), lam_c, lam_og(i)) )^2 *
delta_S11_mag(i)^2 + real( der_S21mag(S11_mag2(i), S21_mag2(i), S11_phase2(i),
S21_phase2(i), L, lam_0(i), lam_c, lam_og(i)) )^2 * delta_S21_mag(i)^2 + real(
der_S11phase(S11_mag2(i),   S21_mag2(i),   S11_phase2(i),   S21_phase2(i),   L,
lam_0(i),   lam_c,   lam_og(i))   )^2   *   delta_S11_phase(i)^2   +   real(
der_S21phase(S11_mag2(i),   S21_mag2(i),   S11_phase2(i),   S21_phase2(i),   L,
lam_0(i), lam_c, lam_og(i)) )^2 * delta_S21_phase(i)^2 ) );
        error_lossfac_Sparam(i)  =  abs(  sqrt(  imag(  der_S11mag(S11_mag2(i),
S21_mag2(i), S11_phase2(i), S21_phase2(i), L, lam_0(i), lam_c, lam_og(i)) )^2 *
delta_S11_mag(i)^2 + imag( der_S21mag(S11_mag2(i), S21_mag2(i), S11_phase2(i),
S21_phase2(i), L, lam_0(i), lam_c, lam_og(i)) )^2 * delta_S21_mag(i)^2 + imag(
der_S11phase(S11_mag2(i),   S21_mag2(i),   S11_phase2(i),   S21_phase2(i),   L,
lam_0(i),   lam_c,   lam_og(i))   )^2   *   delta_S11_phase(i)^2   +   imag(
der_S21phase(S11_mag2(i),   S21_mag2(i),   S11_phase2(i),   S21_phase2(i),   L,
lam_0(i), lam_c, lam_og(i)) )^2 * delta_S21_phase(i)^2 ) );
        error_losstan_Sparam(i)       =       losstan(i)       *       sqrt(
(error_dielec_Sparam(i)/dielec(i))^2   +   (error_lossfac_Sparam(i)/lossfac(i))^2
);
    elseif sign == 2
        %NEGATIVE GAMMA ROOT
        error_dielec_Sparam(i) = abs( sqrt( real( der_S11mag_neg(S11_mag2(i),
S21_mag2(i), S11_phase2(i), S21_phase2(i), L, lam_0(i), lam_c, lam_og(i)) )^2 *
delta_S11_mag(i)^2    +    real(    der_S21mag_neg(S11_mag2(i),    S21_mag2(i),
S11_phase2(i),   S21_phase2(i),   L,   lam_0(i),   lam_c,   lam_og(i))   )^2   *
delta_S21_mag(i)^2    +    real(    der_S11phase_neg(S11_mag2(i),    S21_mag2(i),
S11_phase2(i),   S21_phase2(i),   L,   lam_0(i),   lam_c,   lam_og(i))   )^2   *
delta_S11_phase(i)^2   +   real(   der_S21phase_neg(S11_mag2(i),   S21_mag2(i),
S11_phase2(i),   S21_phase2(i),   L,   lam_0(i),   lam_c,   lam_og(i))   )^2   *
delta_S21_phase(i)^2 ) );
        error_lossfac_Sparam(i) = abs( sqrt( imag( der_S11mag_neg(S11_mag2(i),
S21_mag2(i), S11_phase2(i), S21_phase2(i), L, lam_0(i), lam_c, lam_og(i)) )^2 *
delta_S11_mag(i)^2    +    imag(    der_S21mag_neg(S11_mag2(i),    S21_mag2(i),
S11_phase2(i),   S21_phase2(i),   L,   lam_0(i),   lam_c,   lam_og(i))   )^2   *
delta_S21_mag(i)^2    +    imag(    der_S11phase_neg(S11_mag2(i),    S21_mag2(i),
S11_phase2(i),   S21_phase2(i),   L,   lam_0(i),   lam_c,   lam_og(i))   )^2   *
delta_S11_phase(i)^2   +   imag(   der_S21phase_neg(S11_mag2(i),   S21_mag2(i),
S11_phase2(i),   S21_phase2(i),   L,   lam_0(i),   lam_c,   lam_og(i))   )^2   *
delta_S21_phase(i)^2 ) );
        error_losstan_Sparam(i)       =       losstan(i)       *       sqrt(
(error_dielec_Sparam(i)/dielec(i))^2   +   (error_lossfac_Sparam(i)/lossfac(i))^2
);
    end

    %Uncertainty due to length
    error_dielec_length(i)  =  abs(  sqrt(  real(  der_dL(gam(i),  ln_1_T(i),  L,
lam_0(i), lam_c, lam_og(i)) )^2 * delta_length^2 ) );
```

```
    error_lossfac_length(i) = abs( sqrt( imag( der_dL(gam(i), ln_1_T(i), L,
lam_0(i), lam_c, lam_og(i)) )^2 * delta_length^2 ) );
    error_losstan_length(i)         =         losstan(i)         *         sqrt(
(error_dielec_length(i)/dielec(i))^2   +   (error_lossfac_length(i)/lossfac(i))^2
);

    %Combine all uncertainties in measured (m) Permittivity due to
    %S-Parameters and Length
    delta_ermreal(i)       =       sqrt(       error_dielec_Sparam(i)^2       +
error_dielec_length(i)^2 );
    delta_ermimag(i)       =       sqrt(       error_lossfac_Sparam(i)^2       +
error_lossfac_length(i)^2 );
    delta_ermtan(i)  =  losstan(i)  *  sqrt(  (delta_ermreal(i)/dielec(i))^2  +
(delta_ermimag(i)/lossfac(i))^2 );

    %Uncertainty due to air-gaps
    error_dielec_airgap(i) = abs( sqrt( dercreal_dielec(dielec(i), D1, D2, D3,
D4)^2  *  delta_ermreal(i)^2  +  dercreal_D1(dielec(i),  D1,  D2,  D3,  D4)^2  *
delta_D1^2  +  dercreal_D2(dielec(i),  D1,  D2,  D3,  D4)^2  *  delta_D2^2  +
dercreal_D3(dielec(i), D1, D2, D3, D4)^2 * delta_D3^2 + dercreal_D4(dielec(i),
D1, D2, D3, D4)^2 * delta_D4^2 ) );
    error_lossfac_airgap(i) = abs( sqrt( dercimag_dielec(dielec(i), lossfac(i),
D1,  D2,  D3,  D4)^2  *  delta_ermreal(i)^2  +  dercimag_lossfac(dielec(i),
lossfac(i),  D1,  D2,  D3,  D4)^2  *  delta_ermimag(i)^2  +  dercimag_D1(dielec(i),
lossfac(i), D1, D2, D3, D4)^2 * delta_D1^2 + dercimag_D2(dielec(i), lossfac(i),
D1, D2, D3, D4)^2 * delta_D2^2 + dercimag_D3(dielec(i), lossfac(i), D1, D2, D3,
D4)^2  *  delta_D3^2  +  dercimag_D4(dielec(i),  lossfac(i),  D1,  D2,  D3,  D4)^2  *
delta_D4^2 ) );
    error_losstan_airgap(i)         =         losstan(i)         *         sqrt(
(error_dielec_airgap(i)/dielec(i))^2   +   (error_lossfac_airgap(i)/lossfac(i))^2
);



    wave(i) = (sqrt((sqrt(dielec(i)^2 + lossfac(i)^2) + dielec(i)) / 2));
    harmonic(i) = mod(2*(L/10)*wave(i)*f_0(i),299792458);
end



lambda = zeros(1,length(f_0));
ratio_line = zeros(1,length(f_0));

for i=1:length(f_0)
    lambda(i) = c/f_0(i) *100;
    ratio_line(i) = L/lambda(i);
end

for i=1:length(f_0)
    percenterror_S_param_dielec(i) = 100*error_dielec_Sparam(i)/dielec(i);
    percenterror_S_param_lossfac(i) = 100*error_lossfac_Sparam(i)/lossfac(i);
    percenterror_S_param_losstan(i) = 100*error_losstan_Sparam(i)/losstan(i);

    percenterror_length_dielec(i) = 100*error_dielec_length(i)/dielec(i);
    percenterror_length_lossfac(i) = 100*error_lossfac_length(i)/lossfac(i);
    percenterror_length_losstan(i) = 100*error_losstan_length(i)/losstan(i);

    percenterror_airgap_dielec(i) = 100*error_dielec_airgap(i)/dielec(i);
    percenterror_airgap_lossfac(i) = 100*error_lossfac_airgap(i)/lossfac(i);
```

```
    percenterror_airgap_losstan(i) = 100*error_losstan_airgap(i)/losstan(i);

    percenterror_total_dielec(i) = 100*delta_ermreal(i)/dielec(i);
    percenterror_total_lossfac(i) = 100*delta_ermimag(i)/lossfac(i);
    percenterror_total_losstan(i) = 100*delta_ermtan(i)/losstan(i);
end

[p,ErrorEst] = polyfit(ratio_line,error_dielec_Sparam,5);
pop_fit1 = polyval(p,ratio_line,ErrorEst);

[p,ErrorEst] = polyfit(ratio_line,error_lossfac_Sparam,5);
pop_fit2 = polyval(p,ratio_line,ErrorEst);


%-----                                              -----
%-------------------SECTION III---------------------
%                     PLOT DATA
%-------------------------------------------------------
%-----                                              -----


figure(1)
subplot(311)
errorbar(f_0, dielec, error_dielec_Sparam,'ok')
title('Permittivity of Air')
xlabel('Frequency (Hz)')
xlim([500*10^6 8*10^9])
ylabel('\epsilon_r''')
legend('Raw Data','Confidence Intervals due to S-Parameter Uncertainties')
grid on

figure(1)
subplot(312)
plot(f_0, lossfac, 'color', 'b', 'linestyle', '-', 'linewidth', 2)
line(f_0,  lossfac+error_lossfac_Sparam,  'color',  'r',  'linestyle',  '--',
'linewidth', 1);
line(f_0,  lossfac-error_lossfac_Sparam,  'color',  'r',  'linestyle',  '--',
'linewidth', 1);
xlabel('Frequency (Hz)')
xlim([500*10^6 8*10^9])
ylabel('\epsilon_r''''')
grid on

figure(1)
subplot(313)
errorbar(f_0, losstan, error_losstan_Sparam,'ok')
xlabel('Frequency (Hz)')
xlim([500*10^6 8*10^9])
ylabel('tan \delta')
grid on


figure(2)
subplot(311)
plot(f_0, dielec, 'color', 'b', 'linestyle', '-', 'linewidth', 2)
line(f_0,  dielec  +  error_dielec_length,  'color',  'r',  'linestyle',  '--',
'linewidth', 1);
line(f_0,  dielec  -  error_dielec_length,  'color',  'r',  'linestyle',  '--',
'linewidth', 1);
```

```
title('Permittivity of Air')
xlabel('Frequency (Hz)')
xlim([500*10^6 8*10^9])
ylabel('\epsilon_r''')
legend('Raw Data','Confidence Intervals due to Length Uncertainties')
grid on

figure(2)
subplot(312)
plot(f_0, lossfac, 'color', 'b', 'linestyle', '-', 'linewidth', 2)
line(f_0, lossfac + error_lossfac_length, 'color', 'r', 'linestyle', '--',
'linewidth', 1);
line(f_0, lossfac - error_lossfac_length, 'color', 'r', 'linestyle', '--',
'linewidth', 1);
xlabel('Frequency (Hz)')
xlim([500*10^6 8*10^9])
ylabel('\epsilon_r''''')
grid on

figure(2)
subplot(313)
plot(f_0, losstan, 'color', 'b', 'linestyle', '-', 'linewidth', 2)
line(f_0, losstan + error_losstan_length, 'color', 'r', 'linestyle', '--',
'linewidth', 1);
line(f_0, losstan - error_losstan_length, 'color', 'r', 'linestyle', '--',
'linewidth', 1);
xlabel('Frequency (Hz)')
xlim([500*10^6 8*10^9])
ylabel('tan \delta')
grid on


figure(3)
subplot(311)
plot(f_0, dielec, 'color', 'b', 'linestyle', '-', 'linewidth', 2)
line(f_0, dielec + delta_ermreal, 'color', 'r', 'linestyle', '--', 'linewidth',
1);
line(f_0, dielec - delta_ermreal, 'color', 'r', 'linestyle', '--', 'linewidth',
1);
title({'Permittivity of Alumina Grit vs. Frequency (7mm Coaxial Airline)',
'102\mum, \phi = 0.483 +/- 0.003'})
xlabel('Frequency (Hz)')
xlim([500*10^6 8*10^9])
ylabel('\epsilon_r''')
legend('Raw Data','Confidence Intervals due to S-Parameter and Length
Uncertainties')
grid on

figure(3)
subplot(312)
plot(f_0, lossfac, 'color', 'b', 'linestyle', '-', 'linewidth', 2)
line(f_0, lossfac + delta_ermimag, 'color', 'r', 'linestyle', '--',
'linewidth', 1);
line(f_0, lossfac - delta_ermimag, 'color', 'r', 'linestyle', '--',
'linewidth', 1);
xlabel('Frequency (Hz)')
xlim([500*10^6 8*10^9])
ylabel('\epsilon_r''''')
grid on
```

```
figure(3)
subplot(313)
plot(f_0, losstan, 'color', 'b', 'linestyle', '-', 'linewidth', 2)
line(f_0, losstan + delta_ermtan, 'color', 'r', 'linestyle', '--', 'linewidth',
1);
line(f_0, losstan - delta_ermtan, 'color', 'r', 'linestyle', '--', 'linewidth',
1);
xlabel('Frequency (Hz)')
xlim([500*10^6 8*10^9])
ylabel('tan \delta')
grid on


figure(10)
subplot(311)
plot(f_0, dielec, 'color', 'b', 'linestyle', '-', 'linewidth', 2)
line(f_0, dielec + delta_ermreal, 'color', 'r', 'linestyle', '--', 'linewidth',
1);
line(f_0, dielec - delta_ermreal, 'color', 'r', 'linestyle', '--', 'linewidth',
1);
title({'Permittivity of Alumina Grit vs. Frequency (7mm Coaxial Airline)',
'102\mum, \phi = 0.483 +/- 0.003'})
xlabel('Frequency (Hz)')
xlim([500*10^6 8*10^9])
ylabel('\epsilon_r''')
legend('Raw Data','Confidence Intervals due to S-Parameter and Length
Uncertainties')
grid on

figure(10)
subplot(312)
plot(f_0, lossfac, 'color', 'b', 'linestyle', '-', 'linewidth', 2)
line(f_0, lossfac + delta_ermimag, 'color', 'r', 'linestyle', '--',
'linewidth', 1);
line(f_0, lossfac - delta_ermimag, 'color', 'r', 'linestyle', '--',
'linewidth', 1);
xlabel('Frequency (Hz)')
xlim([500*10^6 8*10^9])
ylabel('\epsilon_r''''')
grid on

figure(10)
subplot(313)
plot(f_0, losstan, 'color', 'b', 'linestyle', '-', 'linewidth', 2)
line(f_0, losstan + delta_ermtan, 'color', 'r', 'linestyle', '--', 'linewidth',
1);
line(f_0, losstan - delta_ermtan, 'color', 'r', 'linestyle', '--', 'linewidth',
1);
xlabel('Frequency (Hz)')
xlim([500*10^6 8*10^9])
ylabel('tan \delta')
grid on


figure(4)
subplot(311)
measure = plot(f_0, dielec_corr, 'color', 'b', 'linestyle', '-', 'linewidth',
2)
```

```
line(f_0, dielec_corr + error_dielec_airgap, 'color', 'r', 'linestyle', '--',
'linewidth', 1);
line(f_0, dielec_corr - error_dielec_airgap, 'color', 'r', 'linestyle', '--',
'linewidth', 1);
title({'Permittivity of Pure Silica Sand (150-250 \mum, \phi = 0.37)','Measured
with a 14mm airline (15cm length)'})
xlabel('Frequency (Hz)')
xlim([500*10^6 8*10^9])
ylabel('\epsilon_r''')
set(get(get(measure,'Annotation'),'LegendInformation'),...
    'IconDisplayStyle','off');
legend('Confidence Intervals due to S-Parameter, Length, and Air-Gap
Uncertainties')
grid on

figure(4)
subplot(312)
plot(f_0, lossfac_corr, 'color', 'b', 'linestyle', '-', 'linewidth', 2)
line(f_0, lossfac_corr + error_lossfac_airgap, 'color', 'r', 'linestyle', '--',
'linewidth', 1);
line(f_0, lossfac_corr - error_lossfac_airgap, 'color', 'r', 'linestyle', '--',
'linewidth', 1);
xlabel('Frequency (Hz)')
xlim([500*10^6 8*10^9])
ylabel('\epsilon_r''''')
grid on

figure(4)
subplot(313)
plot(f_0, losstan_corr, 'color', 'b', 'linestyle', '-', 'linewidth', 2)
line(f_0, losstan_corr + error_losstan_airgap, 'color', 'r', 'linestyle', '--',
'linewidth', 1);
line(f_0, losstan_corr - error_losstan_airgap, 'color', 'r', 'linestyle', '--',
'linewidth', 1);
xlabel('Frequency (Hz)')
xlim([500*10^6 8*10^9])
ylabel('tan \delta')
grid on



dielec_smooth = smooth(dielec,0.15,'rloess');
lossfac_smooth = smooth(lossfac,0.15,'rloess');
losstan_smooth = smooth(losstan,0.15,'rloess');

error_dielec_total_smooth = smooth(delta_ermreal,0.15,'rloess');
error_lossfac_total_smooth = smooth(delta_ermimag,0.15,'rloess');
error_losstan_total_smooth = smooth(delta_ermtan,0.15,'rloess');

figure(5)
subplot(311)
plot(f_0, dielec_smooth, 'color', 'b', 'linestyle', '-', 'linewidth', 2)
line(f_0, dielec_smooth + error_dielec_total_smooth, 'color', 'r', 'linestyle',
'--', 'linewidth', 1);
line(f_0, dielec_smooth - error_dielec_total_smooth, 'color', 'r', 'linestyle',
'--', 'linewidth', 1);
title('Permittivity of Air')
xlabel('Frequency (Hz)')
xlim([500*10^6 8*10^9])
```

```
ylabel('\epsilon_r''')
legend('Raw Data','Confidence Intervals due to S-Parameter, Length, and Air-gap
Uncertainties')
grid on

figure(5)
subplot(312)
plot(f_0, lossfac_smooth, 'color', 'b', 'linestyle', '-', 'linewidth', 2)
line(f_0,   lossfac_smooth   +   error_lossfac_total_smooth,   'color',   'r',
'linestyle', '--', 'linewidth', 1);
line(f_0,   lossfac_smooth   -   error_lossfac_total_smooth,   'color',   'r',
'linestyle', '--', 'linewidth', 1);
xlabel('Frequency (Hz)')
xlim([500*10^6 8*10^9])
ylabel('\epsilon_r''''')
grid on

figure(5)
subplot(313)
plot(f_0, losstan_smooth, 'color', 'b', 'linestyle', '-', 'linewidth', 2)
line(f_0,   losstan_smooth   +   error_losstan_total_smooth,   'color',   'r',
'linestyle', '--', 'linewidth', 1);
line(f_0,   losstan_smooth   -   error_losstan_total_smooth,   'color',   'r',
'linestyle', '--', 'linewidth', 1);
xlabel('Frequency (Hz)')
xlim([500*10^6 8*10^9])
ylabel('tan \delta')
grid on

figure(6)
subplot(311)
plot(ratio_line, pop_fit1,'-',ratio_line, error_dielec_Sparam,'o')
title('Error due to S-parameter uncertainty')
xlabel('L/\lambda')
ylabel('error (Dielectric Constant)')
grid on

figure(6)
subplot(312)
plot(ratio_line,pop_fit2,'-',ratio_line, error_lossfac_Sparam,'o')
xlabel('L/\lambda')
ylabel('error (Dielectric Loss)')
grid on

figure(6)
subplot(313)
plot(ratio_line,pop_fit2,'-',ratio_line, error_losstan_Sparam,'o')
xlabel('L/\lambda')
ylabel('error (Loss Tangent)')
grid on



%-----                                                  -----
%---------------------SECTION IV----------------------
%WRITE PARTICULAR FREQUENCY DATA TO FILES FOR ANALYSIS
%-----------------------------------------------------
%-----                                                  -----
```

```
output = zeros(15,5);

output(1,1) = dielec(find(f_0==100000000));
output(1,2) = lossfac(find(f_0==100000000));
output(1,3) = delta_ermreal(find(f_0==100000000));
output(1,4) = delta_ermimag(find(f_0==100000000));
output(1,5) = delta_ermtan(find(f_0==100000000));

output(2,1) = dielec(find(f_0==495000000));
output(2,2) = lossfac(find(f_0==495000000));
output(2,3) = delta_ermreal(find(f_0==495000000));
output(2,4) = delta_ermimag(find(f_0==495000000));
output(2,5) = delta_ermtan(find(f_0==495000000));

output(3,1) = dielec(find(f_0==1.008500000000000e+09));
output(3,2) = lossfac(find(f_0==1.008500000000000e+09));
output(3,3) = delta_ermreal(find(f_0==1.008500000000000e+09));
output(3,4) = delta_ermimag(find(f_0==1.008500000000000e+09));
output(3,5) = delta_ermtan(find(f_0==1.008500000000000e+09));

output(4,1) = dielec(find(f_0==1.502250000000000e+09));
output(4,2) = lossfac(find(f_0==1.502250000000000e+09));
output(4,3) = delta_ermreal(find(f_0==1.502250000000000e+09));
output(4,4) = delta_ermimag(find(f_0==1.502250000000000e+09));
output(4,5) = delta_ermtan(find(f_0==1.502250000000000e+09));

output(5,1) = dielec(find(f_0==2.015750000000000e+09));
output(5,2) = lossfac(find(f_0==2.015750000000000e+09));
output(5,3) = delta_ermreal(find(f_0==2.015750000000000e+09));
output(5,4) = delta_ermimag(find(f_0==2.015750000000000e+09));
output(5,5) = delta_ermtan(find(f_0==2.015750000000000e+09));

output(6,1) = dielec(find(f_0==2.549000000000000e+09));
output(6,2) = lossfac(find(f_0==2.549000000000000e+09));
output(6,3) = delta_ermreal(find(f_0==2.549000000000000e+09));
output(6,4) = delta_ermimag(find(f_0==2.549000000000000e+09));
output(6,5) = delta_ermtan(find(f_0==2.549000000000000e+09));

output(7,1) = dielec(find(f_0==2.983500000000000e+09));
output(7,2) = lossfac(find(f_0==2.983500000000000e+09));
output(7,3) = delta_ermreal(find(f_0==2.983500000000000e+09));
output(7,4) = delta_ermimag(find(f_0==2.983500000000000e+09));
output(7,5) = delta_ermtan(find(f_0==2.983500000000000e+09));

output(8,1) = dielec(find(f_0==3.497000000000000e+09));
output(8,2) = lossfac(find(f_0==3.497000000000000e+09));
output(8,3) = delta_ermreal(find(f_0==3.497000000000000e+09));
output(8,4) = delta_ermimag(find(f_0==3.497000000000000e+09));
output(8,5) = delta_ermtan(find(f_0==3.497000000000000e+09));

output(9,1) = dielec(find(f_0==4.010500000000000e+09));
output(9,2) = lossfac(find(f_0==4.010500000000000e+09));
output(9,3) = delta_ermreal(find(f_0==4.010500000000000e+09));
output(9,4) = delta_ermimag(find(f_0==4.010500000000000e+09));
output(9,5) = delta_ermtan(find(f_0==4.010500000000000e+09));

output(10,1) = dielec(find(f_0==5.017750000000000e+09));
output(10,2) = lossfac(find(f_0==5.017750000000000e+09));
output(10,3) = delta_ermreal(find(f_0==5.017750000000000e+09));
```

```
output(10,4) = delta_ermimag(find(f_0==5.017750000000000e+09));
output(10,5) = delta_ermtan(find(f_0==5.017750000000000e+09));

output(11,1) = dielec(find(f_0==6.005250000000000e+09));
output(11,2) = lossfac(find(f_0==6.005250000000000e+09));
output(11,3) = delta_ermreal(find(f_0==6.005250000000000e+09));
output(11,4) = delta_ermimag(find(f_0==6.005250000000000e+09));
output(11,5) = delta_ermtan(find(f_0==6.005250000000000e+09));

output(12,1) = dielec(find(f_0==6.499000000000000e+09));
output(12,2) = lossfac(find(f_0==6.499000000000000e+09));
output(12,3) = delta_ermreal(find(f_0==6.499000000000000e+09));
output(12,4) = delta_ermimag(find(f_0==6.499000000000000e+09));
output(12,5) = delta_ermtan(find(f_0==6.499000000000000e+09));

output(13,1) = dielec(find(f_0==7.012500000000000e+09));
output(13,2) = lossfac(find(f_0==7.012500000000000e+09));
output(13,3) = delta_ermreal(find(f_0==7.012500000000000e+09));
output(13,4) = delta_ermimag(find(f_0==7.012500000000000e+09));
output(13,5) = delta_ermtan(find(f_0==7.012500000000000e+09));

output(14,1) = dielec(find(f_0==7.506250000000000e+09));
output(14,2) = lossfac(find(f_0==7.506250000000000e+09));
output(14,3) = delta_ermreal(find(f_0==7.506250000000000e+09));
output(14,4) = delta_ermimag(find(f_0==7.506250000000000e+09));
output(14,5) = delta_ermtan(find(f_0==7.506250000000000e+09));

output(15,1) = dielec(find(f_0==8.000000000000000e+09));
output(15,2) = lossfac(find(f_0==8.000000000000000e+09));
output(15,3) = delta_ermreal(find(f_0==8.000000000000000e+09));
output(15,4) = delta_ermimag(find(f_0==8.000000000000000e+09));
output(15,5) = delta_ermtan(find(f_0==8.000000000000000e+09));


%Write Data to CSV with above filename convention
%Please note the last variable is the matrix to be written to the file
csvwrite(strcat(chem,     '_Grit_',     grit,     '_Sample_No._',     sample_set,
exten),output)
```

Appendix B: Test Fixture Drawings

The test fixture drawings were generated based on the computer-aided design (CAD) models created in PTC Creo Parametric. The first drawing is of the fixture from three different viewing angles. The next four drawings are of the 7 mm airline funnel, 7 mm funnel plate, 14 mm airline funnel, and 14 mm funnel plate respectively. The last two drawings are of the platform bases that are secured to the Gilson Performer III Sieve Shaker. These bases also connect to the funnel plates using two threaded rods.

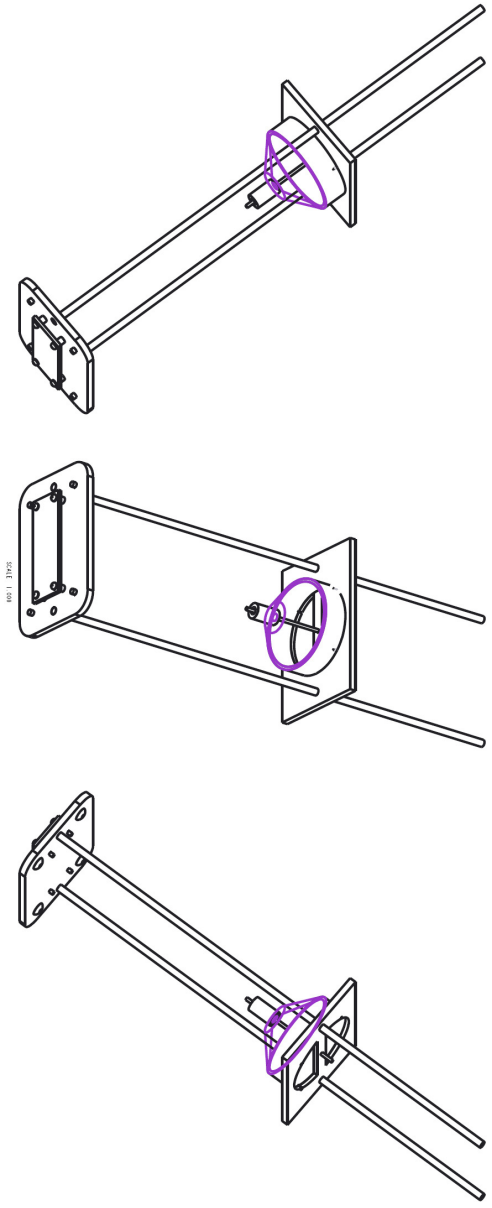

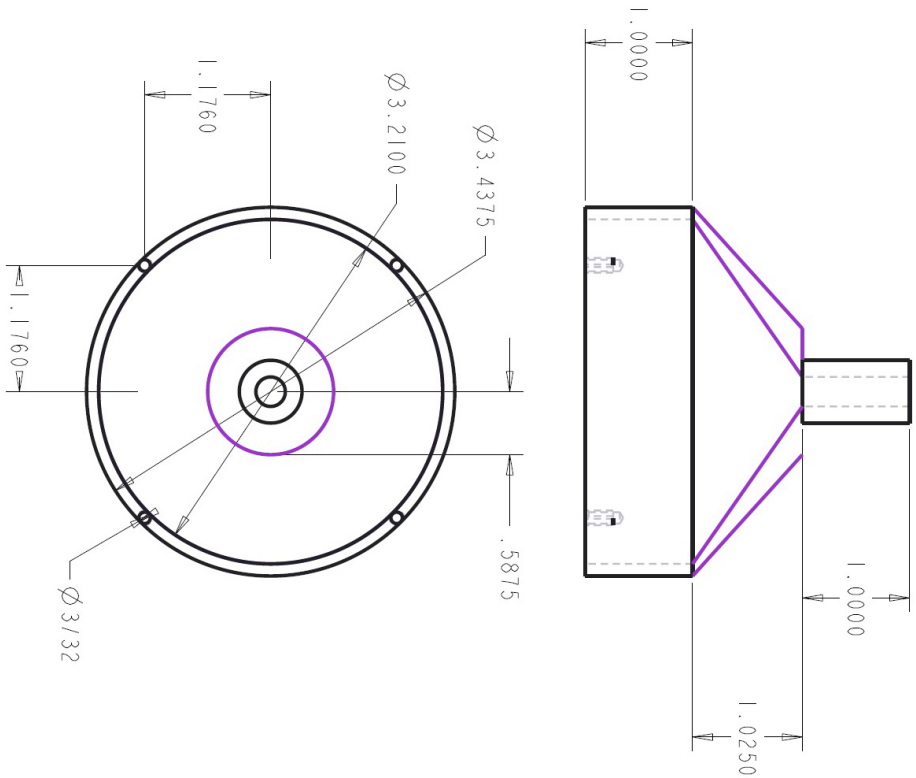
1.0000
1.1760
Ø3.2100
Ø3.4375
1.1760
.5875
Ø3/32
1.0000
1.0250

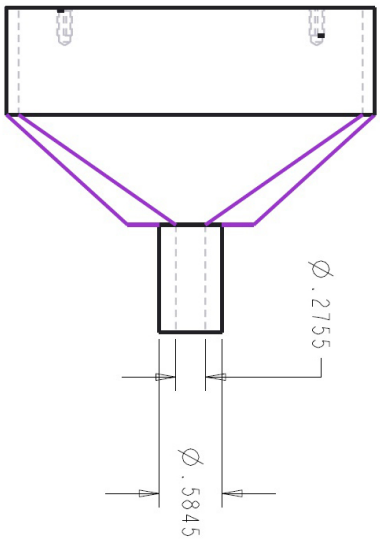
Ø.2755
Ø.5845

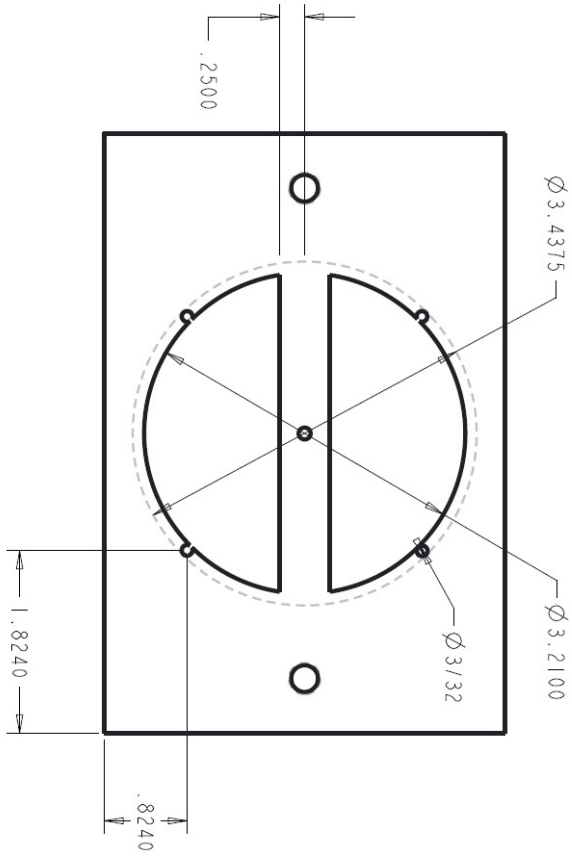
.2500
Ø3.4375
Ø3.2100
Ø3/32
1.8240
.8240

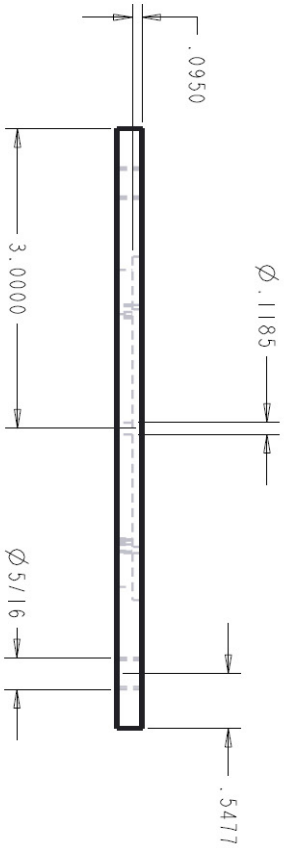
.0950
3.0000
Ø.1185
Ø5/16
.5477

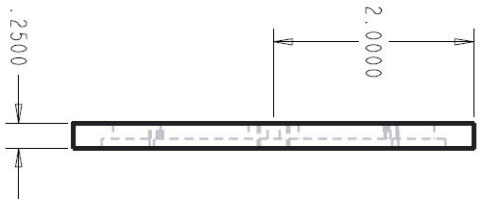
.2500
2.0000

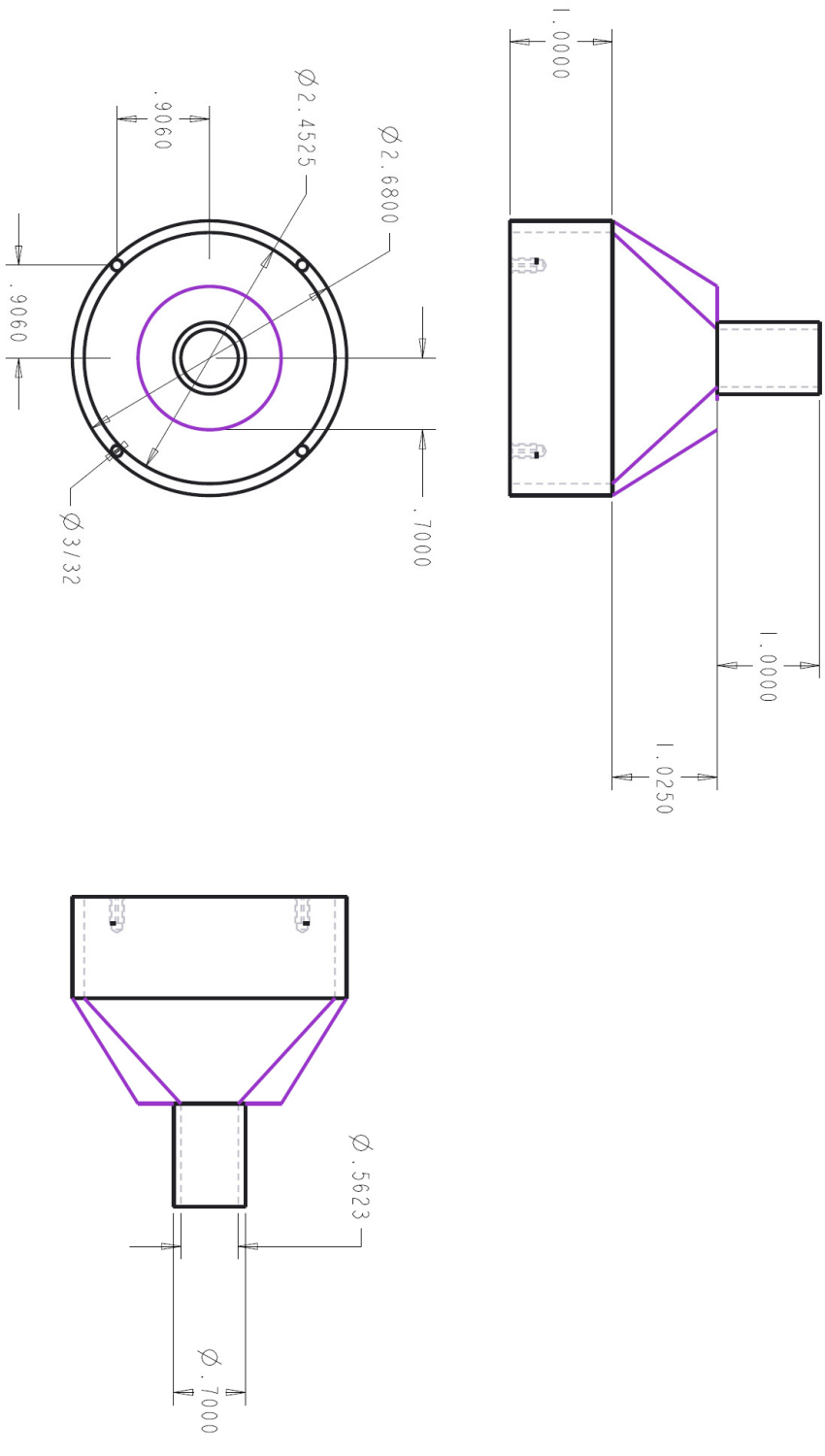
1.0000
Ø2.4525
Ø2.6800
.9060
.9060
.7000
Ø3/32
1.0000
1.0250
Ø.5623
Ø.7000

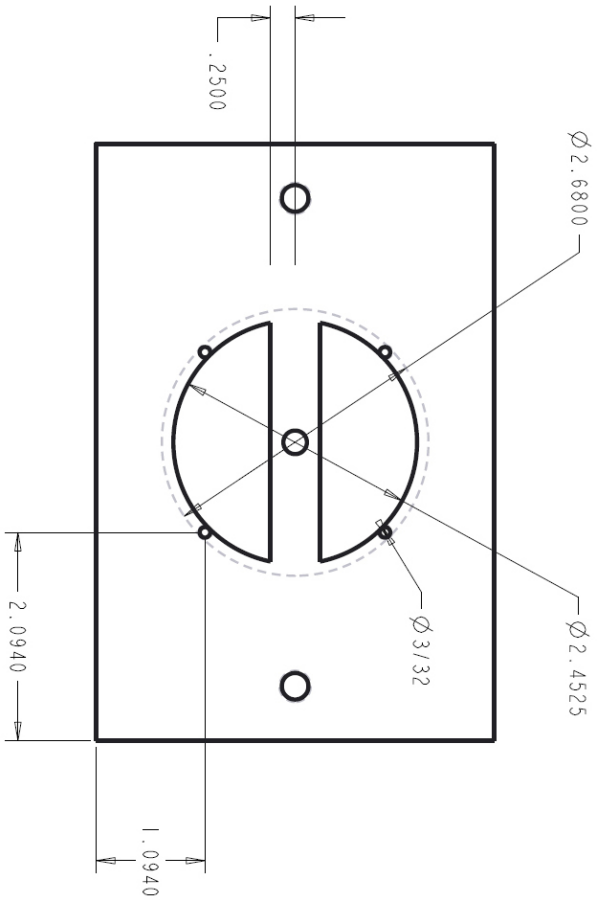
.2500
Ø2.6800
Ø2.4525
Ø3/32
2.0940
1.0940

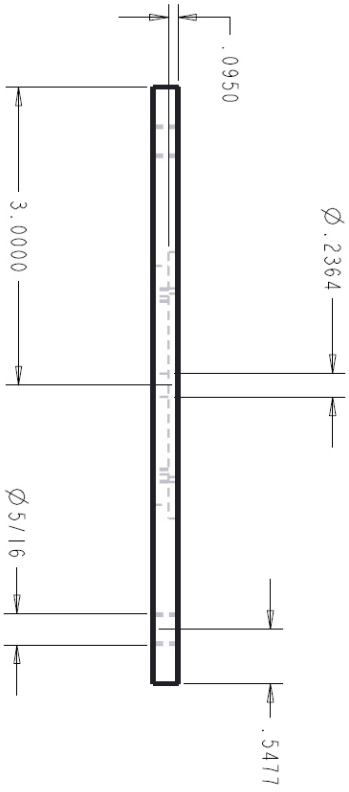
.0950
3.0000
Ø.2364
Ø5/16
.5477

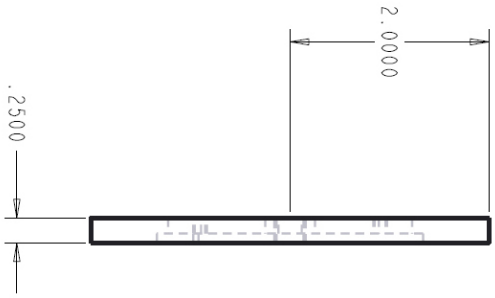
2.0000
.2500

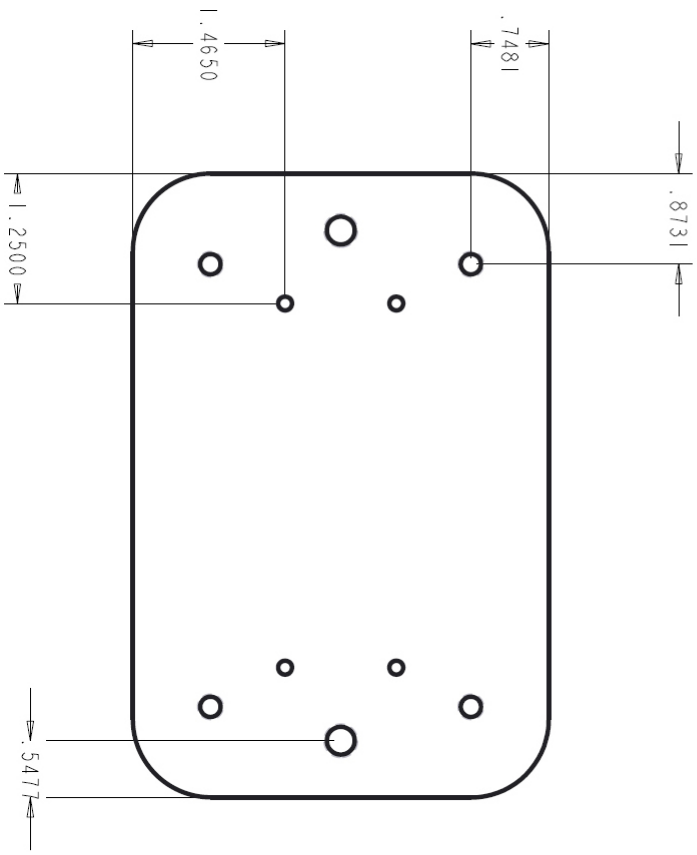
1.4650
.7481
.8731
1.2500
.5477

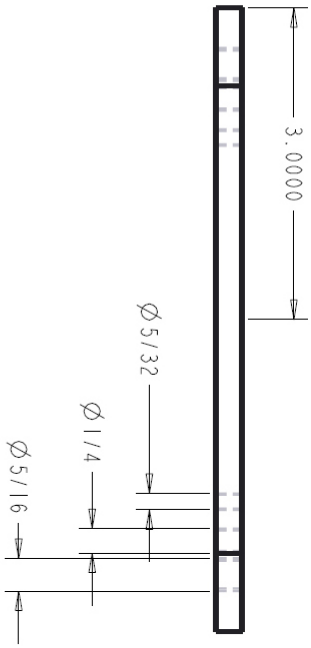
3.0000
Ø5/32
Ø1/4
Ø5/16

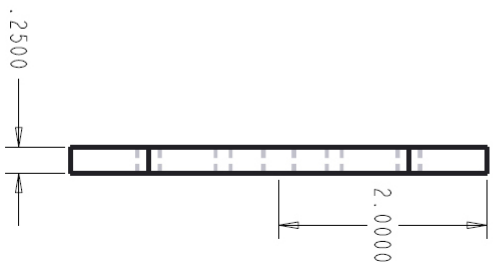
.2500
2.0000

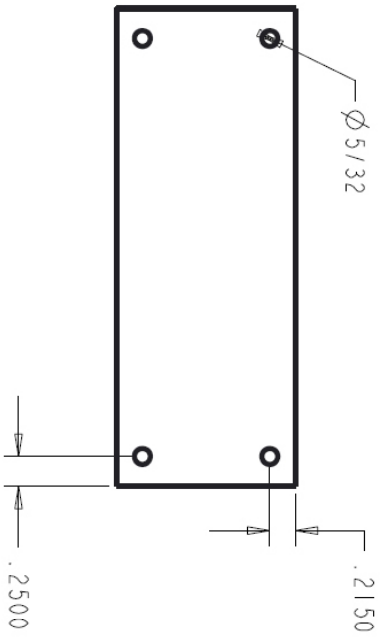
Ø 5/32
.2500
.2150

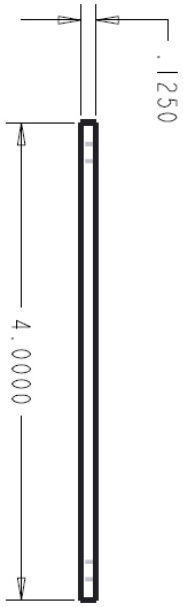
.1250
4.0000

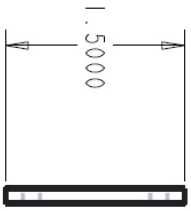
1.5000